

学位論文

**Molecular-Level Precision Functionalization of Surface  
Nanostructures by Noncovalent Interactions**

(非共有結合的相互作用を用いた表面ナノ構造の分子レベル精密修飾)

平成 27 年 12 月博士（理学）申請

東京大学大学院理学系研究科

化学専攻

山田 純也



## — Abstract —

Chemical structure on the surface of materials determines the physicochemical properties such as solubility and binding affinity to other materials. Noncovalent immobilization of functional molecules to the surface is often utilized for the modification of materials due to the facility in operation. For example, surface functionalization of self-assembled objects is often achieved by solvophobic interactions in solution. In another case, nanocarbon materials can be noncovalently functionalized by using chemically-modified aromatic molecules through  $\pi$ - $\pi$  interaction. However, these noncovalent approaches often lack the control of interactions at the molecular level precision and cause nonspecific adsorption of the molecules to the surface. In addition, the ill-controlled molecular immobilization methods often induce destabilization of self-assembled objects and decrease in cost-effectiveness of the surface modification. Therefore, more precise surface functionalization methods are needed.

In this thesis, I developed two kinds of supramolecular surface modification methods to overcome these problems. First one is post-surface modification of a self-assembled nanocapsule composed of a fluoros fullerene amphiphile via fluoros interaction. Second one is shape-selective surface modification of a nanocarbon via host-guest interaction. Specific structure on a nanocarbon surface was selectively modified with cyclodextrins (CDs), which are common host molecules for encapsulation of small guest molecules, and the water-dispersibility of the nanocarbon was improved by the addition of small amount (1 wt%) of CDs. In addition, the host-guest complex of nanocarbon and CD was visualized by high-resolution transmission electron microscopy (TEM) at a single molecule level. A functional group on CD was also visualized by TEM.

Chapter 1 describes non-covalent modification methods for surface nanostructures and the applications. Ligand display on self-assembled capsules and molecular adsorption on nanocarbons are highlighted. In addition, electron microscopic analysis of single organic molecules using nanocarbons as a template is discussed.

Chapter 2 describes protein-ligand display on the surface of sub-micrometer-sized fluoros fullerene vesicle via fluoros interaction. The vesicle composed of fluoros fullerene amphiphile that has three different moieties, perfluoroalkyl side chains/potassium cyclopentadienide /fullerene core, ( $Rf_5C_{60}^-K^+$ ). When the amphiphile forms the vesicular structure, the perfluoroalkyl side chains are exposed to the surface of the vesicle in water. Therefore fluoros-tagged protein ligands can be immobilized on the surface of the vesicle via fluoros interaction simply by mixing them in water. In addition, the vesicle bound to target proteins via the surface ligands.

Chapter 3 describes shape-selective surface modification of a nanocarbon via host-guest interaction of CDs. Carbon nanohorn (CNH) aggregates are 50–150 nm-sized aggregates of cone-shaped carbon nanotubes. The size of cone-shaped tip of CNH is almost the same size as [60]fullerene. CDs are usually used as a host molecule for encapsulation of small guest molecules in water. In particular,  $\gamma$ -CD is known to encapsulate fullerenes into its inner cavity and forms a stable water-soluble complex. Inspired by the shape-selective encapsulation of CDs, I achieved selective modification of the tip of CNH aggregates with  $\gamma$ -CD and the derivatives. Since  $\gamma$ -CD is hydrophilic molecule, hydrophobic CNH aggregates became dispersable in water upon complexation with  $\gamma$ -CD. The complex structures of  $\gamma$ -CD and a tip of CNH were first visualized by TEM at a single-molecule level with atomic resolution. In addition, this tip-selective molecular immobilization on CNH aggregates was applied to visualization of specimens bound to primary hydroxyl group of  $\gamma$ -CD.

Finally, chapter 4 summarizes the present thesis and describes possible outcomes for the chemistry of noncovalent functionalization of self-assembled objects and solid materials that have specific surface nanostructures.

## — Acknowledgements —

I am very grateful to my supervisor, Prof. Dr. Eiichi Nakamura, who guided me through the process of writing this thesis. His enthusiasm, motivation, immense knowledge, and some ambitious orders helped me in not only all these year of research but also in the decision for my futures.

This thesis would not be possible without the support of associate professor Dr. Koji Harano. I am very grateful for all the discussions, which were essential for understanding the experimental results, and for the guidance in the whole research process. His broad interest and knowledge also helped me to get curiosity for new research fields.

I would like to show my gratitude to associate professor Dr. Hayato Tsuji and associate professor Dr. Laurean Ilies, who gave me good advices on the research life and made this laboratory a good and pleasurable place to work.

I am really grateful to Prof. Dr. Bart Jan Ravoo (Westfälische Wilhelms-Universität of Münster, Germany), who welcomed me to join his group as a student studying abroad. Experience in his group expanded my chemistry world and gave me a key to open new research project that is described in this thesis.

I appreciate the support of all members from Dr. Harano's subgroup; Dr. Chao Liu, Dr. Sai Prakash Maddala, Mr. Junfei Xing, Mr. Yuki Itabashi, Mr. Takuya Tsubota, Ms. Satori Kowashi, and Mr. Hiroki Hanayama. I also thank the support from former members; Dr. Yonggang Zhen, Dr. Kosuke Minami, Dr. Hirohisa Nitta, Dr. Ricardo M. Gorgoll, Ms. Utako Takeda, Mr. Takakazu Seki, Ms. Mami Nakatake, Mr. Kei Matsumoto, and Ms. Mayuko Isomura. I am especially grateful for the support of Mr. Satoshi Okada, who spent the whole research life in the same laboratory and the same subgroup together. Existence of him is a strong support for me to work in this laboratory.

I am also grateful for the support of Mr. Kazutaka Shoyama and Mr. Tatsuaki Matsubara, who are students in the same batch with me in this laboratory. They showed me A–Z in the University of Tokyo since I entered in this graduated school.

I am indebted to all of my laboratory colleagues who showed immense support and patience to me. I also thank Dr. Takao Kaneko and Ms. Akemi Maruyama, who have supported the research in this laboratory for so many years.

I am grateful to associate professor Dr. Naoya Shibata, Dr. Akihito Kumamoto, Dr. Mitsushiro Saito (JEOL Ltd.), Ms. Aya Okubo, and Mr. Hajime Hoshi for the TEM measurements and meaningful discussion on the interpretation of the results. Some of the TEM measurements were conducted in the Research Hub for Advanced Nano Characterization, The University of Tokyo, under the support of "Nanotechnology Platform" (project No. 12024046) by MEXT, Japan.

I also thank Ravoo's group members (Westfälische Wilhelms-Universität of Münster, Germany), who showed immense support and patience to me. They also showed me how to live in Germany and how to enjoy the daily life. My world was dramatically expanded by meeting them.

I do not forget the support of Ms. Satoko Karasawa who is my fiancée. She is always close to me whenever I was very busy, sick, or depressed for doing research and hunting a job. All joyful time when we live together always encourages me to go forward.

There are no words to describe how thankful I am to my parents, Mr. Kazunori Yamada and Ms. Naoko Yamada, who grew me and gave me excellent education. I also really thank my relatives; Ms. Tamie Yamaguchi, Mr. Toshikazu Yamaguchi, Ms. Nami Yamaguchi, Ms. Tomomi Yamaguchi, and Mr. Teppei Yamaguchi. I do not forget saying thanks to my deceased relatives; Mr. Yorizou Yamaguchi and Ms. Michie Horiuchi.

Lastly, I would like to thank MERIT that gave me financial support and providing an opportunity to meet collaborator of my Ph.D. studies.

## — List of Publications —

### 【Publication related to the thesis】

“High-Density Display of Protein Ligands on Self-Assembled Capsules via Noncovalent Fluorous Interactions” Harano, K.; Yamada, J.; Mizuno, S.; Nakamura, E.; *Chem. Asian J.* **2015**, *10*, 172–176.

### 【Oral presentations】

[1] “Molecular Release from Fluorous Glass Substrates Triggered by Increase in Gas Concentration in Water”, Junya Yamada, Koji Harano, Eiichi Nakamura 日本化学会第 94 春季年会, 名古屋大学, 東山キャンパス, 名古屋, 2014 年 3 月

[2] “Shape-Selective Host-Guest Complexation of  $\gamma$ -Cyclodextrin with Nanocarbon Surfaces”, Junya Yamada, Akihito Kumamoto, Satoshi Okada, Naoya Shibata, Koji Harano, Eiichi Nakamura 日本化学会第 95 春季年会, 日本大学, 船橋, 2015 年 3 月(学生講演賞受賞)

### 【Poster presentations】

[1] 「フルオラス相互作用を用いた表面機能化水溶性ナノカプセルの構築」, 山田純也, 水野慎一郎, 原野幸治, 中村栄一, 第 24 回基礎有機化学討論会, 学習院大学, 東京, 2013 年 9 月

[2] 「フルオラス相互作用を用いたナノベシクル上における糖類の表面呈示」, FCCA グライコサイエンス若手フォーラム 2014, 山田純也, 水野慎一郎, 原野幸治, 中村栄一, 名古屋大学, 名古屋, 2014 年 8 月

[3] 「フルオラス表面での分子認識を利用した非極性気体応答性分子放出システム」, 山田純也, 関貴一, 原野幸治, 中村栄一, 第 25 回基礎有機化学討論会, 東北大学, 仙台, 2014 年 9 月

[4] 「フルオラス相互作用を用いたナノベシクル上におけるタンパクリガンド分子の表面呈示」, 山田純也, 水野慎一郎, 原野幸治, 中村栄一, 第四回 CSJ 化学フェスタ 2014, タワーホール船堀, 東京, 2014 年 10 月

[5] “High Density Display of Protein Ligands on Fullerene Vesicles via Noncovalent Fluorous Interactions”, Junya Yamada, Shinichiro Mizuno, Koji Harano, Eiichi Nakamura, International Symposium on the Synthesis and Application of Curved Organic  $\pi$ -Molecules and Materials (CURO- $\pi$ ), 京都大学, 宇治, 2014 年 10 月

[6] “Shape-Selective Host-Guest Complexation and Single-Molecule Microscopic Observation of Cyclodextrins on Nanocarbon Surfaces”, Junya Yamada, Akihito Kumamoto, Naoya Shibata, Koji Harano, Eiichi Nakamura, 第 26 回基礎有機化学討論会, 愛媛大学・松山大学, 松山, 2015 年 9 月

[7] “Host-guest complexation and TEM imaging of cyclodextrins on nanocarbon surface”, Junya Yamada, Akihito Kumamoto, Naoya Shibata, Koji Harano, Eiichi Nakamura, Pacificchem 2015, Honolulu, Hawaii, USA, 2015 年 12 月 (口頭発表と同時講演)

## — Abbreviations —

Ac	Acetyl	<sup>i</sup> Pr	Isopropyl
AFM	Atomic Force Microscopy (Microscope)	IR	Infrared Spectroscopy
APCI	Atmospheric Pressure Chemical Ionization	ITO	Indium Tin Oxide
aq	aqueous solution	IZO	Indium Zinc Oxide
a.u.	Arbitrary Unit	LLS	Laser Light Scattering
Bu	Butyl	M	Molar (mol/L)
CAC	Critical aggregation concentration	Man	Mannopyranoside
CD	Cyclodextrin	Me	Methyl
CNH	Carbon Nanohorn	mp	Melting Point
CNT	Carbon Nanotube	NMR	Nuclear Magnetic Resonance
ConA	Concanavalin A	ODCB	<i>o</i> -Dichlorobenzene
DCM	Dichloromethane	PdI	Polydispersity Index
DLS	Dynamic Light Scattering	PNA	Peanut Agglutinin
DMF	<i>N,N</i> -Dimethylformamide	PTFE	Polytetrafluoroethylene
DMSO	Dimethylsulfoxide	rt	Room Temperature
ESI	Electrospray Ionization	SEM	Scanning Electron Microscopy (Microscope)
Et	Ethyl	SMART	Single Molecule Atomic Real Time
eq	Equivalent	STEM	Scanning Transmission Electron Microscopy (Microscope)
FAB	Fast Atom Bombardment	TEM	Transmission Electron Microscopy (Microscope)
FT	Fluorous-Tagged	Tf	Trifluoromethanesulfonyl
Gal	Galactopyranoside	Ts	<i>p</i> -Toluenesulfonyl
GCP	Graphitic Carbon Particle	TG-DTA	Thermogravimetry-Differential Thermal Analysis
GPC	Gel Permeation Chromatography	THF	Tetrahydrofran
HEPES	4-(2-Hydroxyethyl)- 1-Piperazineethanesulfonic Acid	TMS	Tetramethylsilane
HPLC	High Pressure (Performance) Liquid Chromatography	UV	ultraviolet
HRMS	High-Resolution Mass Spectrometry	Vis	Visible



## — Contents —

<b>Abstract .....</b>	<b>i</b>
<b>Acknowledgements .....</b>	<b>iii</b>
<b>List of Publications .....</b>	<b>v</b>
<b>Contents .....</b>	<b>vii</b>
<b>Chapter 1: General Introduction .....</b>	<b>1</b>
1.1. <i>Noncovalent Modification of Self-Assembled Objects</i> .....	3
1.2. <i>Noncovalent Modification of Nanocarbons</i> .....	6
1.3. <i>Electron Microscopic Visualization of Single Molecules Using Nanocarbons</i> .....	8
1.4. <i>References</i> .....	11
<b>Chapter 2: Hierarchical Construction of Protein-Coated Capsule by Orthogonal Noncovalent Interactions.....</b>	<b>15</b>
2.1. <i>Introduction: Fullerene Vesicle and the Surface Modification</i> .....	17
2.2. <i>Preparation of Fullerene Vesicles and FT Molecules</i> .....	20
2.2.1. <i>Synthesis of Fluorous Fullerene Amphiphile and FT Ligand Molecules</i> .....	20
2.2.2. <i>Preparation of Fullerene Vesicles</i> .....	22
2.3. <i>Ligand Display on Fullerene Vesicles</i> .....	22
2.4. <i>Protein Binding on Ligand-Coated Fullerene Vesicles</i> .....	27
2.5. <i>SEM and STEM Imaging of Lectin-Coated Fullerene Vesicles</i> .....	31
2.6. <i>Conclusion</i> .....	33
2.7. <i>References</i> .....	33
<b>Chapter 2: Experimental Section &amp; Supporting Information .....</b>	<b>35</b>
<b>Chapter 3: Shape-Selective Surface Modification of a Nanocarbon via Host-Guest Interaction of Cyclodextrins .....</b>	<b>49</b>
3.1. <i>Introduction</i> .....	51
3.1.1. <i>Properties and Functionalization of Carbon Nanohorns</i> .....	51
3.1.2. <i>Host-Guest Complexation of Cyclodextrins with [60]Fullerene</i> .....	51
3.2. <i>Dispersion of CNH Aggregates in Water with CDs</i> .....	53
3.2.1. <i>Shape-Selective Recognition of Surface Nanostructure of Nanocarbons via Host-Guest Interaction of CDs</i> .....	53
3.2.2. <i>Size Effect of CDs for Complexation with CNH</i> .....	57
3.3. <i>Single-Molecule TEM Imaging of CD/CNH Complex</i> .....	59

3.3.1. Molecular-Level Structure of the Host-Guest Complex of CNH and CDs .....	59
3.3.2. Single-Molecule Atomic Real-Time TEM Observation of $\gamma$ -CD.....	63
3.4. <i>Conclusion</i> .....	70
3.5. <i>References</i> .....	71
<b>Chapter 3: Experimental Section &amp; Supporting Information .....</b>	<b>73</b>
<b>Chapter 4: Summary &amp; Outlook.....</b>	<b>91</b>

*Chapter 1*

**— Chapter 1—  
General Introduction**

## *Chapter 1*

## Chapter 1

Chemical structure on the surface of materials determines the physicochemical properties such as solubility and binding ability to other materials. Modification of the surface with hydrophilic groups increases the solubility in water, and modification with surface ligand induces binding materials to specific protein. Therefore a variety of surface modification methods have been developed for functionalization of materials in materials science. Especially, noncovalent modification with functional small molecules is energetically studied due to its facility in the operation compared with covalent methods. Here I introduce noncovalent surface modification methods focusing on functionalization for self-assembled objects and nanocarbons.

### 1.1. Noncovalent Modification of Self-Assembled Objects

Amphiphilic molecules such as surfactants,<sup>1</sup> lipids<sup>2</sup> and ionic block copolymers<sup>3</sup> composed of hydrophilic head and hydrophobic tail moieties form self-assembled objects. Amphiphilic molecules assemble in proper solvent via solvophobic interaction. In the case of self-assembly in water, amphiphilic molecules form micelle, bilayer vesicle, or bilayer sheets orienting the hydrophobic tails inside of the structure depending on the packing structure in self-assembly.<sup>4</sup> Generally, conical surfactants and ionic block copolymers tend to form micelles, while rod-shaped ionic block copolymers and lipids tend to form bilayer structures (Figure 1-1).<sup>3b, 5</sup>

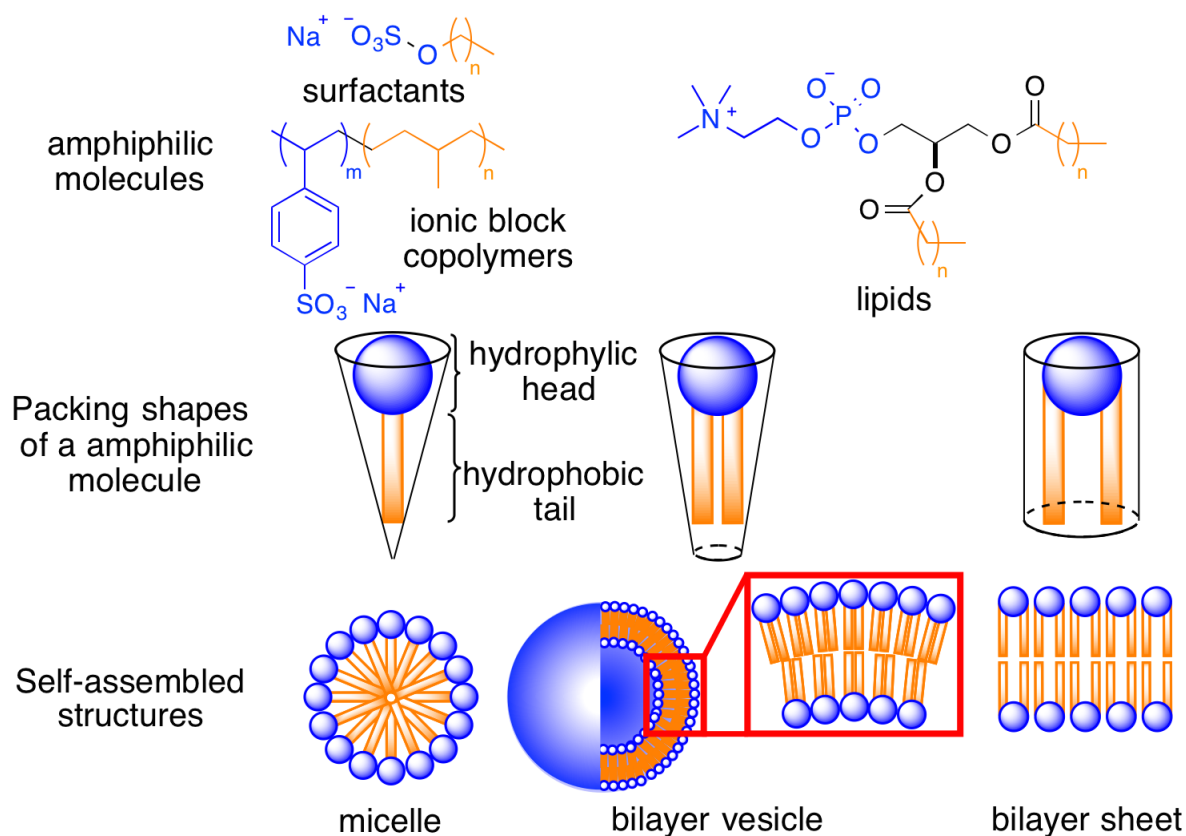


**Figure 1-1.** Relationship between the geometric structures of amphiphilic molecules and the self-assembled structures.

## Chapter 1

Hydrophobic molecules can be incorporated into the hydrophobic interior of self-assembled objects made from amphiphiles, while hydrophilic molecules can be encapsulated into the inner cavity of vesicles at pre- and post-formation of the structures in water (Figure 1-2a).<sup>2, 3b, 6</sup> As an application using this phenomena, micelles and vesicles that contain drug molecules on the inside are used as a drug carrier to suppress metabolization of drugs and to add sustained release property in pharmacotherapy.<sup>3b, 7</sup> In addition, the surface of the vesicles is modified by incorporation of functional molecules via hydrophobic interaction, for instance, ligand modification for binding to protein, cationic modification for immobilization of DNA, and light-harvesting antenna for responsiveness to light irradiation and construction of bio-mimetic materials (Figure 1-2b).<sup>8</sup>

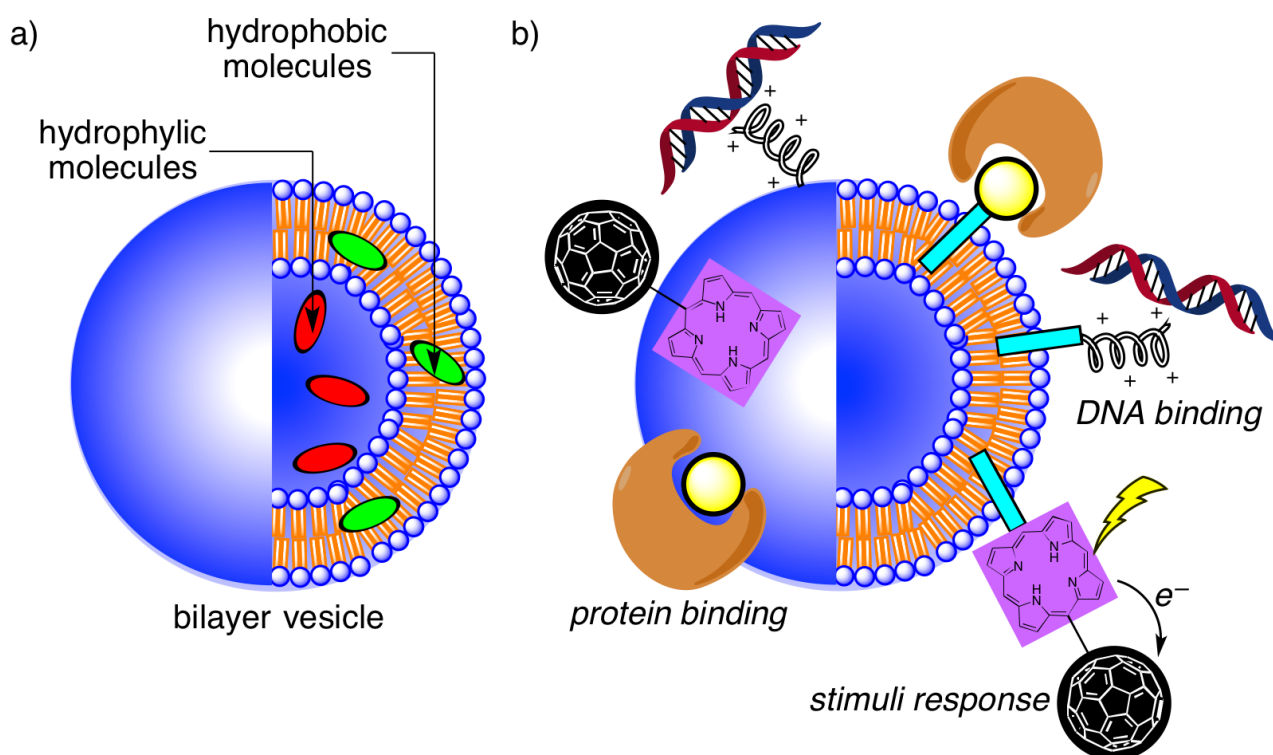


**Figure 1-2.** Incorporation of molecules into bilayer vesicles. (a) Incorporation of molecule such as drug molecules into the inside of vesicles and (b) display of functional molecules on the surface of vesicles.

Ligand functionalization on the surface of self-assembled objects has attracted much attention in the field of chemical biology.<sup>9</sup> Since vesicles have capsular structure, they can contain both hydrophilic and hydrophobic drugs on the inside of the cavity and the membrane, respectively. In addition, their size can be adjusted to the suitable size (10–100 nm) for drug delivery to tumor cells.<sup>10</sup> Therefore, vesicles are widely studied as a drug carrier in drug delivery system.<sup>10a, 11</sup> Modification of the surface of vesicles with protein-binding ligand molecules as “address labels” enables them to be delivered to the target diseases cells. Amphiphilic protein ligands that are composed of protein-binding moiety (conventionally saccharides) and hydrophobic tag moiety such

as alkyl, and adamantyl are immobilized on the membrane of the vesicles via hydrophobic interaction and host-guest interaction in water, respectively (Figure 1-3).<sup>8b, 8c, 12</sup>

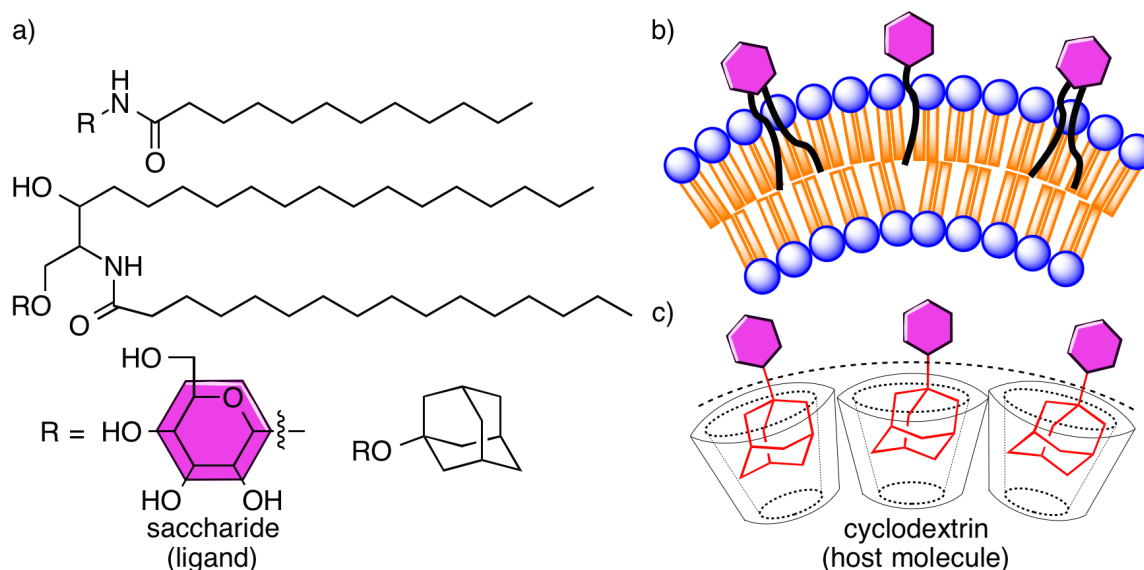


**Figure 1-3.** Ligand display on the surface of vesicles. (a) Aliphatic-tagged saccharides. (b) Ligand display on the surface of a lipid vesicle via hydrophobic interaction. (c) Functionalization of a cyclodextrin vesicle via host-guest interaction.

Hydrophilic saccharides moiety is displayed on the surface of the vesicles (Figure 1-3b, c) and binds to the target protein.<sup>12</sup> However, immobilization of the protein ligands into the membrane of vesicles, especially liposomes, often destabilizes the membrane structure due to competitive interactions between the membrane formation and the ligands immobilization (Figure 1-4).<sup>13</sup>

In the chapter 2 in this thesis, I demonstrate a facile ligand display method on the surface of bilayer vesicles without affecting the structural integrity by using self-assembled fullerene bilayer as a scaffold.

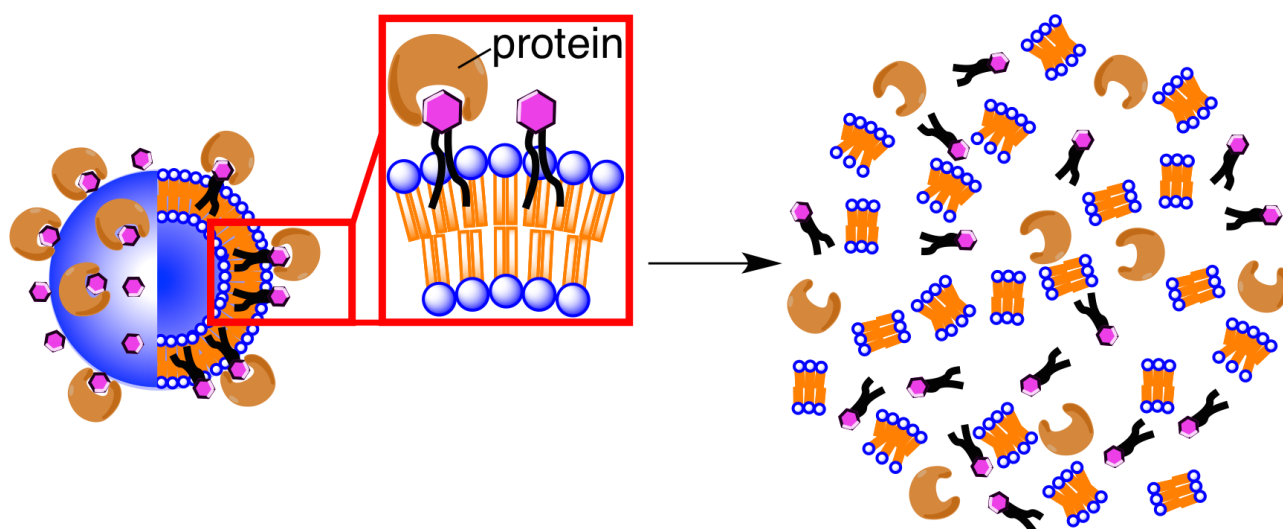


**Figure 1-4.** Destabilization of the membrane structure of vesicles due to competitive uptake of ligand molecules.

## 1.2. Noncovalent Modification of Nanocarbons

Nanocarbons such as fullerenes,<sup>14</sup> carbon nanotubes (CNTs),<sup>15</sup> and graphene<sup>16</sup> have much attention in materials science due to the unique electrochemical properties<sup>17</sup> and the robust molecular architecture<sup>17a, 18</sup> derived from the large network of  $\pi$  system (Figure 1-5). Many modification methods of nanocarbons have been developed to adjust the chemical properties to their usages. Noncovalent modification is more manageable method than covalent modification because it does not break the  $\pi$  system and keep the chemical properties of nanocarbons.

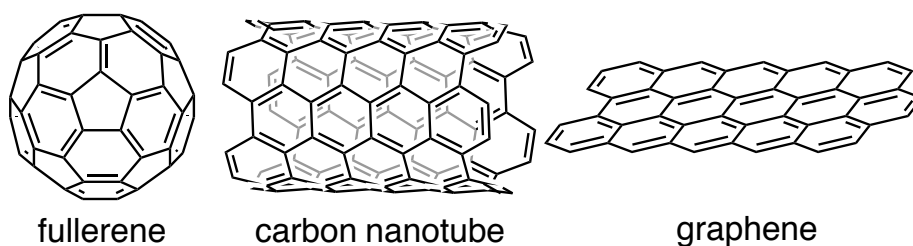


**Figure 1-5.** Structures of nanocarbons.

Generally, noncovalent surface modification of nanocarbons are performed by using long aliphatic molecules<sup>19</sup> or chemically-modified aromatic molecules such as porphyrin,<sup>20</sup> styrene,<sup>21</sup> and pyrene<sup>22</sup> through hydrophobic interaction and  $\pi$ - $\pi$  interaction (Figure 1-6a-c).<sup>23</sup> Bowl-shaped and cage-shaped host molecules such as corannulene,<sup>24</sup> calixarenes,<sup>25</sup> and cyclodextrins<sup>26</sup> form an inclusion complex with fullerenes by recognition of the size and the curved structure of the fullerenes via host-guest interaction (Figure 1-6d).<sup>27</sup> In addition, cyclic aromatic rings are also known to encapsulate fullerenes on the inside (Figure 1-6e).<sup>28</sup> Compared with fullerenes that can be handled as a molecule, however, noncovalent surface modification of CNTs and graphene cannot be controlled very well due to the bulk nature of the materials. Functional molecules are randomly physisorbed on the surface of CNTs and graphene, hence the amount and orientation of the adsorbed molecules are difficult to investigate (Figure 1-6b, c).

Nanocarbons dissolve neither in hydrocarbon nor polar solvents. Even if they are dissolved, they are easily agglomerated in the solution or dispersion liquid. This agglomeration is a severe problem that impedes further functionalization and the following applications. Therefore, improvement of their wettability is often to become a topic of their functionalization.<sup>19, 21, 26, 29</sup> Especially, dispersion and de-bundling of CNTs are widely studied in both organic solvents and aqueous solvents because of the importance in application.<sup>30</sup> Pyrene with an aliphatic pendant was adsorbed on the surface of CNTs through the pyrene moiety and it improved the dispersibility of CNTs in organic solvents such as DMF and methanol (Figure 1-6c).<sup>22a</sup> Surfactants and amphiphilic block copolymers are also adsorbed on the surface of CNTs with the hydrophobic tail and made



## Chapter 1

them dispersed in aqueous solvents (Figure 1-6b).<sup>19, 21</sup> However, large amount of dispersants, at least as much as CNTs, are necessary for the dispersion of CNTs, which often cause bad effects in the physicochemical properties because noncovalent interaction between nanocarbon surface and dispersants usually weak and conventional dispersants aggregates into the self-assembled structure not adsorb on the surface of nanocarbons. In addition, the dispersants are difficult to be removed completely.

In the chapter 3 in this thesis, I try to develop a shape-selective surface modification method of a nanocarbon to overcome the general problem of nonspecific adsorption of functional molecules on the surface.

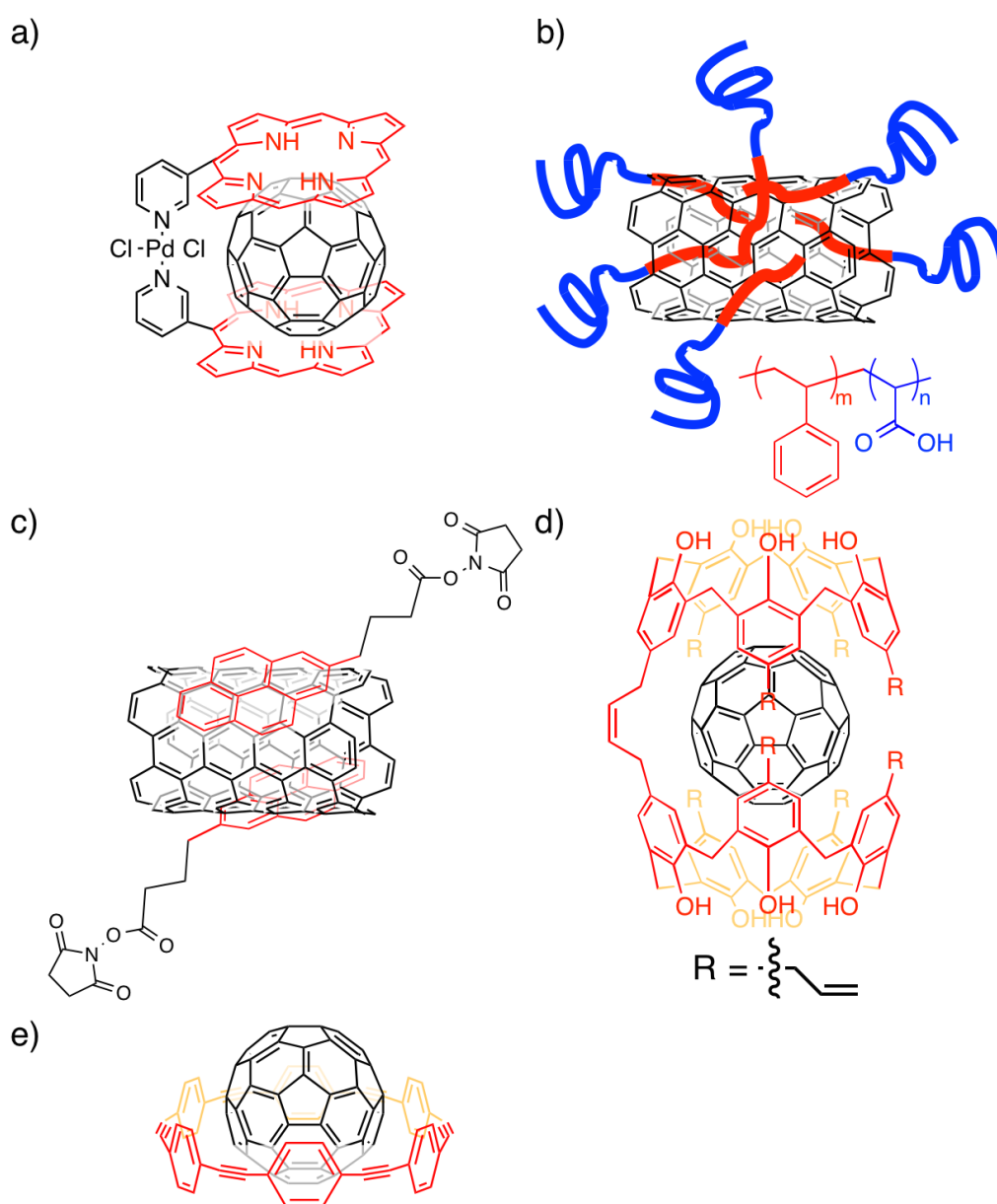


**Figure 1-6.** Noncovalent modification of nanocarbons via  $\pi$ - $\pi$  interaction. Molecules interact with nanocarbons via (a, b) multivalent interactions, (c) monovalent interaction, and (d, e) host-guest interactions.

### 1.3. Electron Microscopic Visualization of Single Molecules Using Nanocarbons

Electron microscopic imaging of the nanometer-sized structure and the behavior of organic molecules give us a new insight to understand the boundary between single molecule-level events and bulk properties of materials. However, the visualization of single organic molecules has been thought to be impossible by transmission electron microscopy (TEM) due to the significant damage of the specimens by electron irradiation during TEM measurement.<sup>31</sup> In contrast, fullerene molecules and the derivatives incorporated in CNTs, fullerene peapod, were stably observed by TEM because of isolation of fullerenes in CNTs (Figure 1-7a).<sup>32</sup> Series of TEM images taken with a small time interval successfully traced the translational and the rotational motions of fullerenes,<sup>33</sup> and also, the dimerization and the carbon-carbon bond reorganization reactions of fullerenes (Figure 1-7b).<sup>34</sup>

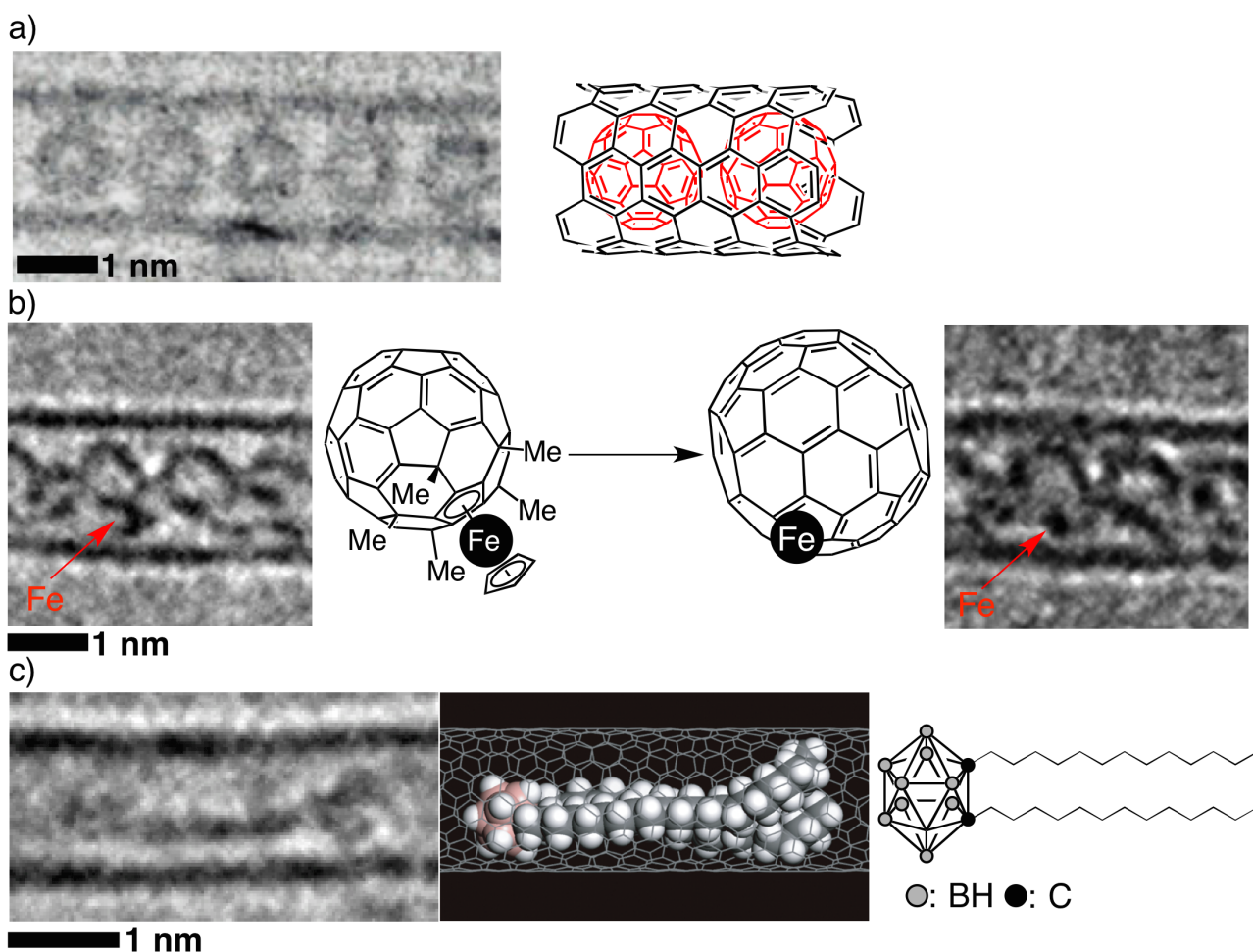


**Figure 1-7.** TEM visualization of specimens on the inside of CNTs. (a) Fullerene peapod, Reprinted from ref. 32c, Copyright © 2005 American Chemical Society. (b) C–C bond reorganization of fullerenes under electron irradiation. Reprinted from ref. 34b, Copyright © 2011 American Chemical Society. (c) Hydrocarbon-attached *ortho*-carborane (left: TEM image, middle: simulation image of the TEM image). Reprinted from ref. 35a, with permission from AAAS.

## Chapter 1

The stereotype for TEM visualization has been broken by success in observation of hydrocarbon-attached *ortho*-carborane by using CNTs as a cage to fixation (Figure 1-7c).<sup>35a</sup> The rotational motions, the conformational changes, and the motion of organic molecules induced by interaction with the wall of CNTs were also observed.<sup>35</sup> In this strategy, however, the specimen molecules should be incorporated into the inside of CNTs. The incorporation is carried out by vacuum vapor deposition,<sup>35</sup> therefore molecules that cannot be vaporized and cannot be tolerated under high temperature are not available. In addition, the observed molecules are limited by the size of the diameter of CNTs. These problems reduce the versatility of the single molecule TEM visualization.

The limitation of TEM visualization using CNTs was overcome using carbon nanohorn (CNH) aggregates<sup>36</sup> as another specimen support. CNH aggregates are 50–150 nm-sized aggregates of cone-shaped CNTs. Since the tip of CNH is more reactive than the sidewall due to the highly curved and strained  $\pi$  system, specimen molecules that are activated by succinimide ester were covalently bound to the tip of CNH via amide bonding (Figure 1-8a).<sup>37</sup>

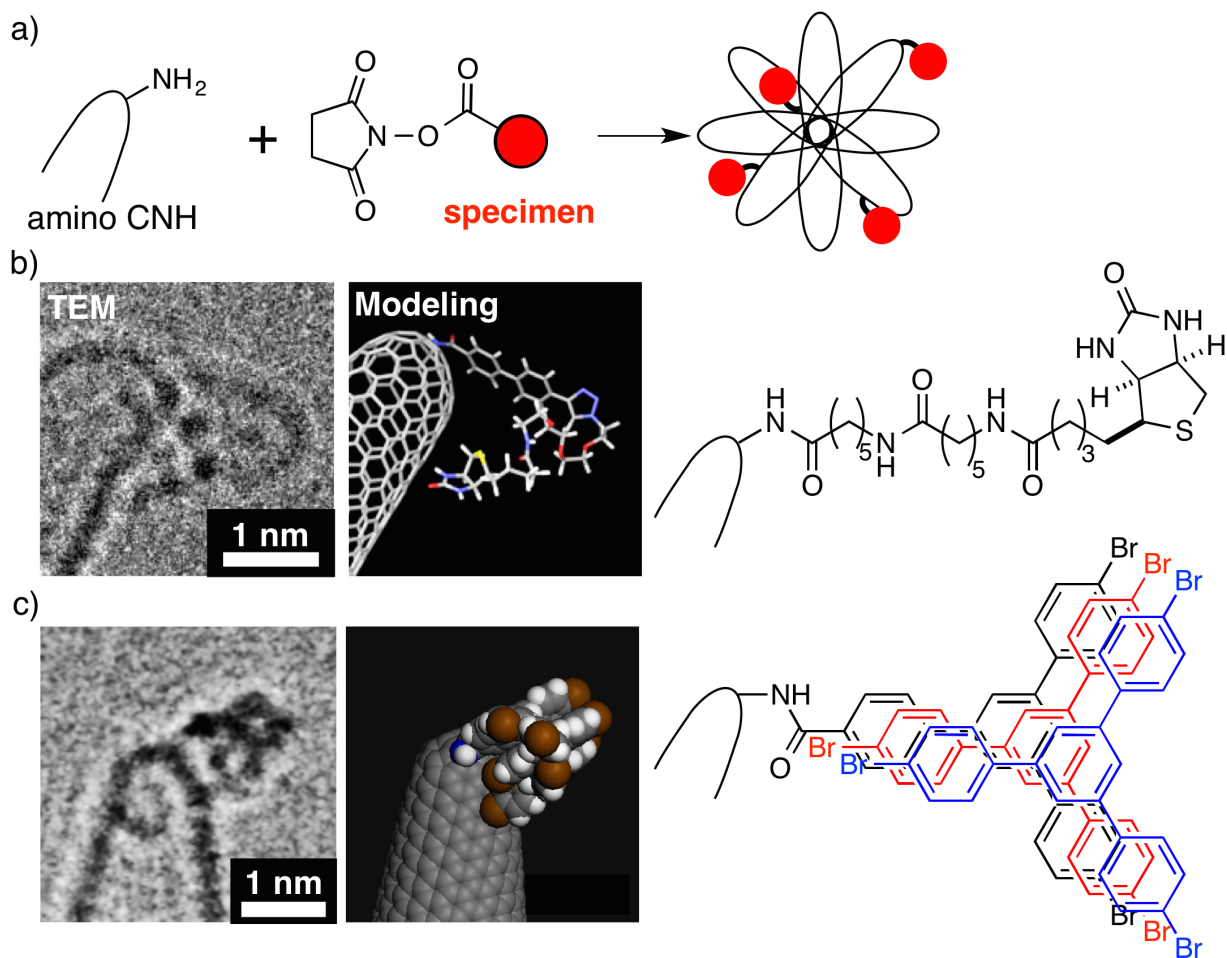


**Figure 1-8.** TEM visualization of specimens on the outside of CNTs (CNH). (a) Schematic illustration of specimen binding to amino CNH. TEM images of (b) biotinylated molecule and (c) cluster of dibromophenylbenzamide and tribromophenylbenzene. (b) Reprinted from ref. 38c, Copyright © 2015 American Chemical Society, (c) Reprinted from ref. 38b, Copyright © 2012 Macmillan Publishers Limited. All Rights Reserved.

## Chapter 1

Perfluorocarbon, biotinylated molecule, and Y-shaped dibromophenylbenzamide were observed in near-atomic resolution by TEM and their conformational changes were investigated (Figure 1-8b, c).<sup>35d, 38</sup> This imaging technique is mild enough to take sequential image of van der Waals clusters of organic molecules (Figure 1-8c).<sup>38b</sup> Because of the smaller spatial limitation than inside of CNTs, larger specimen molecules succeeded in applying to TEM observation, and its more dynamic motion was observed on the tip of CNH. The molecular dynamics was quantified by cross-correlation ( $\gamma$ ) between consecutive each two frames of the movie of TEM images, and it was revealed that the motion was depending on acceleration voltage of TEM (Figure 1-9).<sup>38c</sup> However, the modification yield on CNH via covalent bonding is very low, and it is quite difficult to confirm that specimen molecules are really immobilized of the tip before TEM observation.

In the chapter 3 in this thesis, I discuss shape-selective surface modification of CNH by high resolution TEM imaging. In addition, I developed a new methodology for immobilization of specimen on the tip of CNH using noncovalent interaction.

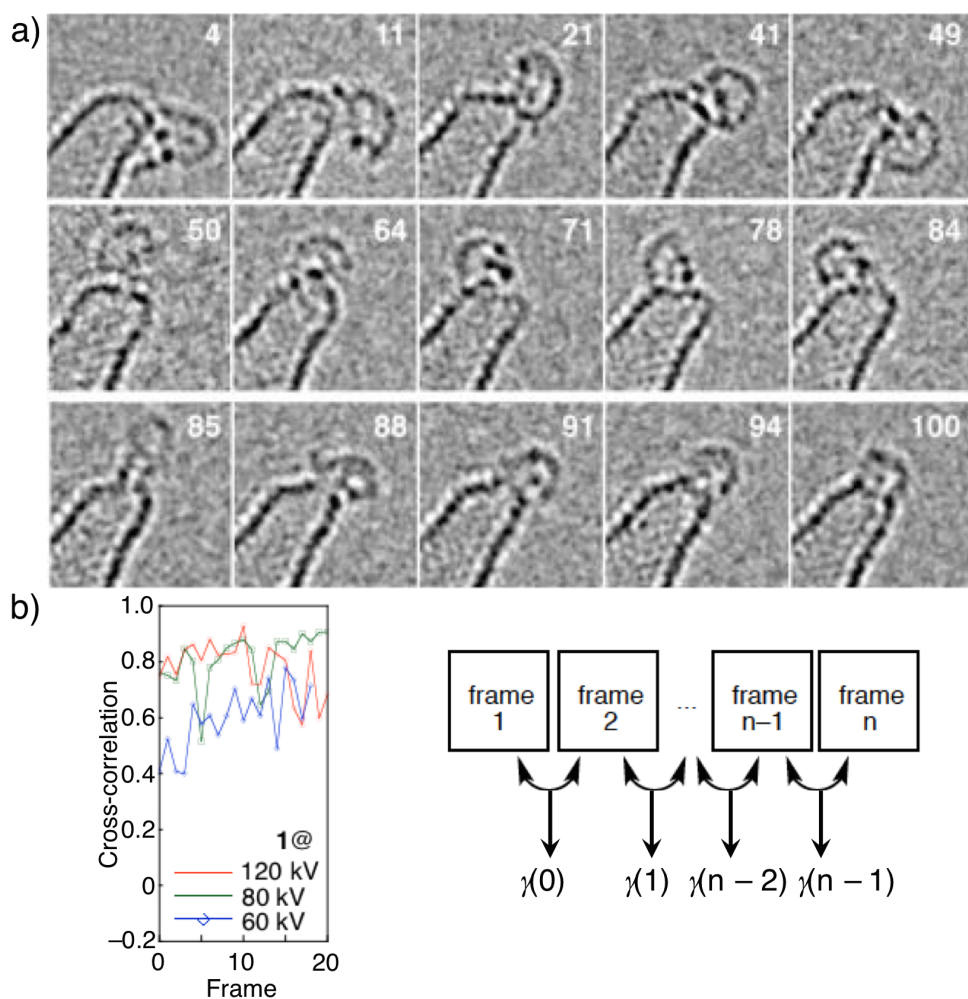


**Figure 1-9.** Quantification of molecular dynamics of specimens observed by TEM. (a) Representative sequential TEM images of biotinylated molecule. (b) Cross correlation calculated from consecutive frames of the movie of TEM images in a. Reprinted from ref. 38c Copyright © 2015 American Chemical Society.

## 1.4. References

- <sup>1</sup> Nagarajan, R. *Langmuir* **1991**, *7*, 2934–2969.
- <sup>2</sup> (a) Szola, F. Jr. *Ann. Rev. Biophys. Bioeng.* **1980**, *9*, 467–508. (b) Weissig, V. *Liposomes Methods and Protocols Volume 1: Pharmaceutical Nanocarriers*, Humana Press, New York, 2010.
- <sup>3</sup> (a) Moffitt, M.; Khougaz, K.; Eisenberg, A. *Acc. Chem. Res.* **1996**, *29*, 95–102. (b) Antonietti, M.; Fuöster, S. *Adv. Mater.* **2003**, *15*, 1323–1333.
- <sup>4</sup> (a) Lum, K.; Chandler, D.; Weeks, J. D. *J Phys. Chem. B* **1999**, *103*, 4570–4577. (b) Maibaum, L.; Dinner, A. R.; Chandler, D. *J. Phys. Chem. B* **2004**, *108*, 6778–6781. (c) Israelachvili, J. N.; Mitchell, D. J.; Ninham, B. W. *J. Chem. Soc., Faraday Trans 2* **1976**, *72*, 1525–1568.
- <sup>5</sup> Israelachvili, J. N. *Intermolecular and surface forces*, Revised 3rd Edition, Academic Press, London, 2011.
- <sup>6</sup> Menger, F. M.; Zhang, H. *J. Am. Chem. Soc.* **2006**, *128*, 1414–1415.
- <sup>7</sup> (a) Blume, G.; Vevc, G. *Biochim. Biophys. Acta Biomembranes* **1990**, *1029*, 91–97. (b) Soppimath, K. S.; Aminabhavi, T. M.; Kulkarni, A. R.; Rudzinski, W. E. *J. Controlled Release* **2001**, *70*, 1–20. (c) Narang, A. S.; Delmarre, D.; Gao, D. *Int. J. Pharm.* **2007**, *345*, 9–25.
- <sup>8</sup> (a) Gust, D.; Moore, T. A.; Moore, A. L. *Acc. Chem. Res.* **2001**, *34*, 40–48. (b) Voskuhl, J.; Ravoo, B. J.; *Chem. Soc. Rev.* **2009**, *38*, 495–505. (c) Nalluri, A. K. M.; Voskuhl, J.; Bultema, J. B. Boekema, E. J., Ravoo, B. J. *Angew. Chem. Int. Ed.* **2011**, *50*, 9747–9751.
- <sup>9</sup> Petkau-Milroy, K.; Brunsveld, L. *Org. Biomol. Chem.* **2013**, *11*, 219–232.
- <sup>10</sup> (a) Drummond, D. C.; Meyer, O.; Hong, K.; Kirpotin, D. B.; Papahadjopoulos, D. *Pharm. Rev.* **1999**, *51*, 691–744. (b) Dreher, M. R.; Liu, W.; Michelich, C. R. Dewhirst, M. W.; Yuan, F.; Chilkoti, A. *J. Natl. Cancer Inst.* **2006**, *98*, 335–344. (c) Perrault, S. D.; Walkey, C.; Jennings, T.; Fischer, H. C.; Chan, W. C. W. *Nano Lett.* **2009**, *9*, 1909–1915.
- <sup>11</sup> Lian, T.; Ho, R. J. Y. *J. Pharm. Sci.* **2001**, *90*, 667–680.
- <sup>12</sup> (a) Voskuhl, J.; Stuart, M. C. A.; Ravoo, B. J. *Chem. Eur. J.* **2010**, *16*, 2790–2796. (c) Lee, H.-K.; Park, K. M.; Jeon, Y. J.; Kim, D.; Oh, D. H.; Kim, H. S.; Park, C. K.; Kim, K. *J. Am. Chem. Soc.* **2005**, *127*, 5006–5007.
- <sup>13</sup> Thomas, G. B.; Rader, L. H. Park, J.; Abezgauz, L.; Danino, D.; DeShong, P.; English, D. S. *J. A. Chem. Soc.* **2009**, *131*, 5471–5477.
- <sup>14</sup> (a) Kroto, H. W.; Heath, J. R.; O'Brien, S. C.; Curl, R. F.; Smalley, R. E. *Nature* **1985**, *318*, 162–163. (b) Diederich, F.; Whetten, R. L. *Acc. Chem. Res.* **1992**, *25*, 119–126.
- <sup>15</sup> (a) Iijima, S. *Nature* **1991**, *354*, 56–58. (b) Bethune, D. S.; Kiang, C. H.; Vries, M. S. D.; Gorman, G.; Savoy, R.; Vazquez, J.; Beyers, R. *Nature* **1993**, *363*, 605–606.
- <sup>16</sup> Novoselov, K. S.; Geim, A. K.; Morozov, S. V.; Jiang, D.; Zhang, Y.; Dubonos, S. V.; Grigorieva, I. V.; Firsov, A. A. *Science* **2004**, *306*, 666–669.
- <sup>17</sup> (a) Dresselhaus, M. S.; Dresselhaus, G.; Eklund, P. C. *Science of Fullerenes and Carbon Nanotubes*, Academic Press, San Diego, 1996. (b) Misewich, J. A.; Martel, R.; Avouris, Ph.; Tsang, J. C.; Heinze, S.; Tersoff, J. *Science* **2003**, *300*, 783–786. (c) Shao, Y.; Wang, J.; Wu, H.; Liu, J.; Aksay, I. A.; Lin, Y. *Electroanalysis* **2010**, *22*, 1027–1036.
- <sup>18</sup> (a) Vigolo, B.; Pénicaud, A.; Coulon, C.; Sauder, C.; Paillet, R.; Journet, C.; Bernier, P.; Poulin, P. *Science* **2000**, *290*, 1331–1334. (b) Stankovich, S.; Dinkin, D. A.; Dommett, G. H. B.; Kohlhaas, K. M.; Zimney, E. J.; Stach, E. A.; Piner, R. D.; Nguyen, S. T.; Ruoff, R. S. *Nature* **2006**, *442*, 282–

## Chapter 1

286.

<sup>19</sup> Islam, M. F.; Rojas, E.; Bergey, D. M.; Johnson, A. T.; Yodh, A. G. *Nano Lett.* **2003**, *3*, 269–273.

<sup>20</sup> (a) Sun, D.; Tham, F. S.; Reed, T. C.; Chaker, L.; Burgess, M.; Boyd, P. D. W. *J. Am. Chem. Soc.* **2000**, *122*, 10704–10705. (b) Murakami, H.; Nomura, T.; Nakashima, N. *Chem. Phys. Lett.* **2003**, *378*, 481–485. (c) Geng, J.; Jung, H.-T. *J. Phys. Chem. C* **2010**, *114*, 8227–8234.

<sup>21</sup> Kang, Y.; Taton, A. *J. Am. Chem. Soc.* **2003**, *125*, 5650–5651.

<sup>22</sup> (a) Chen, R. J.; Zhang, Y.; Wang, D.; Dai, H. *J. Am. Chem. Soc.* **2001**, *123*, 3838–3839. (b) Matsuo, Y.; Morita, K.; Nakamura, E. *Chem. Asian. J.* **2008**, *3*, 1350–1357. (c) Zhu, J.; Yudasaka, M.; Zhang, M.; Kasuya, D.; Iijima, S. *Nano Lett.* **2003**, *3*, 1239–1243.

<sup>23</sup> (a) Sinnokrot, M. O.; Sherrill, C. D. *J. Phys. Chem. A* **2006**, *110*, 10656–10668. (b) Kawase, T.; Kurata, H. *Chem. Rev.* **2006**, *106*, 5250–5273.

<sup>24</sup> Denis, P. A. *New J. Chem.* **2014**, *38*, 5608–5616.

<sup>25</sup> (a) Atwood, J. L.; Koutsantonis, G. A.; Raston, C. L. *Nature* **1994**, *368*, 229–231. (b) Wang, J.; Gutsche, C. D. *J. Am. Chem. Soc.* **1998**, *120*, 12226–12231.

<sup>26</sup> Yoshida, Z.; Takekuma, H.; Takekuma, S.; Matsubara, Y. *Angew. Chem., Int. Ed.* **1994**, *33*, 1597–1599.

<sup>27</sup> Schneider, H.-J. *Angew. Chem. Int. Ed.* **1991**, *30*, 1417–1436.

<sup>28</sup> (a) Kawase, T.; Tanaka, K.; Seirai, Y.; Shiono, N.; Oda, M. *Angew. Chem. Int. Ed.* **2003**, *42*, 5597–5600. (b) Iwamoto, T.; Watanabe, Y.; Sadahiro, T.; Haino, T.; Yamago, S. *Angew. Chem. Int. Ed.* **2011**, *50*, 8342–8344. (c) Matsuno, T.; Sato, S.; Iizuka, R.; Isobe, H. *Chem. Sci.* **2015**, *6*, 909–916.

<sup>29</sup> (a) Stankovich, S.; Piner, R. D.; Chen, X.; Wu, N.; Nguyen, S. T.; Ruoff, R. S. *J. Mater. Chem.* **2006**, *16*, 155–158. (b) Ehli, C.; Rahman, G. M. A.; Jux, N.; Balbinot, D.; Guldi, D. M.; Paolucci, F.; Marcaccio, M.; Paolucci, D.; Melle-Franco, M.; Zerbetto, F.; Campidelli, S.; Prato, M. *J. Am. Chem. Soc.* **2006**, *128*, 11222–11231. (c) Xu, Y.; Bai, H.; Lu, G.; Li, C.; Shi, G. *J. Am. Chem. Soc.* **2008**, *130*, 5856–5857.

<sup>30</sup> Vaisman, L.; Wagner, H. D.; Marom, G. *Adv. Colloid Interface Sci.* **2006**, *128–130*, 37–46.

<sup>31</sup> Massover, W. H. *Micron* **2011**, *42*, 141–151.

<sup>32</sup> (a) Cumings, J.; Zettl, A. *Science* **2000**, *289*, 602–604. (b) Monthieux, M. *Carbon* **2002**, *40*, 1809–1823. (c) Khlobystov, A. N.; Britz, D. A.; Briggs, G. A. D. *Acc. Chem. Res.* **2005**, *38*, 901–909. (d) Liu, Z.; Yanagi, K.; Suenaga, K.; Kataura, H.; Iijima, S. *Nat. Nanotechnol.* **2007**, *2*, 422–425.

<sup>33</sup> Khlobystov, A. N.; Porfyrakis, K.; Kanai, M.; Britz, D. A.; Ardavan, A.; Shinohara, H.; Dennis, T. J. S.; Briggs, G. A. D. *Angew. Chem. Int. Ed.* **2004**, *43*, 1386–1389.

<sup>34</sup> (a) Koshino, M.; Niimi, Y.; Nakamura, E.; Kataura, H.; Okazaki, T.; Suenaga, K.; Iijima, S. *Nat. Chem.* **2010**, *2*, 117–124. (b) Nakamura, E.; Koshino, M.; Saito, T.; Niimi, Y.; Suenaga, K.; Matsuo, Y. *J. Am. Chem. Soc.* **2011**, *133*, 14151–14153.

<sup>35</sup> (a) Koshino, M.; Tanaka, T.; Solin, N.; Suenaga, K.; Isobe, H.; Nakamura, E. *Science* **2007**, *316*, 853. (b) Solin, N.; Koshino, M.; Tanaka, T.; Takenaga, S.; Kataura, H.; Isobe, H.; Nakamura, E. *Chem. Lett.* **2007**, *36*, 1208–1209. (c) Koshino, M.; Tanaka, T.; Solin, N.; Suenaga, K.; Isobe, H.; Nakamura, E. *Nat. Nanotechnol.* **2008**, *3*, 595–597. (d) Harano, K.; Takenaga, S.; Okada, S.; Niimi,

## Chapter 1

Y. Yoshikai, N.; Isobe, H.; Suenaga, S.; Kataura, H.; Koshino, M.; Nakamura, E. *J. Am. Chem. Soc.* **2014**, *136*, 466–473.

<sup>36</sup> Iijima, S.; Yudasaka, M.; Yamada, R.; Bandow, S.; Suenaga, K.; Kokai, F.; Takahashi, K. *Chem. Phys. Lett.* **1999**, *309*, 165–170.

<sup>37</sup> Isobe, H.; Tanaka, T.; Maeda, R.; Noiri, E.; Solin, N.; Yudasaka, M.; Iijima, S.; Nakamura, E. *Angew. Chem. Int. Ed.* **2006**, *45*, 6676–6680.

<sup>38</sup> (a) Nakamura, E.; Koshino, M.; Tanaka, T.; Niimi, Y.; Harano, K.; Nakamura, Y.; Isobe, H. *J. Am. Chem. Soc.* **2008**, *130*, 7808–7809. (b) Harano, K.; Homma, T.; Niimi, Y.; Koshino, M.; Suenaga, K.; Leibler, L.; Nakamura, E. *Nat. Mater.* **2012**, *11*, 877–881. (c) Gorgoll, R. M.; Yücelen, E.; Kumamoto, A.; Shibata, N.; Harano, K.; Nakamura, E. *J. Am. Chem. Soc.* **2015**, *137*, 3474–3477.

## *Chapter 1*



— Chapter 2 —

**Hierarchical Construction of Protein-Coated Capsule by Orthogonal  
Noncovalent Interactions**

## Chapter 2

This chapter was published in the following paper and reproduced with the permission from 2015 WILEY-VCH Verlag GmbH & Co. KGaA, Weinheim.

“High-Density Display of Protein Ligands on Self-Assembled Capsules via Noncovalent Fluorous Interactions” Harano, K.; Yamada, J.; Mizuno, S.; Nakamura, E.; *Chem. Asian J.* **2015**, *10*, 172–176.

## 2.1. Introduction: Fullerene Vesicle and the Surface Modification

Sub-100 nm-sized nanocapsules are very attractive as a drug carrier due to the capsular structure and the suitable size to avoid metabolization in human body.<sup>1</sup> Conventionally, liposomes made of lipid amphiphiles (molecules composed of polar head and nonpolar tail (s)) and polymersomes made of amphiphilic polymers are used as a drug carrier in pharmacotherapy.<sup>2</sup> Ligand display on the surface of the self-assembled capsules enables them to bind to a specific membrane protein of target diseased cells for the efficacy control. However, immobilization of the protein ligands into a membrane of the self-assembled capsules, especially liposomes, often destabilizes the membrane structure due to competitive interactions between the membrane formation and the ligand immobilization.<sup>3</sup> Polymersomes also have a problem in the clinical usages, because polymers are usually difficult to be metabolized and tend to remain in tissues to cause toxic effects. The desirable features of the nanocapsules for practical application are 1) being composed of small molecules, 2) having robust membrane to tolerate further functionalization, and 3) being easily modified.

Nakamura et al. reported that water-soluble pentasubstituted [60]fullerene amphiphiles ( $R_5C_{60}^- K^+$ ) form sub-100 nm-sized self-assembled vesicles in water (Figure 2-1).<sup>4</sup> The amphiphiles are composed of ternary architecture of alkyl or (perfluoro)alkyl side chains (nonpolar), potassium cyclopentadienide (polar), and fullerene core (nonpolar).<sup>4b</sup> The functional groups are synthetically introduced to the *para*-position of the substituted benzene ring. Due to the robust molecular structure of the fullerene core, the amphiphiles self-assemble into mechanically stable bilayer or interdigitated bilayer fullerene vesicles via  $\pi$ - $\pi$  interaction. In addition, the substituted groups of the fullerene amphiphile are exposed to outside of the vesicle in water even though these are hydrophobic (perfluoro)alkyl groups.<sup>5</sup> Therefore, the surface of the vesicle can be functionalized by designing the substituted groups of the fullerene amphiphiles. Formation of the vesicles was analyzed by not only light scattering in solution but also electron microscopy such as scanning electron microscopy (SEM) and transmission electron microscopy (TEM) under vacuum. Due to the high stability of fullerenes and the structure robustness of the vesicles, the vesicular structure is maintained on substrates after drying, and the surface nanostructures were clearly observed in SEM.

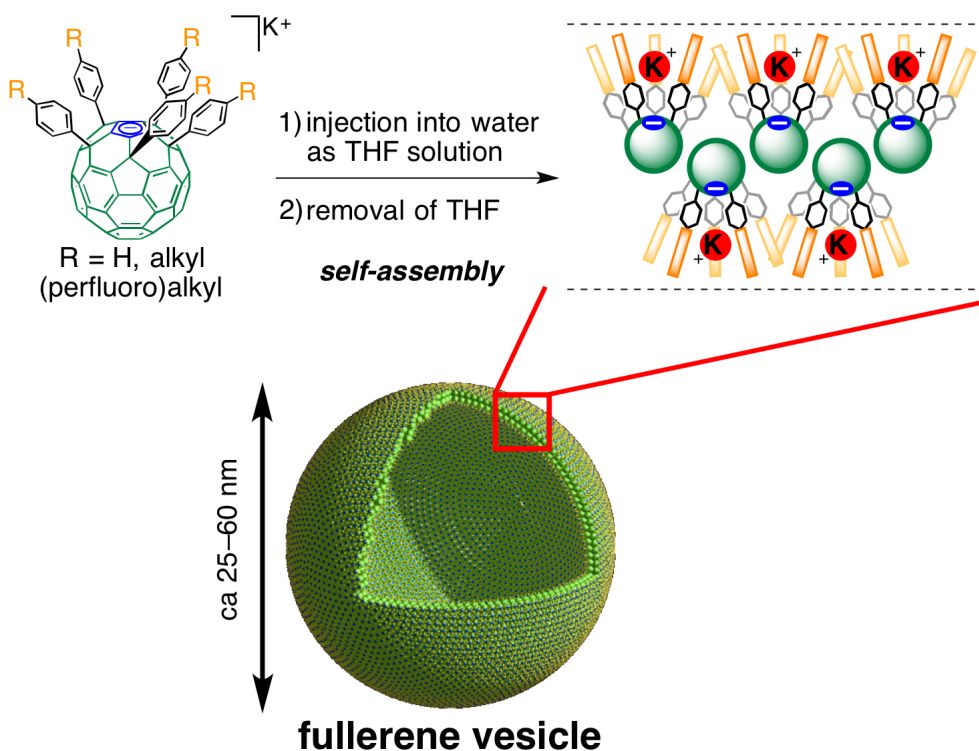


**Figure 2-1.** Fullerene vesicle composed of water-soluble pentasubstituted fullerene amphiphiles.

Previously, Nakamura et al. reported a covalent construction method using Huisgen cycloaddition reaction of alkynyl vesicle, **C8(7Y)K** vesicle, and azide-terminated biotin molecule.<sup>6</sup> They demonstrated binding of avidin on the vesicle surface. Structural robustness of the fullerene vesicle enabled the surface modification and the following protein binding at post-formation of the vesicular structure. The adsorbed avidin on the surface of vesicle was clearly observed by extreme high resolution SEM without dissociation of the vesicle (Figure 2-2). Doxorubicin, an anticancer drug, was delivered into HepG2 cell (liver carcinoma) *in vitro* by encapsulation into the inner cavity of biotinylated fullerene vesicle and showed cytotoxicity, but the fullerene vesicle did not show cytotoxicity. Other fullerene vesicle composed of  $\text{Ph}_5\text{C}_{60}^-\text{K}^+$  also showed low cytotoxicity.<sup>7</sup> However, isolation of the biotin-coated vesicle is necessary after the Huisgen cycloaddition reaction, and the efficacy of the cycloaddition reaction was low (20% based on the alkynyl group). I surmised that development of noncovalent surface modification method of fullerene vesicles would solve this operation issue. In this chapter, I demonstrate that a noncovalent fluorous modification method enabled dense functionalization of the surface of fullerene vesicle.

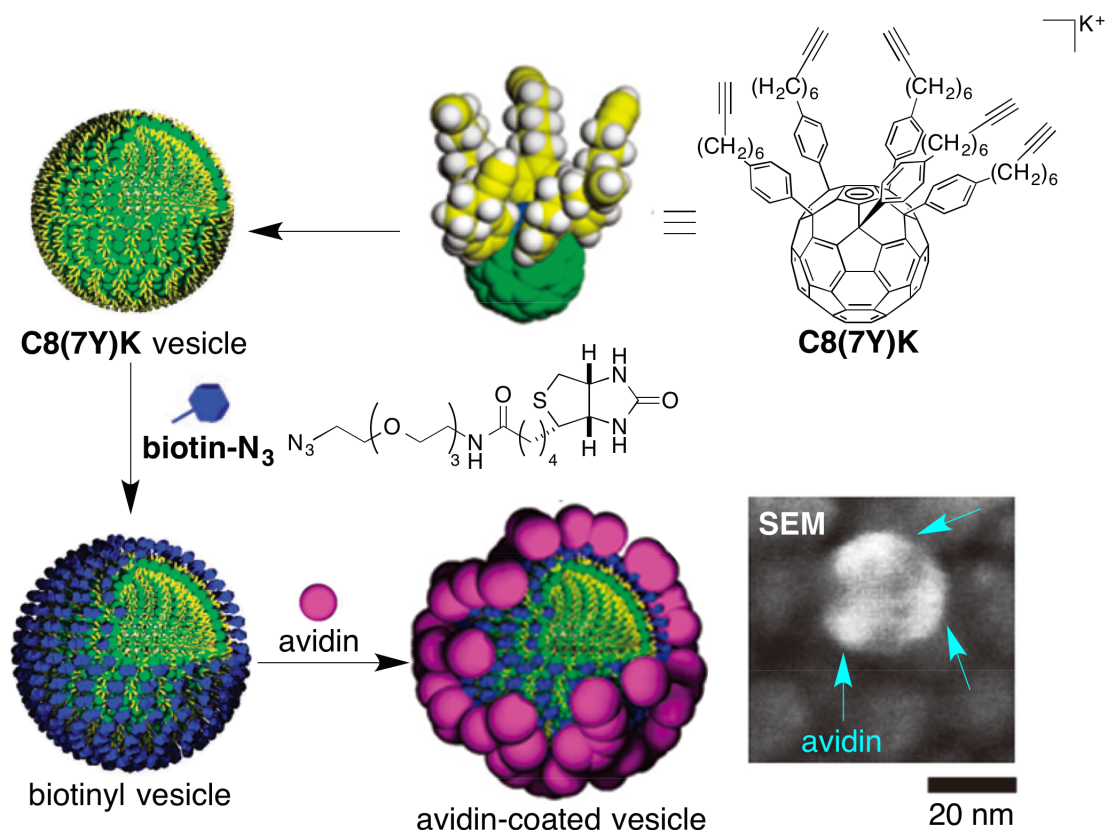


**Figure 2-2.** Formation and SEM imaging of protein-coated nanocapsules. Preparation of a biotinylated fullerene vesicle from fullerene amphiphile **C8(7Y)K** via Huisgen cycloaddition reaction and conjugation with avidin. (Right bottom) SEM images of avidin-coated vesicles coated on a microcrystalline ITO (indium-tin oxide)/glass substrate, Pale blue arrows denote avidin molecules. The SEM image is reprinted from ref. 6 with permission of The Royal Society of Chemistry.

Fluorous fullerene vesicle **V1** composed of water-soluble fluorous fullerene amphiphile **F8K** ( $R_5C_{60}^-K^+$ ,  $R = 4\text{-heptadecafluorooctylphenyl}$ , Figure 2-3) has large potential as a template for ligand display because of the fluorous nature. **F8K** self-assembles in water and forms vesicular structure with exposing their (perfluoro)octyl chains to an outer aqueous phase. Since fluorous compounds are specifically dissolved in fluorous solvents rather than water and non-fluorous organic solvents due to the small dielectric constant, fluorous-tagged (FT) molecules that are molecules bearing a perfluoroalkyl group, can be immobilized on fluorous surface in a noncovalent manner. It is known that FT-saccharides can be easily immobilized on the surface of a fluorous-modified glass slide<sup>8</sup> and a polytetrafluoroethylene membrane filter<sup>9</sup>, both of which have highly fluorinated surface, via fluorous interaction.<sup>10</sup> This immobilization method is applied to a simple ways of solid-phase synthesis of polysaccharide<sup>11</sup>, production of microarray<sup>8</sup>, and detection of virus<sup>9</sup>.

Herein, I applied this fluorous modification method for ligand display on vesicle **V1** to develop more facile noncovalent surface modification methods of self-assembled nanocapsule without

destabilization of the membrane structure. The ternary architecture of **F8K** enables to use orthogonal noncovalent interactions for membrane formation of **V1** ( $\pi$ - $\pi$  interaction) and ligand display on the surface of **V1** (fluorous interaction). In addition, due to the immiscibility of (perfluoro)alkyl group, alkyl group, and properly designed FT-ligand molecules can be effectively displayed on the surface of the vesicle for the following protein binding. These well-constructed molecular designs in both the vesicle and the ligand molecule developed a non-invasive method for ligand display and protein binding on self-assembled nanocapsule. A part of this research has been already reported in my master theses.<sup>12</sup>

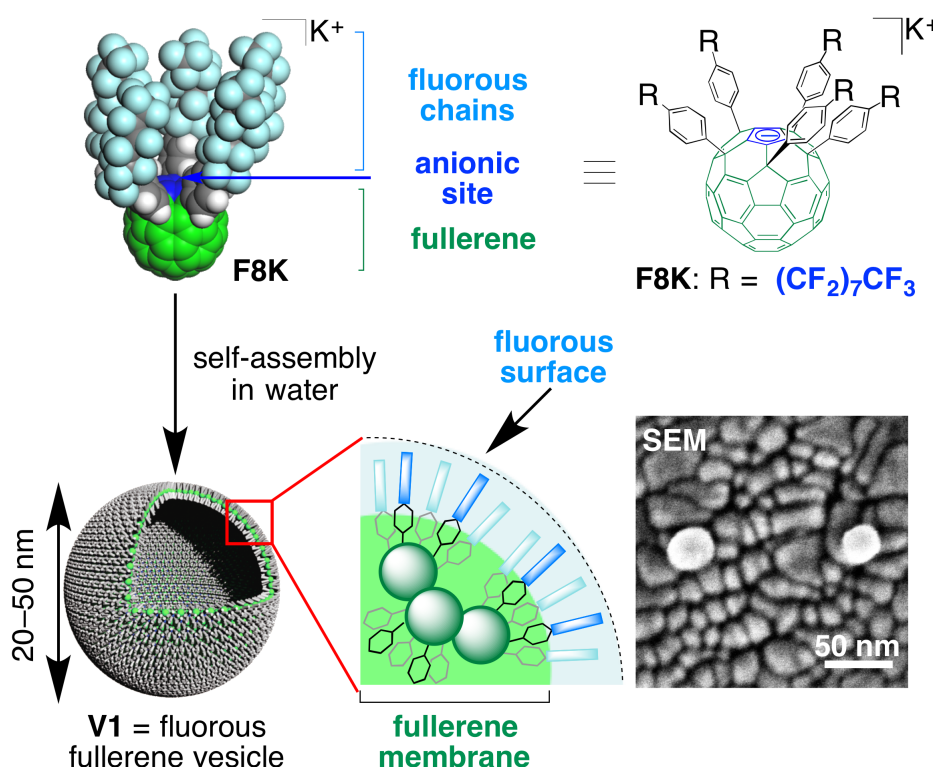


**Figure 2-3.** A fluorinated fullerene vesicle **V1** composed of water-soluble fluorinated fullerene **F8K**. SEM images of **V1** coated on a microcrystalline ITO/glass substrate.

## 2.2. Preparation of Fullerene Vesicles and FT Molecules

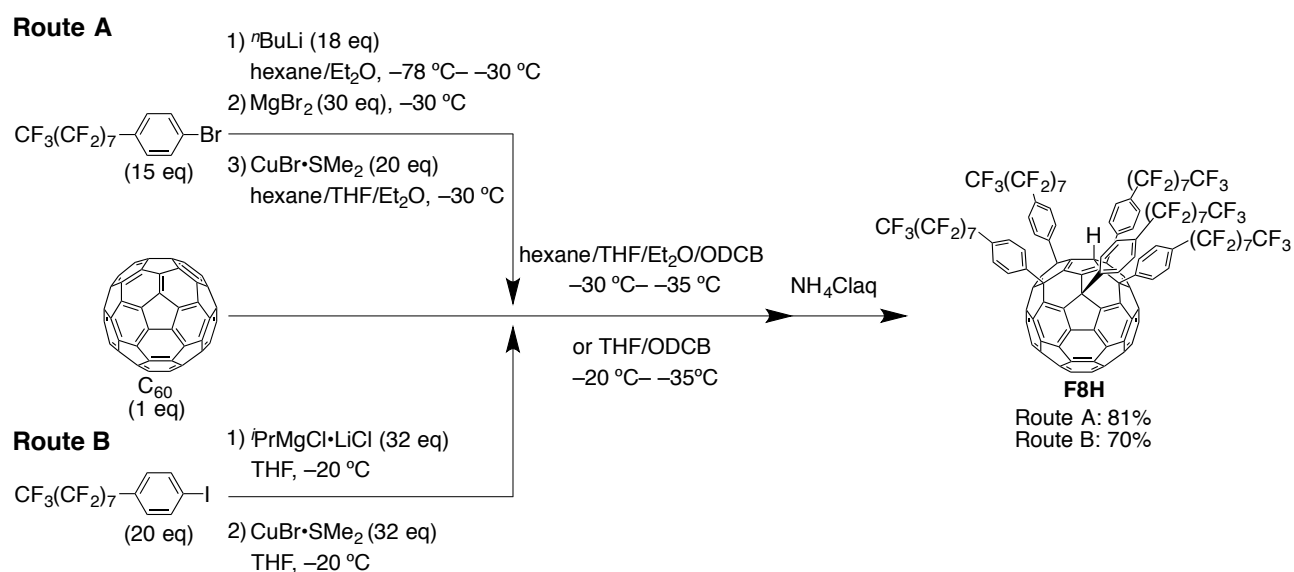
### 2.2.1. Synthesis of Fluorous Fullerene Amphiphile and FT Ligand Molecules

Penta(4-heptafluorooctylphenyl)[60]fullerene (**F8H**,  $R_5C_{60}H$ ,  $R =$  4-heptafluorooctylphenyl) as a precursor of fullerene amphiphile **F8K** was firstly reported by Nakamura et al. in 2010.<sup>5</sup> **F8H** was synthesized by pentaaddition reaction of [60]fullerene with 1-bromo-4(heptafluorooctyl)benzene through three organometallic intermediates, organolithium, organomagnesium, and organocopper derivatives of 1-bromo-4(heptafluorooctyl)benzene (Route A in Scheme 2-1). However, the three-step synthesis for the organocopper precursor of **F8H** made the operation difficult and often reduced the

## Chapter 2

reproducibility of the reaction because of instability of organometallic intermediates made of 1-bromo-4(heptadecafluorooctyl)benzene. Therefore I modified the synthetic procedure of **F8H**. I prepared the organocopper precursor in one-pot using 4(heptadecafluorooctyl)-1-iodobenzene as a starting material and turbo Grignard reagent ( $^i\text{PrMgCl}\cdot\text{LiCl}$  complex)<sup>13</sup> to prepare the organomagnesium intermediate. **F8H** was synthesized this procedure with 70% yield and good reproducibility (Route B in Scheme 2-1). Penta(4-octylphenyl)[60]fullerene (**C8H**,  $\text{R}_5\text{C}_{60}\text{H}$ ,  $\text{R} = 4\text{-octylphenyl}$ ) was synthesized to prepare an aliphatic fullerene vesicle **V1C** for aliphatic template for ligand display by the reported procedure.<sup>4b</sup>

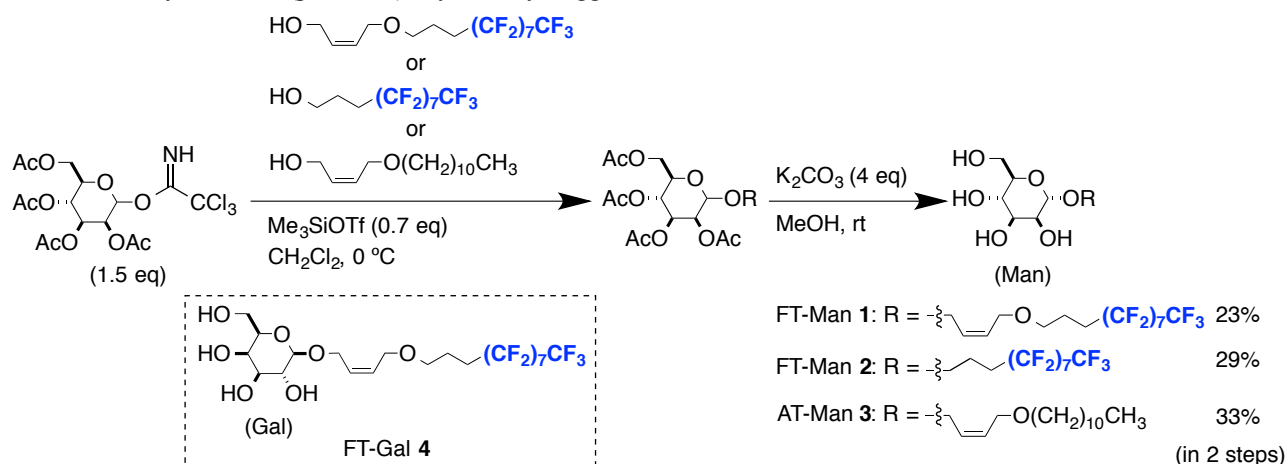
**Scheme 2-1.** Synthetic procedures of **F8H**.



Fluorous-tagged (FT)-mannopyranosides (**FT-Man 1** and **FT-Man 2**) and alkyl-tagged (AT)-mannopyranoside (**AT-Man 3**) were synthesized by reaction of 2,3,4,6-tetra-*O*-acetyl- $\alpha/\beta$ -D-mannopyranosidetrichloroacetimidate and the corresponding alcohols with reference of Pohl's group paper<sup>8</sup> (Scheme 2-2). **FT-Man 1** is composed of a (perfluoro)octyl group and a longer aliphatic tether than **FT-Man 2**. These two ligands were designed to elucidate the orientation of immobilization of the FT molecules on the fullerene vesicles. Pohl et al. reported that the properly designed length of aliphatic tether was necessary for binding to a protein on fluorous glass surface.<sup>8</sup> **AT-Man 3** is designed to elucidate the importance of fluorous interaction for functionalization. FT-galactopyranoside (**FT-Gal 4**, synthesized by Mr. Mizuno, S.) was used as another ligand molecule for evaluation of the protein binding ability of the fullerene vesicles.

## Chapter 2

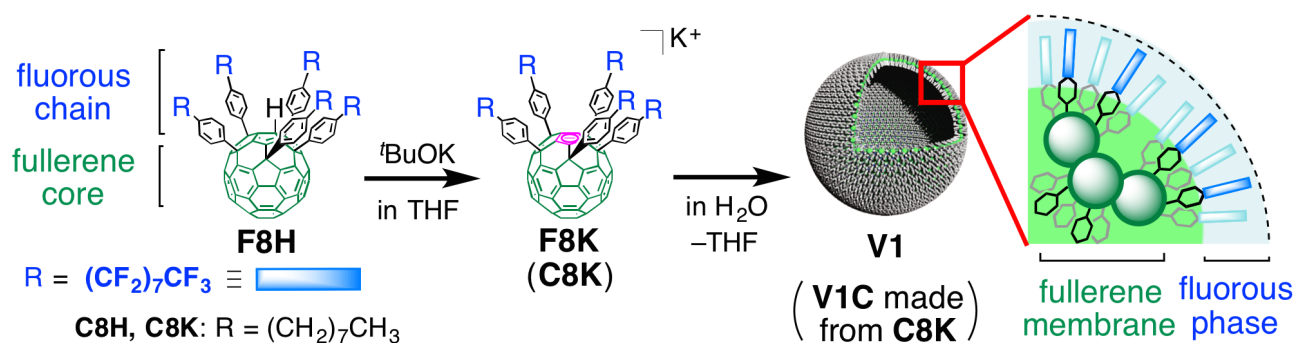
**Scheme 2-2.** Synthesis of (perfluoro)alkyl or alkyl-tagged saccharides.



### 2.2.2. Preparation of Fullerene Vesicles

Preparation of fullerene vesicle **V1** and **V1C** has been already reported by Nakamura group.<sup>4b</sup> Briefly, potassium salts of fullerene amphiphiles **F8K** (for **V1**) and **C8K** (for **V1C**) were prepared by deprotonation of **F8H** and **C8H** in THF, respectively. The solution of the potassium fullerene salt was slowly injected into water with stirring to obtain the vesicle solution. THF was removed by evaporation, and then the vesicle solution was diluted with water to adjust the concentration of the potassium fullerene salt to 1.0 mM in water (Scheme 2-3). The hollow vesicular structure of **V1** in water was confirmed previously through combined dynamic and static light scattering analysis.<sup>4</sup> The average diameter of the vesicle **V1** was determined to be  $27.0 \pm 0.5$  nm (polydispersity index (Pdl) of 0.15) by dynamic light scattering (DLS) measurement. The vesicle solution of **C8K** (**V1C** solution) was prepared by the same procedure and the concentration was adjusted to 1.0 mM. The average diameter of the vesicle **V1C** was determined to be  $23.8 \pm 0.1$  nm (Pdl: 0.15, Figure S2-1).

**Scheme 2-3.** Schematic illustration of preparation of fullerene vesicle **V1** and **V1C**.



### 2.3. Ligand Display on Fullerene Vesicles

Perfluorinated surface of vesicle **V1** was successfully modified with FT-Man **1** just by mixing the solutions (Figure 2-4). FT-Man **1** in water forms aggregates of an ill-defined  $\mu\text{m}$ -sized structure (Figure 2-4b, gray), and so do FT-Man **2** and the AT-Man **3** (See Figure S2-1 in supporting



information.) measured by DLS measurement. Upon mixing the solution of **1** into **V1** ( $[\mathbf{1}]:[\mathbf{F8K}] = 1:1$  mole ratio), the aggregates mostly disappeared, and instead there formed a uniform solution of **V2** that showed a DLS peak with an average diameter of  $32.8 \pm 0.8$  nm (PDI of 0.15, Figure 2-4b, red). Compared with the average diameter of **V1** ( $27.0 \pm 0.5$  nm, Figure 2-4b, black), the  $5.8 \pm 0.7$  nm increase in the diameter of **V2** indicates that the mannopyranoside and the alkyl tether moieties of **1** are displayed on the surface of **V1**. The size increase of **V1** is larger than the expected value from the molecular size of the mannopyranoside and the alkyl tether moieties of **1** (ca.  $1.5$  nm  $\times$  2 molecules =  $3.0$  nm), suggesting that **V1** was slightly swollen by insertion of the (perfluoro)octyl group of **1** into the membrane of **V1**.<sup>14</sup>

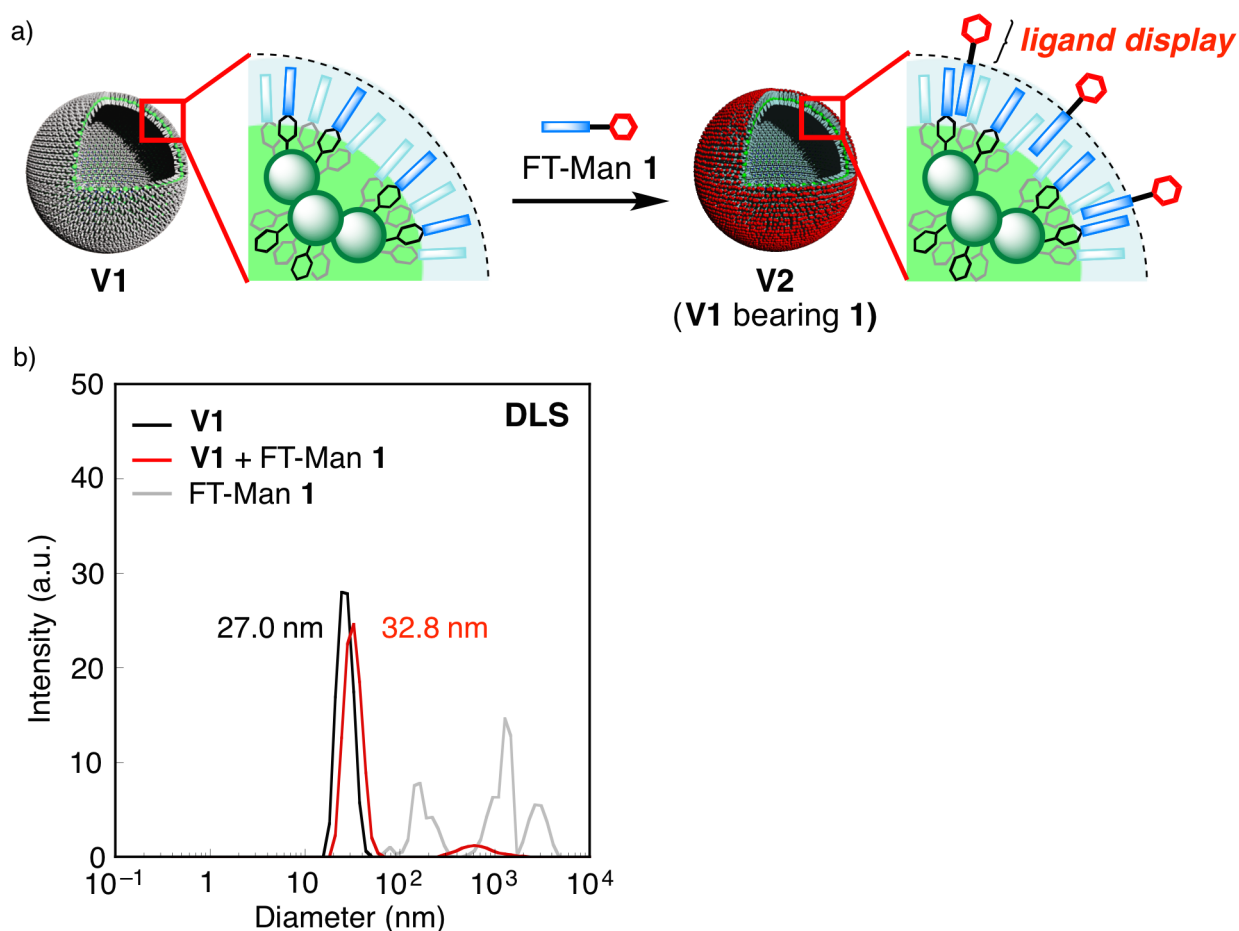


**Figure 2-4.** Surface coating of **V1** with FT-Man **1** in water. (a) Schematic illustration of display of **1** on **V1**, (b) DLS data for **V1** (black), an aggregate of **1** (gray) and a mixture of **V1** and **1** at  $[\mathbf{F8K}]:[\mathbf{1}] = 1:1$  mole ratio recorded at  $25$  °C. The zeta potentials of **V1** and **V2** ( $[\mathbf{F8K}]:[\mathbf{1}] = 1:5$  mole ratio) at pH 7.4 were  $-40$  mV and  $-60$  mV, respectively.

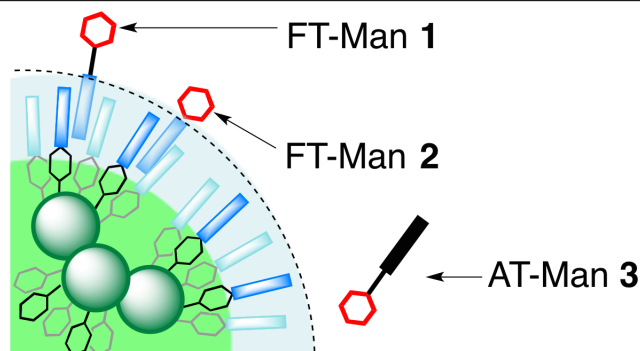
Ligand display on the fullerene vesicles was evaluated further with other combinations of the vesicle and the ligand molecule by size increase of the vesicles. The size increase of the vesicles upon binding of the ligand molecules is summarized in Table 2-1. Upon mixing FT-Man **2** that has short alkyl tether into the solution of vesicle **V1**, size increase corresponding to the

## Chapter 2

mannopyranoside moiety was detected. However mixing AT-Man **3** into the solution **V1** did not show size increase of **V1**. This result suggests that **3** was not adsorbed on the surface of **V1** due to the immiscibility of alkyl group of **3** and (perfluoro)alkyl group of **F8K**. When aliphatic fullerene vesicle **V1C** was used as a template for ligand display,  $3.1 \pm 0.2$  nm or  $3.3 \pm 0.2$  nm of size increase of **V1C** was detected by mixing FT-Man **1** or **3** into the solution of **V1C**, respectively. The value of size increase indicates that both **1** and **3** were adsorbed on the surface of **V1C** via hydrophobic interaction but did not induce swelling of **V1C** like combination of **V1** and **1**. I surmise that the (perfluoro)octyl group and octyl group of **1** and **3** were not inserted into the membrane of **V1C**, hence **V1C** modified with **1** or **3** does not show significant protein binding ability on the vesicle as shown in next section.

**Table 2-1.** Increase in the vesicle size upon addition of ligand molecules, e.g., by addition of **1** to **V1**. [fullerene] = [ligand] = 0.2 mM. Unit is nm. The measurement was carried out in triplicate and the error denotes standard error of mean. Original DLS data is shown in Figure S2-1 in supporting information.

<b>V1 + 1</b>	<b>V1 + 2</b>	<b>V1 + 3</b>	<b>V1C + 1</b>	<b>V1C + 3</b>
<b>5.8 ± 0.7</b>	1.1 ± 1.0	0.0 ± 0.6	3.1 ± 0.2	3.3 ± 0.2



The maximum amount of FT-Man **1** which can be adsorbed on the surface of vesicle **V2** was estimated by interfacial tension measurement using pendant drop method. Briefly, a droplet of sample solution was hanged on the tip of a syringe needle and interfacial tension of the sample was calculated by analysis of the shape of the droplet using the equation of Bashforth and Adams which is based on Laplace's equation (Figure S2-3).<sup>12b</sup> **F8K** amphiphile did not show interfacial activity because it does not exist as a monomer in water even though it was very low concentration ( $< 0.1$   $\mu\text{M}$ ) due to the formation of the rigid vesicle structure (Figure 2-5b). Therefore, the fullerene amphiphile is not adsorbed to the air-water interface and does not show interfacial activity. In contrast, since **1** is composed of hydrophilic mannopyranoside moiety and hydrophobic fluorine tag moiety, **1** shows surface activity in water as a surfactant. In water, **1** is adsorbed to air-water interface and decreases the interfacial tension (Figure 2-5a, B). In contrast, in **V1** solution, **1** is adsorbed to the fluorine surface of **V1** first, and after saturation on the surface of **V1**, **1** starts to be

## Chapter 2

adsorbed on the air-water interface and decreases the interfacial tension of **V1** solution. The maximum amount of **1** on **V1** was estimated by measuring difference in the critical aggregation concentration (CAC) that indicates saturation of the air-water interface of droplet of **1** in water ( $19.1 \pm 1.4$  mM, Figure 2-5c, red) and in **V1** solution ( $24.1 \pm 1.3$  mM, Figure 2-5c, blue). This difference of  $5.0 \pm 1.9$  mM in the CAC of **1** indicates the saturation (maximum) amount of **1** on the surface of **V1** ( $[\text{F8K}] = 1.0$  mM).

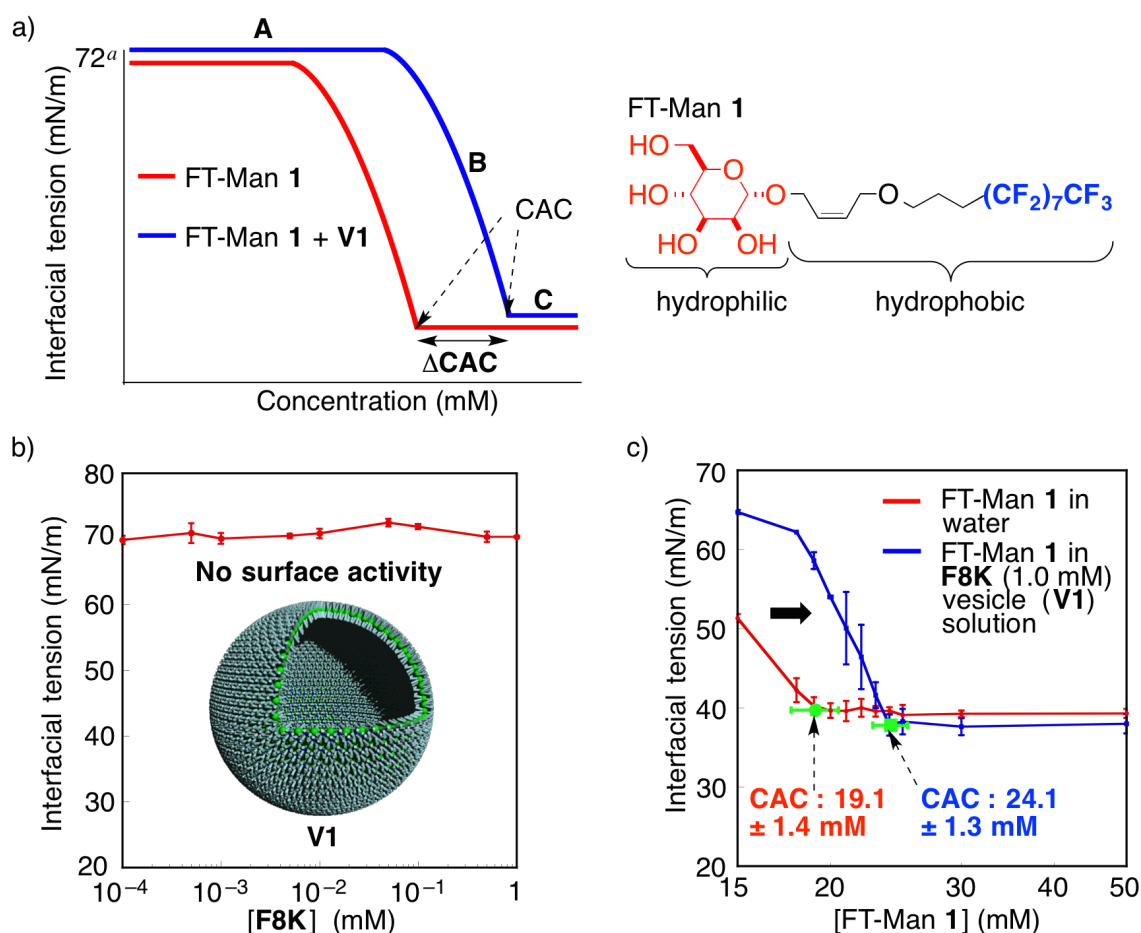


**Figure 2-5.** Quantitative evaluation of the amount of FT-Man **1** on the surface of vesicle **V1** by interfacial tension measurement using a pendant drop method. (a) Expected illustration of interfacial tension change upon increase of concentration of **1**. A: No change in interfacial tension (<sup>a</sup> interfacial tension of pure water at 25 °C), B: Decrease of interfacial tension due to adsorption of **1** to air-water interface, C: No change in interfacial tension due to saturation at air-water interface with **1**. (b) Interfacial activity of **V1** in water. (c) Interfacial activity of **1** in water (red) and **1** in a solution of vesicle **V1** (1.0 mM for **F8K**, blue). The measurement was carried out in triplicate and the error denotes standard error of mean. The CAC of **1** increases by  $5.0 \pm 1.9$  mM because of adsorption of **1** on **V1**.

Assuming that the water-soluble **1** does not penetrate the fullerene bilayer and according to molecular modeling of the membrane structure of **V2** saturated with **1** (Figure 2-6),<sup>6</sup> I conclude that approximately eight molecules of **1** per **F8K** are located outside, hence there were approximately three molecules of **1**/nm<sup>2</sup> on the surface of a vesicle (6890 molecules on **V1** with 27.0 nm diameter). FT-Gal **4** was also loaded on the surface of **V1** with the same maximum density as **1** (Figure 2-7).

## Chapter 2

The ligand molecules are densely packed at this density as we can see in the molecular modeling (Figure 2-6).

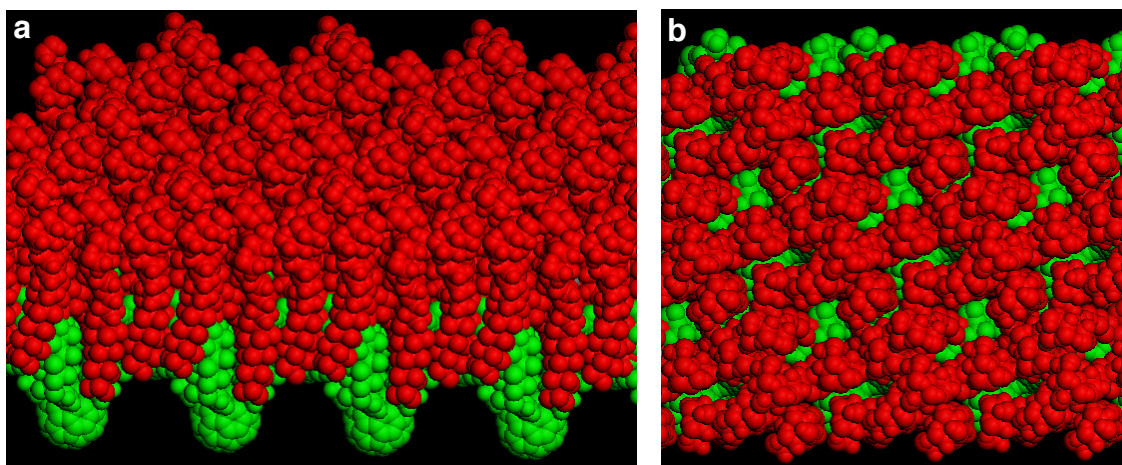


**Figure 2-6.** Molecular modeling of **V2** ( $[\text{F8K}]:[\text{1}] = 1:8$ ), where FT-Man **1** is densely packed on the **F8K** membrane. (a) Side view and (b) top view. The van der Waals models of **F8K** and **1** are shown in green and red, respectively. Potassium ions of **F8K** are omitted for clarity.

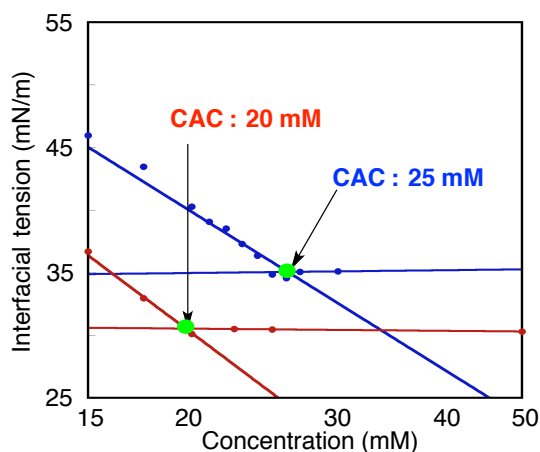


**Figure 2-7.** Interfacial tension measurements of FT-Gal **4**. Interfacial tension change in FT-Gal **4** in water (red) and **4** in a solution of vesicle **V1** (1.0 mM for **F8K**, blue). CAC values of **4** increased by 5 mM due to absorption of **4** on **V1**. This result suggests that the maximum loading ratio of **4** on **V1** is 5:1. Error bar means standard error ( $N=3$ ).

Structure robustness of vesicle **V2** in solution was evaluated by heating at 80 °C for 24 h traced visually and by DLS. Neither aggregation nor precipitation occurred. As studied by SEM (See Figure S2-2 in supporting information and Figure 2-14a.), **V2** maintains its spherical structure even in air and under vacuum conditions. The spherical structure was also maintained upon atomic force microscopic (AFM) analysis on mica in air (Figure 2-8a), and on scanning transmission electron microscopy (STEM) on a thin carbon film under vacuum (Figure 2-8b). Contrast profile of **V2** in the STEM image shows a unimodal curve (Figure 2-8b, right) that indicates that **V2** retained

the contents of the inside. From these results, therefore, **V2** is very robust like vesicle **V1**, suggesting that the immobilization of the fluoruous saccharides does not destabilize the bilayer membrane.<sup>5</sup>

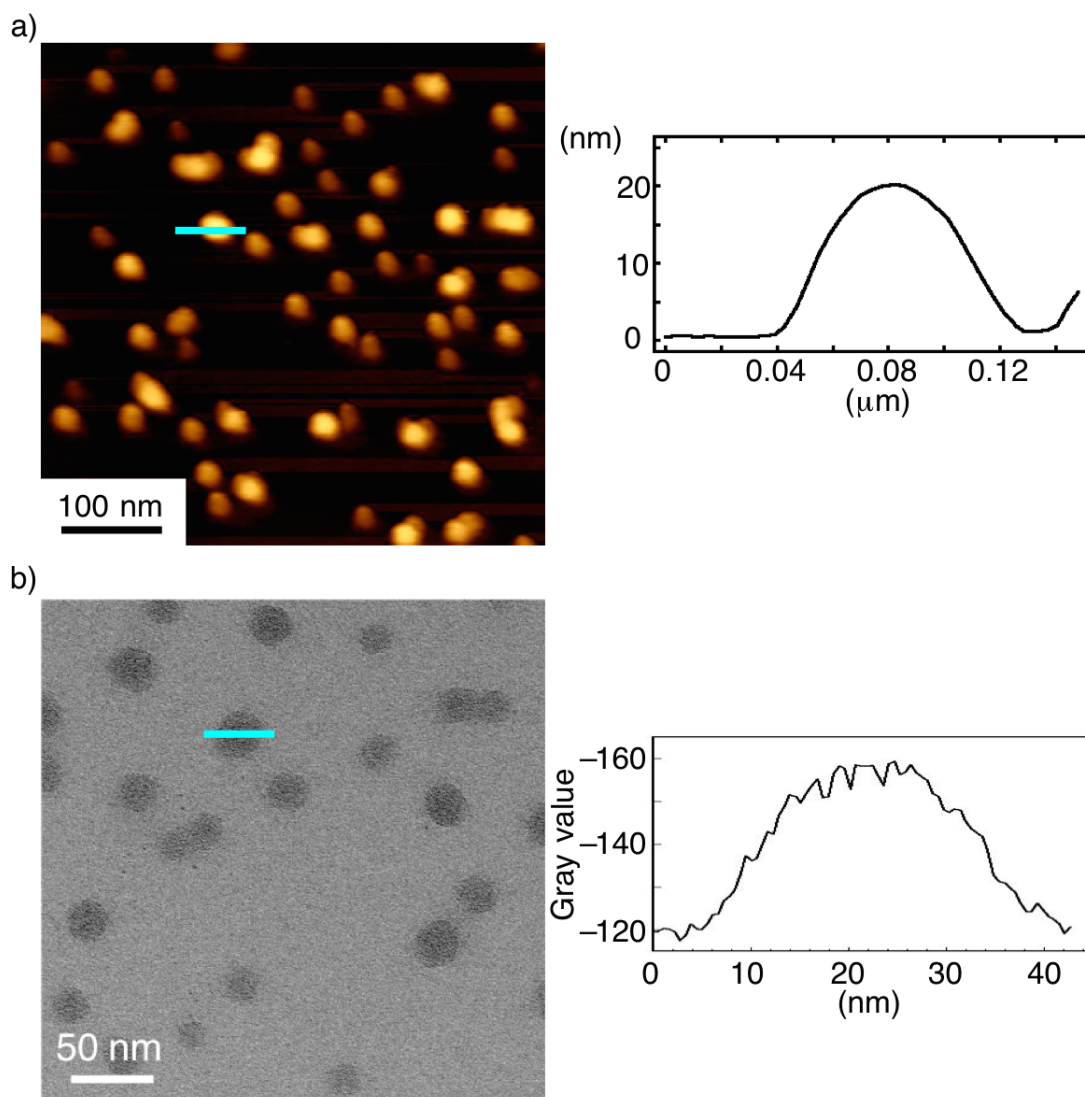


**Figure 2-8.** Microscopic images of **V2**. (a) AFM image of **V2** on mica. Cross section diagram of **V2** (right, pale blue line in the left image). (b) STEM image of **V2** on an amorphous carbon film (ca. 6 nm thickness) at an acceleration voltage of 200 kV. Contrast profile of **V2** (right, pale blue line in the left image).

## 2.4. Protein Binding on Ligand-Coated Fullerene Vesicles

Protein binding on ligand-coated fullerene vesicles with concanavalin A (ConA, a lectin binds to mannose) was next probed according to the known protocol for assessment of sugar–protein binding on a vesicle (Figure 2-9).<sup>15</sup> Addition of a buffer solution of ConA (2.0  $\mu\text{M}$ , pH 7.2) to a solution of **V2** (**V1** + FT-Man **1**; [**F8K**] = [**1**] = 20  $\mu\text{M}$ ) increases the turbidity of the solution due to spontaneous agglomeration of **V3** originating in the cross-linking of the vesicles via tetravalent ConA (Figure 2-9b, red).<sup>15</sup> Methyl  $\alpha$ -D-mannopyranoside (3,000 eq) was added as an inhibitor for binding between **1** and ConA after 20 min when the turbidity increase reached plateau. The

turbidity of the solution was decreased that means partially destroy of the network structure of **V3** agglomerates. This result indicates that ConA binds to the surface of **V1** via **1**. In contrast, **V1** bearing FT-Man **2** or AT-Man **3**, and **V1C** bearing **1** or **3** did not show significant turbidity increase after addition of ConA (Figure 2-10a).

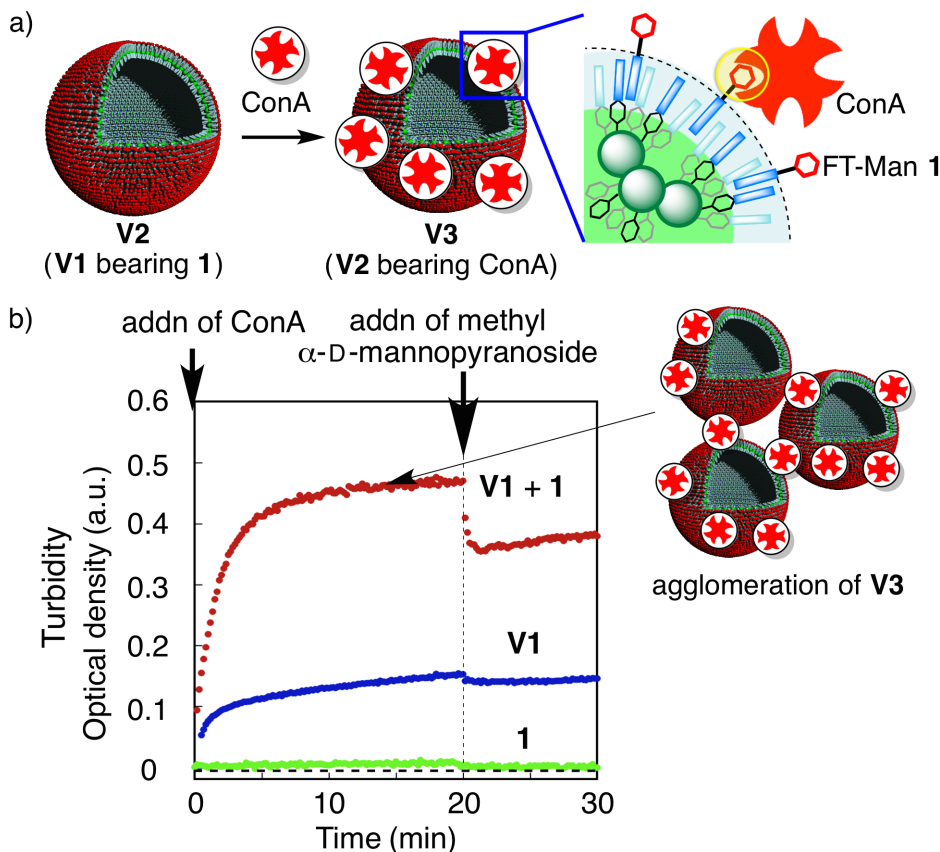


**Figure 2-9.** Time evolution of the turbidity of the solution upon addition of ConA to a mixture of **V1** and FT-Man **1**. The turbidity was monitored by measurement of the optical density at  $\lambda = 500$  nm ([fullerene] = 20  $\mu$ M). (a) Schematic illustration of ConA binding on vesicle **V2** (**V1** bearing **1**) via **1**. (b) Turbidity change for a mixture of **V1** and **1** ([**F8K**]:[**1**] = 1:1, red). Addition of 3,000 eq of methyl  $\alpha$ -D-mannopyranoside at 20 min resulted in a decrease in turbidity (red). The blue and the green lines are control experiments for **V1** and **1**, respectively. Photoabsorption of **F8K** is subtracted from the optical density as a background.

According to the size increase of **V1** upon the ligand display (Table 2-1), **2** was immobilized on the surface of **V1** but the mannopyranoside moiety was not properly displayed to bind to ConA (Figure 2-10b), and **3** was not immobilized on the surface of **V1**. Therefore ConA did not bind to these vesicles and no significant turbidity increase was observed (Figure 2-10a, gray and orange for **V1** + **2** and **V1** + **3**, respectively).

As shown in the section 2-3, size of **V1C** was increased upon mixing of **1** and **3** corresponding to display of the ligands on the surface of **V1C**. However, neither **V1C** bearing **1** (Figure 2-10a, green) nor **V1C** bearing **3** (Figure 2-10a, blue) showed significant turbidity increase. Mismatching alkyl-(perfluoro)alkyl combination of **C8K** of **V1C** and **1**, and alkyl-alkyl combination of **C8K** and **3** are too weak to immobilize ConA on the surface of the vesicles. These

ligand molecules are easily detached from the surface of the vesicles when hydrophilic ConA binds and makes the molecules dissolved into water (Figure 2-10c). As a result, it is obviously revealed that fluororous interaction enables proper ligand display and the following protein binding on the vesicle. Note that nonspecific binding of **V1** to the proteins exists but negligible (Figure 2-9b, blue).

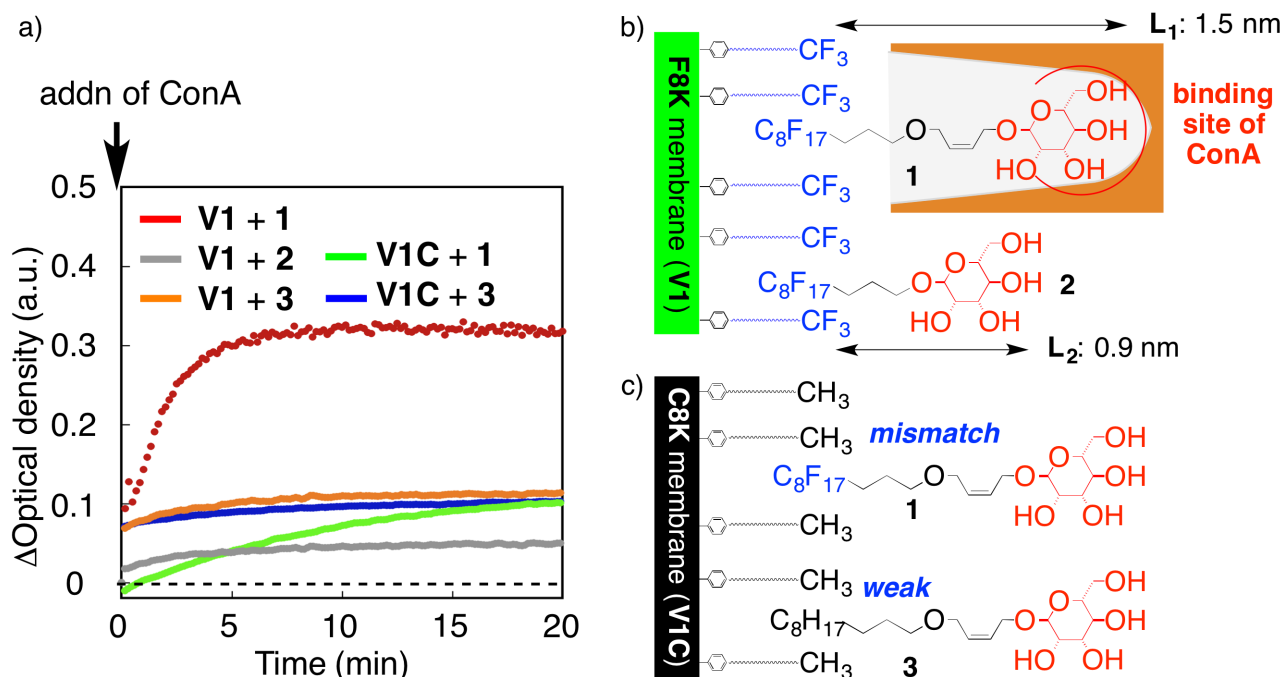


**Figure 2-10.** Time evolution of the turbidity of the solution upon addition of ConA to a mixture of **V1** or **V1C** and FT- or AT-Man. The turbidity was monitored by measurement of the optical density at  $\lambda = 500$  nm ([fullerene] = 20  $\mu$ M). (a) Turbidity change for a mixture of vesicle **V1** or **V1C**, and FT- or AT-Man ([fullerene]:[Man] = 1:1). The background contribution of the nonspecific binding to **V1** (Blue line in Figure 2-9b) is subtracted. Surface structure of ligand display on fullerene vesicles, (b) **V1** (**F8K** membrane), and (c) **V1C** (**C8K** membrane) expected by size increase of the vesicles upon mixing ligand molecules (Table 2-1).

I also confirmed that vesicle **V1** bearing FT-Gal **4** has strong interaction with peanut agglutinin (PNA, A protein binds to galactose.) by turbidity measurement (Figure 2-11). Then the protein binding selectivity was evaluated by using FT-Man- and FT-Gal-coated vesicles.<sup>12a</sup> Since the **V1** coated with **1** selectively binds to ConA (Figure 2-12a), the vesicle coated with **4** binds to PNA (Figure 2-12b). The lower selectivity in the experiment in Figure 2-12b is due to the poorer selectivity of ConA than PNA.<sup>16</sup> **V1** decorated with a 1:1 mixture of **1** and **4** bound to both ConA and PNA (Figure 2-12c). The slow rate of binding of PNA (Figure 2-12c, blue) is consistent with the reported data.<sup>17</sup> These results suggested that dual modification of **V1** with different ligand molecules was succeeded by just mixing each solution via fluororous interaction, and the dual-modified vesicle recognized two different proteins.

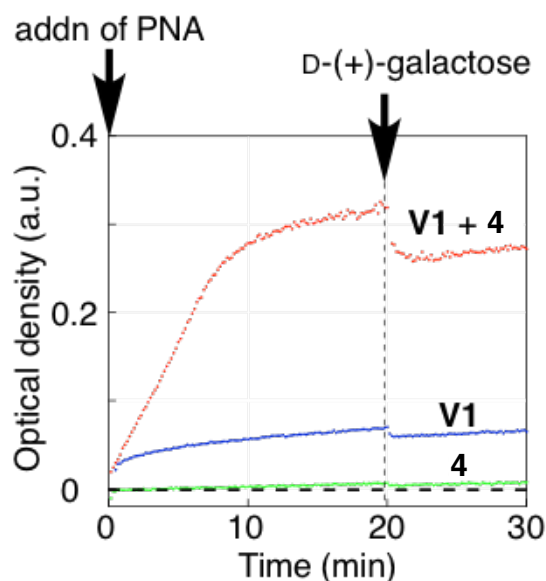


**Figure 2-11.** Time-dependent turbidity change after mixing proteins with ligand molecule-coated vesicles monitored by optical density at  $\lambda = 500$  nm. We started to record the optical density at the point of addition of proteins (0 min). Concentration of fullerene amphiphiles was fixed to 20 mM. Absorption of the **V1** at 500 nm was independently measured and subtracted from the optical density as a background. (a) Turbidity change upon mixing PNA with **V1** incorporating **4** ( $[\mathbf{F8K}]:[\mathbf{4}] = 1:1$ , red), and PNA with **V1** (blue). At 20 min, 1500 eq of D-(+)-galactose was added as an inhibitor of binding between **4** and PNA (dashed line).

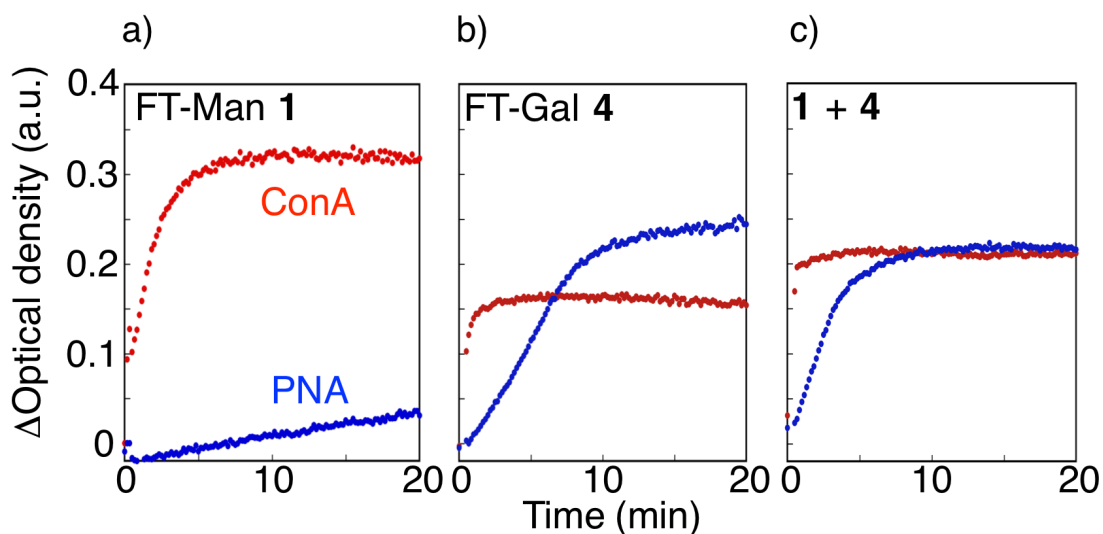


**Figure 2-12.** Recognition of two different proteins by **V1** decorated with FT-Man **1** and FT-Gal **4**. (a) Turbidity increase for **V1** + **1** and ConA (red) or PNA (blue) ( $[\mathbf{F8K}]:[\mathbf{1}] = 1:1$ ). (b) For **V1** + **4** and ConA or PNA ( $[\mathbf{F8K}]:[\mathbf{4}] = 1:1$ ). (c) For **V1** + **1** + **4** ( $[\mathbf{F8K}]:[\mathbf{1}]:[\mathbf{4}] = 1:0.5:0.5$ ). A turbidity decrease was observed when methyl  $\alpha$ -D-mannopyranoside and D-(+)-galactose were added to the solutions of **V1** + **1** + **4** mixed with ConA and PNA, respectively (See Figure S2-5 in supporting information.). The background contribution of the nonspecific binding to **V1** is subtracted.

Density of FT-saccharides displayed on the surface of vesicle **V1** can be easily tuned up to eight molecules of FT-saccharides per **F8K**. By changing the sugar density on the vesicle surface, it was found that there is an optimum sugar density for optimum protein binding (Figure 2-13). As



shown in the red line of a combination of ConA and FT-Man 1-coated vesicle, the turbidity increase maximizes at a **1/F8K** ratio of 0.6 (i.e., approximately proportional to sugar/surface area and ca 0.43 molecule/nm<sup>2</sup>). At a higher ligand density, the binding ability vanished. A similar trend was also observed for the PNA binding to FT-Gal 4-coated vesicle with the binding maximizing at  $[4]/[F8K] = 1.4$  (i.e., approximately proportional to sugar/surface area and ca 1.0 molecule/nm<sup>2</sup>, Figure 2-13, blue). Assuming closest hexagonal packing of the ligand molecules on the surface of **V1**, the optimum ratio of **1** on **V1** for ConA binding is a distance of 3.3 nm among each molecule and that is **4** on **V1** is a distance 2.1 nm. These values are close to the known values for spatial separation of the ConA and PNA binding sites, 3.6–3.9 nm<sup>18</sup> and 2.4–3.0 nm<sup>19</sup>, respectively. Appropriate spacing between the ligand moiety on the vesicle is necessary for proteins to bind to the saccharide moiety of ligand molecules on the vesicle surface.

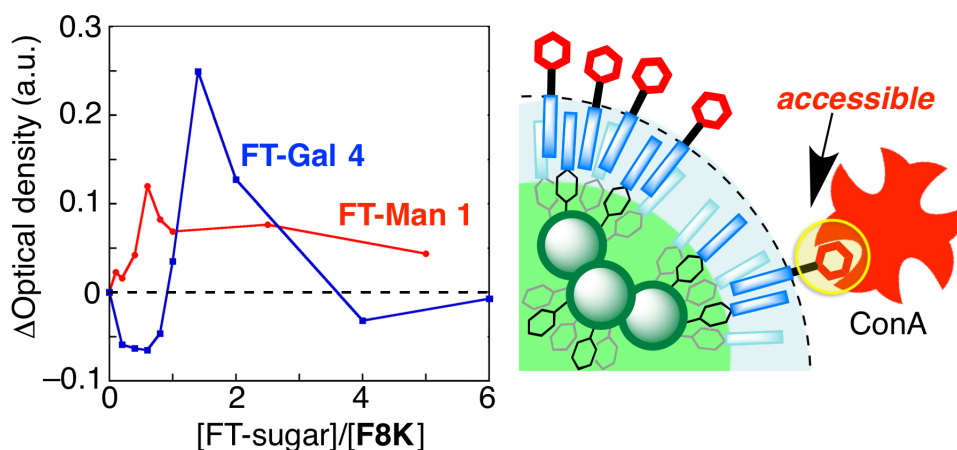


**Figure 2-13.** Dependence of turbidity on sugar density on the vesicle surface measured for combinations of ConA and **V1**-coated FT-Man 1 (red) and PNA and **V1**-coated with FT-Gal 4 (blue). The vertical axis refers to the optical density of the solution after subtraction of the contribution of nonspecific binding to **V1**.

## 2.5. SEM and STEM Imaging of Lectin-Coated Fullerene Vesicles

High resolution SEM provided visual evidence that **V1** maintained its spherical structure after addition of FT-Man 1 and ConA. FT-Man 1-coated vesicle **V2** and protein-binding vesicle **V3** were spin-coated on an IZO (indium-zinc oxide)/glass substrate. After addition of ConA into **V2** solution, **V3** forms and gradually agglomerates into micrometer-sized network structures. To visualize isolated **V3**, **V3** was sampled at 1 min after addition of ConA when the turbidity of the solution have not reached plateau (cf. Figure 2-9b). Surface of IZO is very smooth and hydrophilic that supports the visualization of nanometer-sized vesicles clearly and the isolation of the vesicle on the surface (Figure S2-2). The SEM analysis was carried out using electron beam current of 6.3 pA at low beam landing voltage (200 V) to avoid signal generation from deep inside of the vesicles. Surface of **V2** is very smooth (Figure 2-14a), whereas that of **V3** is rough (Figure 2-14b). ca. 10

## Chapter 2

nm-sized objects are observed on the surface of **V3** (indicated with red circles in Figure 2-14c) that is corresponding to ConA (8 nm).<sup>20</sup> But the spherical structure of the vesicle is still maintained. SEM image of **V3** sampled 20 min after addition of ConA shows network structures, but even after agglomeration, the spherical structure of vesicles is also maintained. In addition, STEM image shows that vesicles with dark black contrast were agglomerated via ConA with gray contrast without loss of the contents of the inside (Figure 2-14e). These results indicate that the ligand display, the protein binding, and the agglomeration did not break the vesicular structure of **V1**. Modification of vesicular vectors with ligand molecules bearing a hydrophobic insertion chain and large amount of proteins usually greatly reduces the mechanical stability of the vesicles.<sup>3,21</sup> In this case, however, mutually orthogonal molecular interactions,  $\pi$ - $\pi$  interaction and fluororous interaction, were applied for driving forces of vesicle formation and ligand binding, respectively. Therefore **V2** and **V3** kept their spherical structure after the modification.

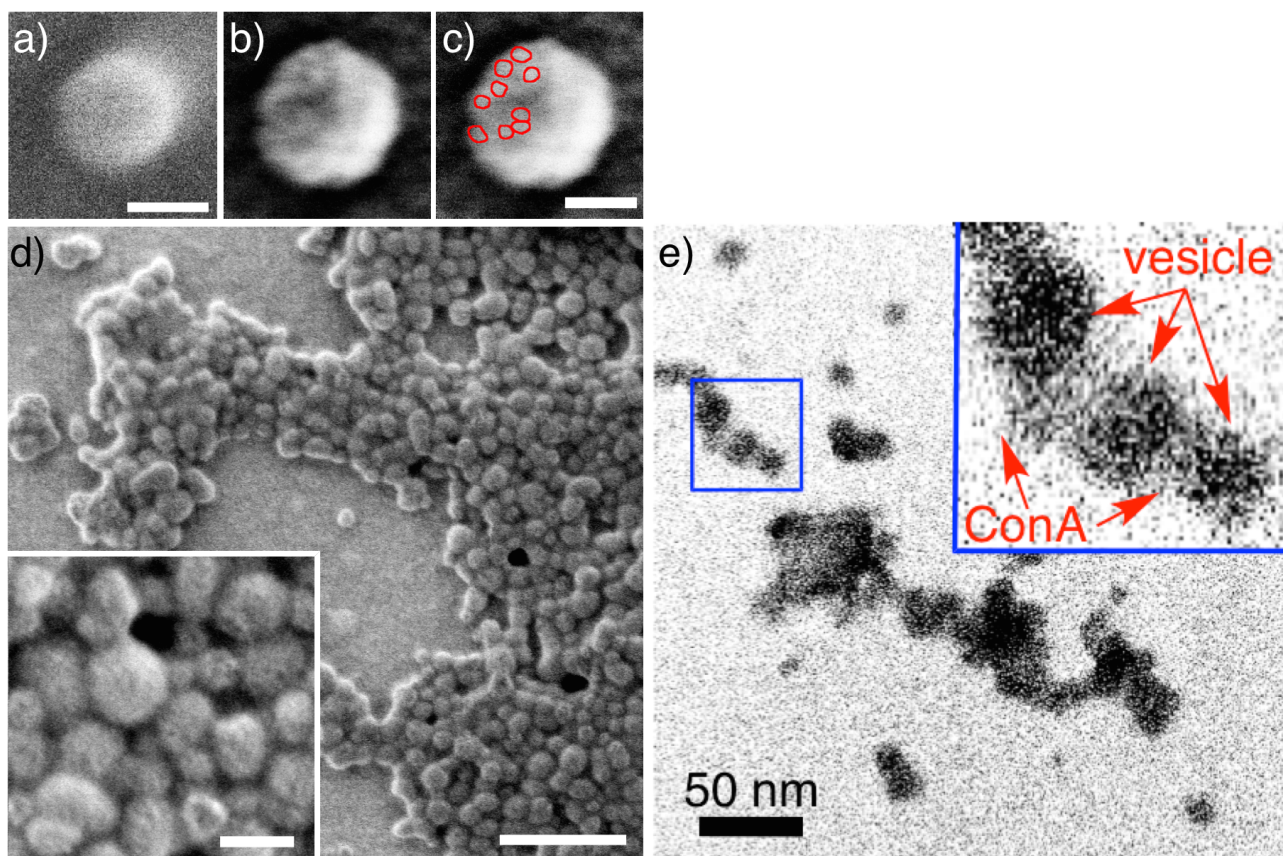


**Figure 2-14.** SEM and STEM images of vesicle **V3** (**V2** bearing ConA). SEM images of **V2** (**V1** bearing FT-Man **1**), **V3**, and the network of **V3** were recorded on an IZO/glass substrate at a landing voltage of 200 V. The imaging under these conditions does not require the conventional metal coating of the sample. (a) **V2**, which is a perfect sphere and has a smooth surface (a mole ratio of **F8K:1** = 1:1). Scale bar is 25 nm. (b) **V3** sampled 1 min after mixing with ConA. (c) The same image as in b, where brighter areas because of ConA molecules are highlighted in red. Scale bar is 50 nm. (d) Agglomerated **V3** sampled 20 min after mixing with ConA. Scale bar is 200 nm. (Inset) A magnified image where ConA molecules are seen to glue **V3** to each other. Scale bar is 50 nm. (e) STEM image of the network of **V3** recorded on an amorphous carbon film (ca. 6 nm thickness) at an acceleration voltage of 200 kV. Vesicles and ConA are denoted by red arrows.

## 2.6. Conclusion

In conclusion, a fluorinated fullerene **F8K** vesicle and ligand display via fluorinated interaction provide a viable approach to the preparation of structurally well-defined nanocapsules. Protein ligands are effectively displayed on the surface of the vesicle for the following protein binding. Spherical structure of the vesicle was maintained after the ligand display and the protein binding. The simplicity of the preparation, the structural robustness, and the utility of diversity of fluorinated-tagged molecules are attractive for construction of a drug carrier in pharmacotherapy compared with conventional lipid systems. In addition, the fluorine-rich and fullerene-based functional vesicles are unique among water-soluble mesoscopic nanostructures and are expected to be applicable as bioimaging agents for  $^{19}\text{F}$  MRI<sup>22</sup> and antioxidants.<sup>7</sup>

## 2.7. References

- <sup>1</sup> (a) Blume, G.; Vevc, G. *Biochim. Biophys. Acta Biomembranes* **1990**, *1029*, 91–97. (b) Soppimath, K. S.; Aminabhavi, T. M.; Kulkarni, A. R.; Rudzinski, W. E. *J. Controlled Release* **2001**, *70*, 1–20. (c) Narang, A. S.; Delmarre, D.; Gao, D. *Int. J. Pharm.* **2007**, *345*, 9–25. (d) Antonietti, M.; Fuöster, S. *Adv. Mater.* **2003**, *15*, 1323–1333.
- <sup>2</sup> (a) Drummond, D. C.; Meyer, O.; Hong, K.; Kirpotin, D. B.; Papahadjopoulos, D. *Pharm. Rev.* **1999**, *51*, 691–744. (b) Lian, T.; Ho, R. J. Y. *J. Pharm. Sci.* **2001**, *90*, 667–680.
- <sup>3</sup> Rosoff, M., Ed. *Vesicles*; Marcel Dekker: New York, 1996.
- <sup>4</sup> (a) Zhou, S.; Burger, C.; Chu, B.; Sawamura, M.; Nagahama, N.; Toganoh, M.; Hackler, U. E.; Isobe, H.; Nakamura, E. *Science* **2001**, *291*, 1944–1947. (b) Homma, T.; Harano, K.; Isobe, H.; Nakamura, E. *J. Am. Chem. Soc.* **2011**, *133*, 6364–6370.
- <sup>5</sup> Homma, T.; Harano, K.; Isobe, H.; Nakamura, E. *Angew. Chem. Int. Ed.* **2010**, *49*, 1665–1668.
- <sup>6</sup> Harano, K.; Minami, K.; Noiri, E.; Okamoto, K.; Nakamura, E. *Chem. Commun.* **2013**, *49*, 3525–3527.
- <sup>7</sup> R. Maeda, E. Noiri, H. Isobe, T. Homma, T. Tanaka, K. Negishi, K. Doi, T. Fujita, E. Nakamura, *Hypertens. Res.* **2008**, *31*, 141–151.
- <sup>8</sup> Ko, K.-S.; Jaipuri, F. A.; Pohl, N. L. *J. Am. Chem. Soc.* **2005**, *127*, 13162–13163.
- <sup>9</sup> Tojino, M.; Mori, M.; Kasuya, M. C. Z.; Hatanaka, K. Kawaguchi, A.; Nagata, K.; Shirai, T.; Mizuno, M. *Bioorg. Med. Chem. Lett.* **2012**, *22*, 1251–1254.
- <sup>10</sup> (a) Gladysz, J. A.; Curran, D. P.; Horváth, I. T. *Handbook of Fluorous Chemistry*, Wiley-VCH, Weinheim, 2004. (b) Horváth, I. T.; Rábai, J. *Science* **1994**, *266*, 72–75. (c) Studer, A.; Hadida, S.; Ferritto, R.; Kim, S. Y.; Jeger, P.; Wipf, P.; Curran, D. P. *Science* **1997**, *275*, 823–826. (d) Vincent, J.-M. *Chem. Commun.* **2012**, *48*, 11382–11391. (e) Yi, W.-B.; Ma, J.-J.; Jiang, L.-Q.; Cai, C.; Zhang, W. *J. Fluorine Chem.* **2014**, *157*, 84–105.
- <sup>11</sup> Miura, T.; Inazu, T. *Tetrahedron Lett.* **2003**, *44*, 1819–1821.
- <sup>12</sup> (a) Mizuno, S. *Master Thesis* **2011**. (b) Yamada, J. *Master Thesis* **2013**.
- <sup>13</sup> Krasovskiy, A.; Knochel, P. *Angew. Chem. Int. Ed.* **2004**, *43*, 3333–3336.
- <sup>14</sup> Harano, K.; Gorgoll, R. M.; Nakamura, E. *Chem. Commun.* **2013**, *49*, 7629–7631.
- <sup>15</sup> (a) Aoi, K.; Itoh, K.; Okada, M. *Macromolecules* **1995**, *28*, 5391–5393. (b) Kamiya, N.;

## Chapter 2

Tominaga, M.; Sato, S.; Fujita, M. *J. Am. Chem. Soc.* **2007**, *129*, 3816–3817.

<sup>16</sup> Brewer, C. F.; Brown, R. D. *Biochemistry* **1979**, *18*, 2555–2562.

<sup>17</sup> Neurohr, K. J.; Young, N. M.; Smith, I. C. P.; Mantsch, H. H. *Biochemistry* **1981**, *20*, 3499–3504.

<sup>18</sup> Thomas, G. B.; Rader, L. H.; Park, J.; Abezgauz, L.; Danino, D.; DeShong, P.; English, D. S. *J. Am. Chem. Soc.* **2009**, *131*, 5471–5477.

<sup>19</sup> Vico, R. V.; Voskuhl, J.; Ravoo, B. J. *Langmuir* **2011**, *27*, 1391–1397.

<sup>20</sup> Becker, J. M.; Reek, Jr. G. N.; Wang, J. L.; Cunningham, B. A.; Edelman, G. M. *J. Biol. Chem.* **1975**, *250*, 1513–1524.

<sup>21</sup> Dieluweit, S.; Csiszár, A.; Rubner, W.; Fleischhauer, J.; Houben, S.; Merkel, R. *Langmuir* **2010**, *26*, 11041–11049.

<sup>22</sup> H. Matsushita, S. Mizukami, F. Sugihara, Y. Nakanishi, Y. Yoshioka, K. Kikuchi, *Angew. Chem. Int. Ed.* **2014**, *53*, 1008–1011.

**— Chapter 2 —  
Experimental Section  
&  
Supporting Information**

## *Chapter 2*

### Table of Contents

#### 1. General

#### 2. Materials

#### 3. Measurements

#### 4. References

#### 1. General

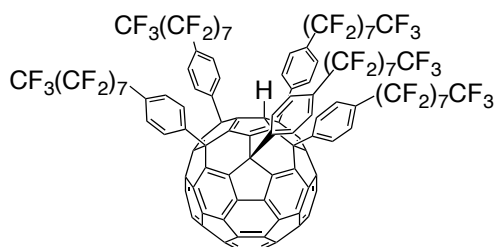
All reactions dealing with air- or moisture-sensitive compounds were carried out in a dry reaction vessel under nitrogen or argon atmosphere. The water content of the solvent was confirmed with a Karl-Fisher Moisture Titrator (MKC-210, Kyoto Electronics Company) to be less than 100 ppm. Analytical thin-layer chromatography was performed on a glass plate coated with 0.25 mm 230–400 mesh silica gel containing a fluorescent indicator (Merck). Analysis with high performance liquid chromatography (HPLC) was performed on JASCO HPLC system equipped with a Bucky Prep column (Nacalai Tesque Cosmosil Buckyprep, 4.6 × 250 mm; column temperature at 40 °C). Flash silica gel chromatography was performed on silica gel 60N (Kanto, spherical and neutral, 140–325 mesh) as described by Still.<sup>1</sup> Gel permeation chromatography (GPC) was performed on Japan Analytical Industry LC-908 (eluent: chloroform) with JAIGEL 1H and 2H polystyrene columns. Infrared (IR) were recorded on a ASI Applied System React IR1000 equipped with an attenuated total reflection (ATR) instrument or JASCO/ FT IR-420 and are reported as wavenumbers ( $\nu$ ) in  $\text{cm}^{-1}$ . NMR spectra were measured on JEOL ECX-400 and ECA-500 spectrometers and reported in parts per million from tetramethylsilane (TMS). <sup>1</sup>H NMR spectra in CDCl<sub>3</sub> were referenced internally to TMS as a standard and CS<sub>2</sub> was used as a co-solvent for dissolution of fullerene pentaadducts, <sup>13</sup>C NMR spectra to the solvent resonance. Hexafluorobenzene ( $\delta = -162.0$ ) was used as an internal standard for <sup>19</sup>F NMR.<sup>2</sup> Dynamic light scattering (DLS) study was carried out on a Malvern Zetasizer Nano ZS machine. Scanning transmission electron microscopy (STEM) was performed on a JEOL JEM-2100F (acceleration voltage: 200 kV). Atomic force microscope (AFM) measurement was performed by using JEOL JSPM-4200 with a silicon cantilever (NSC-35, resonant frequency 120–190 kHz). The time-dependent turbidity changes were recorded on a JASCO V-570 UV/Vis/NIR Spectrophotometer.

## Chapter 2

### 2. Materials

Unless otherwise noted, materials were purchased from Tokyo Kasei Co., Aldrich Inc., and other commercial suppliers and used after appropriate purification before use. Anhydrous ethereal solvents (stabilizer-free) were purchased from WAKO Pure Chemical and purified by a solvent purification system (GlassContour)<sup>3</sup> equipped with columns of activated alumina and supported copper catalyst (Q-5) prior to use. All other solvents were purified by distillation and stored over molecular sieves 4 Å. Distilled water was further purified with Millipore Milli-Q. **F8K** vesicle (**V1**)<sup>4</sup> and **C8K** vesicle (**V1C**)<sup>5</sup> were prepared according to the reported procedures.

### 6,9,12,15,18-Penta(4-heptadecafluorooctylphenyl)-1,6,9,12,15,18-hexahydro(C<sub>60</sub>-I<sub>n</sub>) [5,6]fullerene (**F8H**)

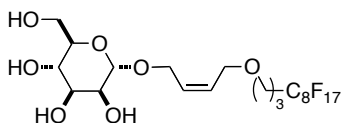


The synthesis of **F8H** was firstly reported by Nakamura et al. in 2010.<sup>4</sup> Herein a modified procedure for facile synthesis of **F8H** is described. 4-(heptadecafluorooctyl)-1-iodobenzene (435 mg, 0.700 mmol) in THF (0.35 mL) was added to Turbo Grignard reagent; a solution of <sup>i</sup>PrMgCl•LiCl in THF (1.08 M, 1.04 mL, 1.12 mmol) over 10 min at -20 °C. After stirring for 1 h at -20 °C, the solution was transferred through a cannula to a suspension of CuBr•SMe<sub>2</sub> (230 mg, 1.12 mmol) in THF (0.60 mL) at -20 °C, and then the mixture was stirred for 10 min at -20 °C. A solution of C<sub>60</sub> (25.0 mg, 35.0 μmol) in 1,2-dichlorobenzene (1.27 mL) was transferred through a cannula to the mixture at -20 °C. After stirring for 1 h at 35 °C, saturated aqueous ammonium chloride solution (1 mL) was added to the solution. The suspension was concentrated to remove THF and dimethyl sulfide. The concentrated mixture was filtered through a pad of silica gel (3 cm) with toluene and FC-72. The filtrate was concentrated on a rotary evaporator at 70 °C until precipitation occurred. Methanol was added until precipitation was complete. The precipitate was collected by membrane filter, washed with methanol, and dried under reduced pressure for 4 h to obtain an orange-red powder (80.2 mg) in 70 % yield. Analytical data is consistent with the reported ones.<sup>4</sup>



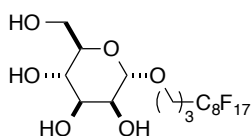
## Chapter 2

### 1-*O*-(4,4,5,5,6,6,7,7,8,8,9,9,10,10,11,11,11-heptafluoroundecanoxyl-*cis*-but-2-enyl)- $\alpha$ -mannopyranoside (FT-Man 1)



1-*O*-(4,4,5,5,6,6,7,7,8,8,9,9,10,10,11,11,11-heptafluoroundecanoxyl-*cis*-but-2-enyl)-2,3,4,6-tetra-*O*-acetyl- $\alpha$ -mannopyranoside (56.5 mg, 64.3  $\mu$ mol)<sup>6</sup> and  $K_2CO_3$  (31.5 mg, 228  $\mu$ mol) was dissolved in MeOH (3 ml). The mixture was stirred for 30 min. The reaction mixture was neutralized using Amberlyst-15 ion-exchange resin and filtered. The solvent was removed under reduced pressure and desired product was obtained as a colorless sticky solid (39.6 mg, 55.7  $\mu$ mol, 87%): mp 180–181 °C (dec); IR (powder) 3383, 2925, 2503, 1722, 1452, 1370, 1331, 1201, 1146, 1134, 1104, 1059, 1031, 974, 877, 809, 779, 737, 721, 703, 655, 557  $cm^{-1}$ ;  $^1H$  NMR (500 MHz, methanol- $d_4$ )  $\delta$  1.86–1.91 (m, 2H), 2.24–2.35 (m, 2H), 3.54–3.57 (m, 3H), 3.62 (dd,  $J = 9.7, 9.7$  Hz, 1H), 3.69–3.71 (m, 2H), 3.81 (dd,  $J = 1.7, 3.4$  Hz, 1H), 3.86 (dd,  $J = 2.3, 12.0$  Hz, 1H), 4.11–4.31 (m, 4H), 4.81 (d,  $J = 1.7$  Hz, 1H), 5.72–5.77 (m, 2H);  $^{13}C$  NMR (125 MHz, methanol- $d_4$ )  $\delta$  21.91, 28.88 (t,  $J_{CF} = 23$  Hz), 62.95, 63.59, 67.49, 68.64, 69.68, 72.20, 72.63, 74.84, 100.76, 129.52, 131.03;  $^{19}F$  NMR (470 MHz, methanol- $d_4$ )  $\delta$  -124.87 (2F), -122.03 (2F), -121.31 (2F), -120.50 (4F), -120.31 (2F), -113.05 (2F), -79.97 (3F); Anal. Calcd for  $C_{21}H_{23}F_{17}O_7$ : C, 35.51; H, 3.26. Found: C, 35.22; H, 3.52.

### 1-*O*-(4,4,5,5,6,6,7,7,8,8,9,9,10,10,11,11,11-heptafluoroundecanoxyl)- $\alpha$ -mannopyranoside (FT-Man 2)

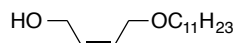


To a solution of 2,3,4,6-tetra-*O*-acetyl- $\alpha/\beta$ -D-mannopyranosidetrichloroacetimidate<sup>7</sup> (211 mg, 0.428 mmol) and 1H,1H,2H,2H,3H,3H-perfluoroundecanol (138 mg, 289  $\mu$ mol) in dichloromethane (5 mL) were cooled down to 0 °C. TMSOTf (41.8 mg, 188  $\mu$ mol) was added and the reaction mixture was stirred at 0 °C for 30 min. The reaction was quenched with triethylamine (1 mL). The crude product was purified by solid-phase extraction using a fluorosolid-phase extraction cartridge (Fluorous Technologies, Inc.). Non-fluorous compounds were eluted with 80% MeOH/water and fluorosolid compounds were eluted by 100% MeOH. The solvent was removed under reduced pressure. Whole amount of the fluorosolid compounds (193 mg) and  $K_2CO_3$  (149 mg, 1.08 mmol) were dissolved in MeOH (7.5 mL). The mixture was stirred at rt for 2 h. The reaction

## Chapter 2

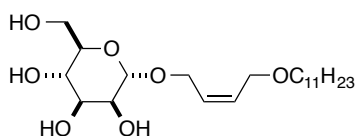
mixture was neutralized using Amberlyst-15 ion-exchange resin and filtered. The solvent was removed under reduced pressure and desired product was purified by flash column chromatography on silica gel using Hexane/EtOAc and EtOAc/MeOH as eluent. The desired product was obtained as a colorless sticky solid (50.0 mg, 78.0  $\mu\text{mol}$ , 29%): mp 205–206 °C; IR (powder) 3317, 2927, 2855, 2360, 2340, 1739, 1435, 1366, 1262, 1146, 1102, 1026, 977, 809, 705, 657, 557  $\text{cm}^{-1}$ ;  $^1\text{H}$  NMR (500 MHz, methanol- $d_4$ )  $\delta$  1.85–1.95 (m, 2H), 2.23 (tt,  $J = 19, 9.0$  Hz, 2H), 3.48–3.54 (m, 2H), 3.60 (t,  $J = 9.5$  Hz, 1H), 3.67–3.72 (m, 2H), 3.80–3.86 (m, 3H), 4.77 (d,  $J = 1.2$  Hz, 1H);  $^{13}\text{C}$  NMR (125 MHz, methanol- $d_4$ )  $\delta$  21.77, 28.91 (t,  $J_{\text{CF}} = 22$  Hz), 62.94, 66.99, 68.55, 72.13, 72.64, 74.89, 101.65;  $^{19}\text{F}$  NMR (470 MHz, methanol- $d_4$ )  $\delta$  -124.77 (2F), -121.90 (2F), -121.22 (2F), -120.41 (4F), -120.22 (2F), -112.83 (2F), -79.85 (3F); HRMS (FAB+): Calculated for  $[\text{C}_{17}\text{H}_{17}\text{F}_{17}\text{O}_6\text{Na}]^+$ : 663.0651, found: 663.0637.

### 4-undecanoxyl-*cis*-2-buten-1-ol



*cis*-1,4-butanediol (0.330 mg, 3.50 mmol) and crushed KOH (304 mg, 5.42 mmol) were added to distilled DMF (15 mL). Undecyl iodide (800 mg, 2.83 mmol) was added to the solution at rt and then the reaction mixture was heated at 65 °C for 2 h. The reaction was quenched with HCl (1N) after dilution with water (30 mL). The organic layer was extracted with EtOAc (30 mL x 3) and dried over brine (10 mL) and  $\text{MgSO}_4$ . The mixture was filtered and the solvent was removed under reduced pressure. The crude product was purified by flash column chromatography on silica gel using Hexane/EtOAc as eluent. The desired product was obtained as a yellow oil (549 mg, 2.27 mmol, 81%): IR 3368, 2923, 2853, 2360, 2340, 1722, 1466, 1380, 1106, 1029, 721  $\text{cm}^{-1}$ ;  $^1\text{H}$  NMR (500 MHz,  $\text{CDCl}_3$ )  $\delta$  0.88 (t,  $J = 7.2$  Hz, 3H), 1.26–1.30 (m, 16H), 1.56–1.61 (m, 2H), 1.96 (t,  $J = 5.7$  Hz, OH), 3.44 (t,  $J = 6.6$  Hz, 2H), 4.05 (d,  $J = 6.3$  Hz, 2H), 4.21 (dd,  $J = 5.7, 5.7$  Hz, 2H), 5.72 (dt,  $J = 11, 5.7$  Hz, 1H), 5.83 (dt,  $J = 11, 6.3$  Hz, 1H);  $^{13}\text{C}$  NMR (125 MHz,  $\text{CDCl}_3$ )  $\delta$  14.10, 22.67, 26.14, 29.32, 29.46, 29.56, 29.59 (2C), 29.70, 31.89, 58.83, 66.47, 70.91, 128.65, 132.02; HRMS (ESI+): Calculated for  $[\text{C}_{15}\text{H}_{30}\text{O}_2\text{Na}]^+$ : 265.2138, found: 265.2136.

### 1-*O*-(undecanoxyl-*cis*-but-2-enyl)- $\alpha$ -mannopyranoside (AT-Man 3)

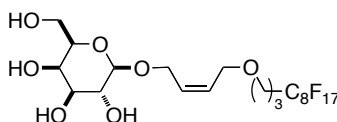


To a solution of 2,3,4,6-tetra-*O*-acetyl- $\alpha/\beta$ -D-mannopyranosidetrichloroacetimidate (296 mg,

## Chapter 2

603  $\mu\text{mol}$ )<sup>7</sup> and 4-undecanoxyl-*cis*-2-buten-1-ol (121 mg, 500  $\mu\text{mol}$ ) in dichloromethane (10 mL) were cooled down to 0 °C. TMSOTf (77.8 mg, 350  $\mu\text{mol}$ ) was added and the reaction mixture was stirred at 0 °C for 1.5 h. The reaction was quenched with triethylamine (0.1 mL) after dilution with water (20 mL). The organic layer was extracted with dichloromethane (10 mL x 3) and dried over brine (10 mL) and MgSO<sub>4</sub>. The mixture was filtered and the solvent was removed under reduced pressure. The crude product (400 mg) and K<sub>2</sub>CO<sub>3</sub> (277 mg, 2.00 mmol) were dissolved in MeOH (15 mL). The mixture was stirred at rt for 1 h. The reaction mixture was neutralized using Amberlyst-15 ion-exchange resin and filtered. The solvent was removed under reduced pressure and desired product was purified by flash column chromatography on silica gel using Hexane/EtOAc and EtOAc/MeOH as eluent. The desired product was obtained as an yellow waxy oil (67.0 mg, 166  $\mu\text{mol}$ , 33%): IR (powder) 3331, 2924, 2854, 2360, 2341, 1650, 1459, 1353, 1230, 1071, 975, 835, 736, 678 cm<sup>-1</sup>; <sup>1</sup>H NMR (500 MHz, methanol-*d*<sub>4</sub>)  $\delta$  0.89 (t, *J* = 6.9 Hz, 3H), 1.29–1.32 (m, 16H), 1.56 (tt, *J* = 7.2, 7.1 Hz, 2H), 3.44 (t, *J* = 6.6 Hz, 2H) 3.53–3.56 (m, 1H) 3.65 (td, *J* = 9.7, 1.7 Hz, 1H), 3.71–3.75 (m, 2H), 3.82–3.85 (m, 2H), 4.08 (d, *J* = 4.6 Hz, 2H), 4.11–4.15 (m, 1H), 4.25–4.28 (m, 1H) 4.81 (s, 1H) 5.70–5.73 (m, 2H); <sup>13</sup>C NMR (125 MHz, methanol-*d*<sub>4</sub>)  $\delta$  14.43, 23.72, 27.25, 30.46, 30.58, 30.72 (3C), 30.77, 33.06, 62.90, 63.69, 67.37, 68.60, 71.59, 72.20, 72.60, 74.74, 100.75, 129.39, 131.13; HRMS (ESI<sup>+</sup>): Calculated for [C<sub>21</sub>H<sub>40</sub>O<sub>7</sub>Na]<sup>+</sup>: 427.2666, found: 427.2677.

### 1-*O*-(4,4,5,5,6,6,7,7,8,8,9,9,10,10,11,11,11-heptafluoroundecanoxyl-*cis*-but-2-enyl)-2,3,4,6- $\beta$ -galactopyranoside (FT-Gal 4)



1-*O*-(4,4,5,5,6,6,7,7,8,8,9,9,10,10,11,11,11-heptafluoroundecanoxyl-*cis*-but-2-enyl)-2,3,4,6-tetra-*O*-acetyl- $\alpha$ -galactopyranoside (10.1 mg, 11.5  $\mu\text{mol}$ )<sup>7</sup> and K<sub>2</sub>CO<sub>3</sub> (7.5 mg, 54  $\mu\text{mol}$ ) was dissolved in MeOH (1 ml). The mixture was stirred for 2 h. The reaction mixture was neutralized using Amberlyst-15 ion-exchange resin and filtered. The solvent was removed under reduced pressure and desired product was obtained as a colorless sticky solid (7.5 mg, 11  $\mu\text{mol}$ , 88%): mp 81.5–82.5 °C; IR (powder) 3502, 3337, 2933, 2870, 1731, 1452, 1372, 1332, 1200, 1146, 1114, 1077, 1058, 1041, 974, 920, 861, 780, 738, 721, 704, 655, 622, 558 cm<sup>-1</sup>; <sup>1</sup>H NMR (500 MHz, methanol-*d*<sub>4</sub>)  $\delta$  1.86–1.92 (m, 2H), 2.24–2.35 (m, 2H), 3.47–3.57 (m, 5H), 3.74–3.85 (m, 5H), 4.28 (d, *J* = 8.1 Hz, 1H), 4.33 (dd, *J* = 6.9, 12.6 Hz, 1H), 4.45 (dd, *J* = 5.75, 13.2 Hz, 1H), 5.72–5.83 (m, 2H); <sup>13</sup>C NMR (125 MHz, methanol-*d*<sub>4</sub>)  $\delta$  21.87, 28.87 (t, *J*<sub>CF</sub> = 23 Hz), 62.55, 65.48, 67.50, 69.66,

## Chapter 2

70.33, 72.47, 75.02, 76.78, 103.86, 129.52, 131.03;  $^{19}\text{F}$  NMR (470 MHz, methanol- $d_4$ )  $\delta$  -124.87 (2F), -122.03 (2F), -121.31 (2F), -120.50 (4F), -120.31 (2F), -113.05 (2F), -79.97 (3F); Anal. Calcd for  $\text{C}_{21}\text{H}_{23}\text{F}_{17}\text{O}_7$ : C, 35.26; H, 3.26. Found: C, 35.40; H, 3.43.

### Preparation of fullerene vesicles

The vesicle solution of **F8K** (**V1** solution) used for the studies was prepared as reported<sup>4</sup>: Potassium *tert*-butoxide in THF (1.0 M, 35.2 mL, 35.2  $\mu\text{mol}$ ) was added to a suspension of **F8H** (23.4  $\mu\text{mol}$ ) in THF (1.84 mL) and the mixture was stirred under nitrogen. During the mixing, the suspension became a dark transparent solution of **F8K**. After 3 h, a portion of the solution of **F8K** (12.5 mM, 1.60 mL, 20  $\mu\text{mol}$ ) was slowly injected into water (8.4 mL) with stirring at 400 rpm over 1 min using a syringe pump (ISIS Co.) to obtain a vesicle solution of **F8K** (2.0 mM) in 16 % THF/water. THF was removed by evaporation, and then the vesicle solution was diluted with water using 25 mL measuring flask. The final concentration of vesicle **V1** was determined to be 1.0 mM by UV-Vis absorption measurement. The average diameter of the vesicle **V1** was determined to be  $27.0 \pm 0.5$  nm (PDI: 0.15) by DLS measurement. The vesicle solution of **C8K** (**V1C** solution) was prepared by the same procedure and the concentration was adjusted to 1.0 mM. The average diameter of the vesicle **V1C** was determined to be  $23.8 \pm 0.1$  nm (PDI: 0.15).

### Typical procedure of preparation of V2

A stock solution of FT-Man **1** (0.50 mM, 0.12 mL) was mixed with **F8K** (0.33 mM) vesicle (**V1**) solution (0.18 mL) and the mixture was stirred using a magnetic stirrer over 10 min at 200 rpm ( $[\mathbf{1}] = [\mathbf{F8K}] = 0.20$  mM). Increase in diameter of the vesicle and disappearance of signal originating in **1** were observed by DLS analysis, suggesting adsorption of **1** on **V1** (i.e. formation of **V2**).

## 3. Measurements

### DLS measurements

DLS measurement was performed by using Malvern Zetasizer Nano ZS equipped with an He-Ne laser operating 4 mW power and 633 nm wavelength, and a computer-controlled correlator, at a 173° accumulation angle. Measurements were carried out in polystyrene or glass cuvette. The data were processed using Dispersion Technology Software version 5.10 to give Z-average particle size and polydispersity index (PDI) value by cumulant analysis, and particle size distribution with high resolution (Multiple narrow mode).

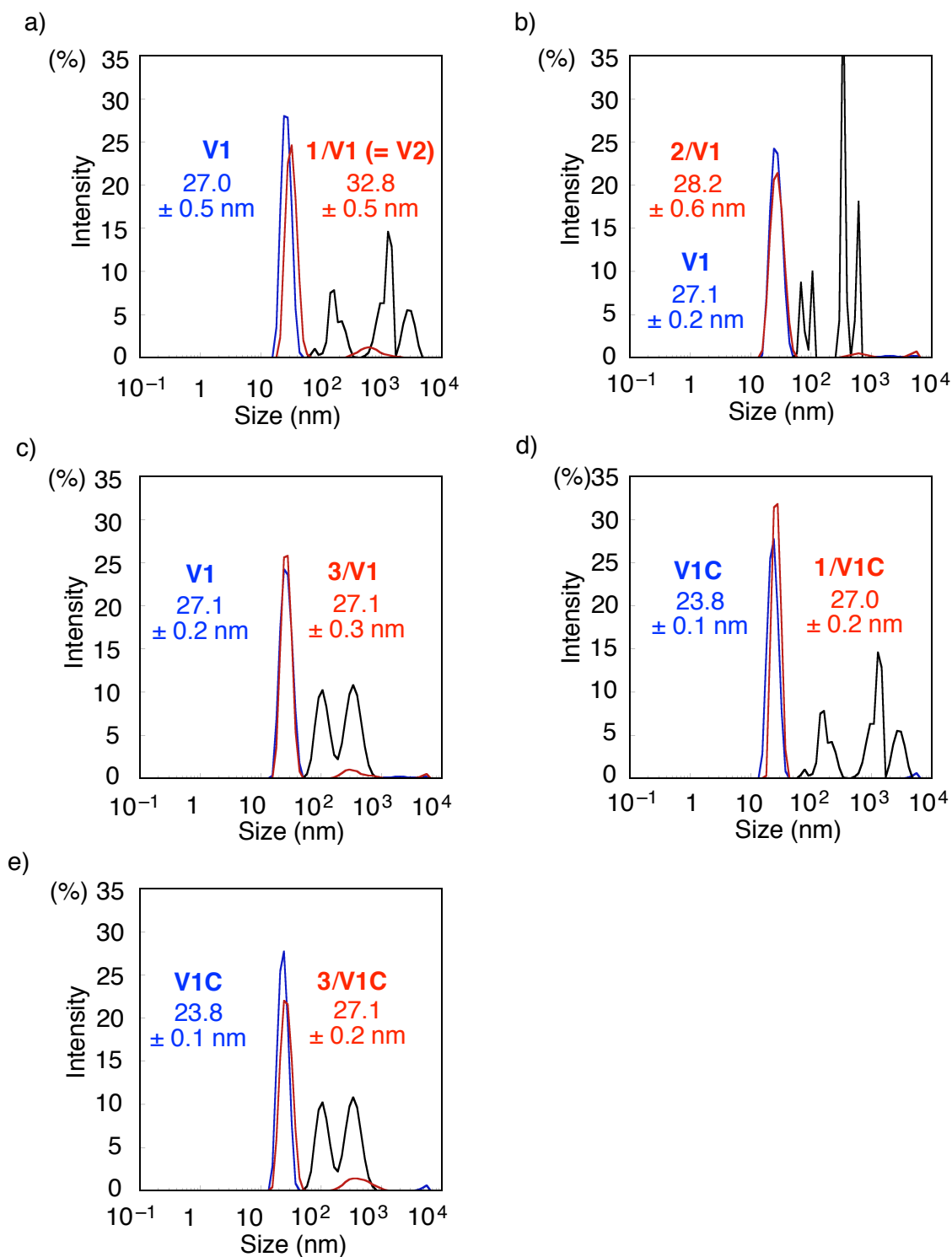


**Figure S2-1.** DLS analysis of fullerene vesicles, V1 and V1C, coated with 1, 2, and 3 ([sugar]/[fullerene] = 1:1). (a) V1 + 1, (b) V1 + 2, (c) V1 + 3, (d) V1C + 1, (e) V1C + 3. Error means standard error (N = 3). Aggregates of 1, 2, and 3 are shown as black line.

**SEM measurement**

Extreme high resolution scanning electron microscopy (SEM) was carried out using a FEI Magellan 400L. An aqueous solution of the **V1**, **V2**, and **V3** ( $[\text{V1}] = 0.02\text{--}2\text{ mM}$ ) was spin-coated on an IZO/glass substrate cleaned by UV/ozone pretreatment. After drying under reduced pressure ( $5 \times 10^{-2}\text{ Pa}$ ) for 10 min, the substrates were subjected to the SEM observation at a beam landing voltage of 200 V with a beam deceleration bias of 800 V under a vacuum of  $5 \times 10^{-5}\text{ Pa}$  without any conductive coatings.

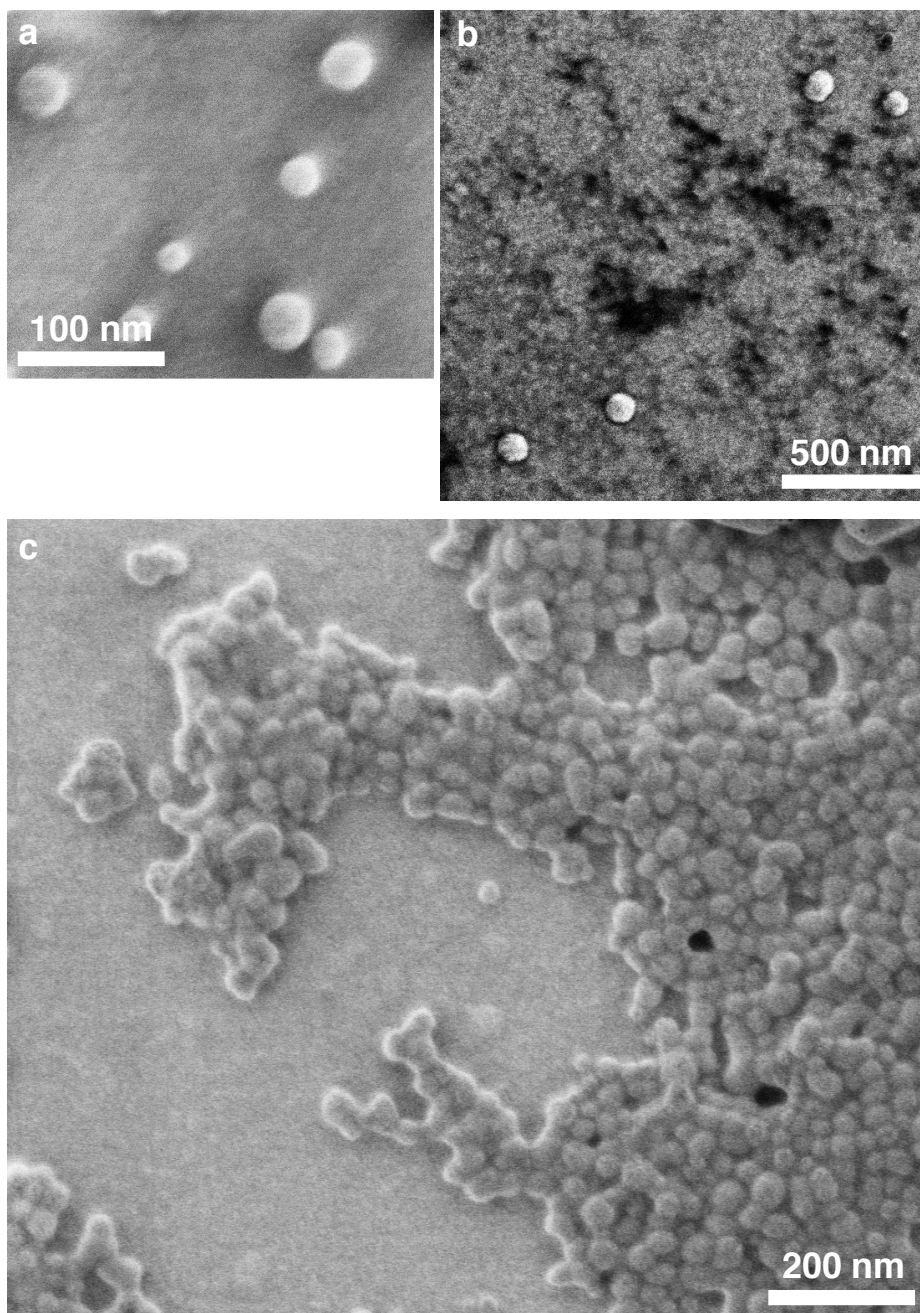


**Figure S2-2.** SEM images of fullerene vesicles on an IZO/glass taken at beam landing voltage of 200 V and beam current of 6.3 pA. (a) **V2**, (b) **V3**, (c) agglomerated **V3**. The vesicles are the round objects surrounded by shadow and the irregular objects in b are the crystalline fine structures of IZO or excess ConA.

## Chapter 2

### AFM measurement

AFM measurement was conducted on a JEOL JSPM-4200 with a silicon cantilever (NSC-350, resonant frequency 120–190 kHz). Samples were deposited on mica substrate (5 x 5 mm<sup>2</sup>) in aliquot of 2 mL under air. After drying the sample by blowing air for 10 sec and under reduced pressure (5 x 10<sup>-2</sup> Pa), the AFM images were obtained with AC mode measurement.

### STEM measurement

A solution (2 µl) of **F8K** vesicle (50 µM) or the mixture of **F8K**, FT-Man **1**, and ConA ([**F8K**] = [**1**] = 50 µM, [ConA] = 1.8 µM) in water was dropped on TEM copper grids pre-coated with super-ultra-high-resolution carbon supported films (thickness: ca 6 nm, Oken Shoji Co. Inc.), and the substrate was dried without blotting in a desiccator overnight. The STEM observation at 298 K was performed on a JEOL JEM-2100F with a spherical aberration coefficient Cs = 1.0 mm at an acceleration voltage of 200 kV under reduced pressure of 1.0 × 10<sup>-5</sup> Pa in the sample column. The current density was ca 0.5 pA•cm<sup>-2</sup>. The imaging instrument used was an ultrascan charged-coupled device (CCD) camera (512 × 512 pixels).

### Interfacial tension measurement

Interfacial tension measurements were performed using a DM-301 (Kyowa Interface Science Co. Ltd.) and analyzed by FAMAS software. FT-Man **1** was weighted in a plastic tube and dissolved in **F8K** (1.0 mM) vesicle (**V1**) solution (200 µL) by stirring using a magnetic stirrer over 10 min at 200 rpm. Interfacial tension at each concentration was measured by the pendant drop method.<sup>8</sup> The droplet of sample solution was hanged down from the tip of syringe and the interfacial tension ( $\gamma$ ) was calculated from the captured image of the droplet using the equation of Bashforth and Adams which is based on Laplace's equation (eq.1).

$$\frac{1}{R_1/a} + \frac{\sin \varphi}{x/a} = -B \frac{z}{a} + 2 \quad (\text{eq. 1})$$

where  $a$  is the radius of curvature at the apex of the drop,  $x$ ,  $z$  and  $f$  are the coordinates defined as in Figure S2-3, and  $B$  is given by eq.2.

$$B = \frac{a^2 g \Delta \rho}{\gamma} \quad (\text{eq. 2})$$

where  $\Delta \rho$  is the difference between the densities of the pendant drop and air,  $g$  is the gravitational constant, Interfacial tension of **1** was measured three times at each concentration of **1**. Error was calculated as standard error of the interfacial tension. The CAC values were obtained from an intersection of two regression curves (Figure S2-4). The maximum density of **1** on the **V2** surface

## Chapter 2

was estimated from increase of critical aggregation concentration (CAC) of **1**. The maximum density of FT-Gal **4** was also obtained in the same way as **1**.

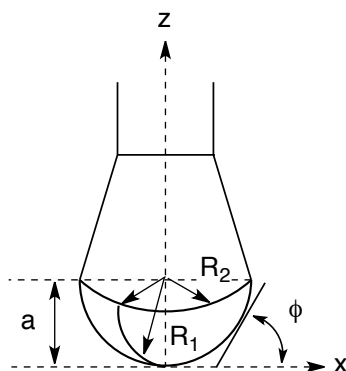


**Figure S2-3.** Pendant drop method to measure interfacial tension.

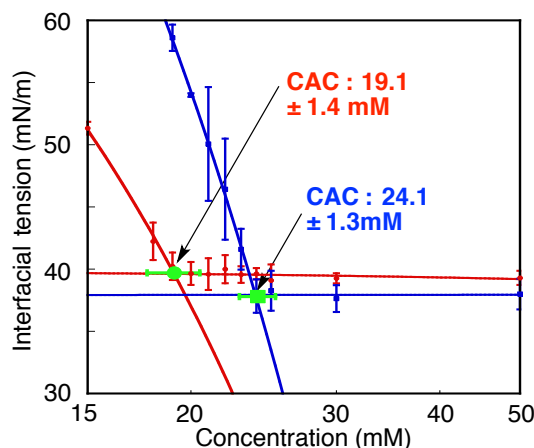


**Figure S2-4.** Interfacial tension measurements of FT-Man **1**. Interfacial tension change in **1** in water (red) and **1** in a solution of vesicle **V1** (1.0 mM for **F8K**, blue). CAC values of **1** increased by 5 mM due to absorption of **1** on **V1**. This result suggests that the maximum loading ratio of **1** on **V1** is 5:1. Error bar means standard error (N =3).

### Molecular modeling of **V2**

Molecular structure of **F8K** was optimized by molecular mechanics calculations using Compass force field implemented in Materials Studio.<sup>9</sup> The surface area per one **F8K** molecule that consists of outer part of the **V1** vesicle was estimated to be 3.80 nm<sup>2</sup> from SLS measurements.<sup>4b</sup> Using hexagonal closest packing lattice of **F8K** with spatial separation of 2.10 nm between the neighboring molecules generated on Materials Studio, eight FT-Man molecules **1** per one **F8K** molecule were placed on **F8K** layer manually not to overlap with **F8K** molecule and other FT-molecules within the sum of van der Waals radii.



Turbidimetry experiments<sup>10</sup>

**Concanavalin A (ConA) and peanut agglutinin (PNA):** Turbidimetry experiments were performed in a quartz cell (1×1 cm). Aliquot (500  $\mu$ L) of stock ConA or PNA solutions (1 mg/ mL) in HEPES buffer (10 mM, pH 7.1, [NaCl] = 150 mM, [CaCl<sub>2</sub>] = 1 mM, [MnCl<sub>2</sub>] = 1 mM) was diluted with the same HEPES buffer (1700 mL). The 1: 1 mixture as a molar ratio of **F8K** or **C8K**, and FT-Man **1** or the 1: 1 mixture as a molar ratio of **F8K** and FT-Gal **4** in Milli-Q (300  $\mu$ L) was added. The mixture was stirred at 1000 rpm at 20 °C and UV spectra were measured every 10 sec. The turbidity of the mixtures was monitored by plotting absorbance at 500 nm. After 20 minutes, an excess amount of inhibitor in HEPES buffer (150  $\mu$ L of 1 M solution of Me- $\alpha$ -D-mannopyranoside for ConA, 150  $\mu$ M of 0.5 M of D-(+)-galactose) was added. The absorbance after addition of the inhibitor was corrected in consideration of the effect of dilution. The same vesicle solution was used for a series of experiment for avoidance of effect of the size distribution.

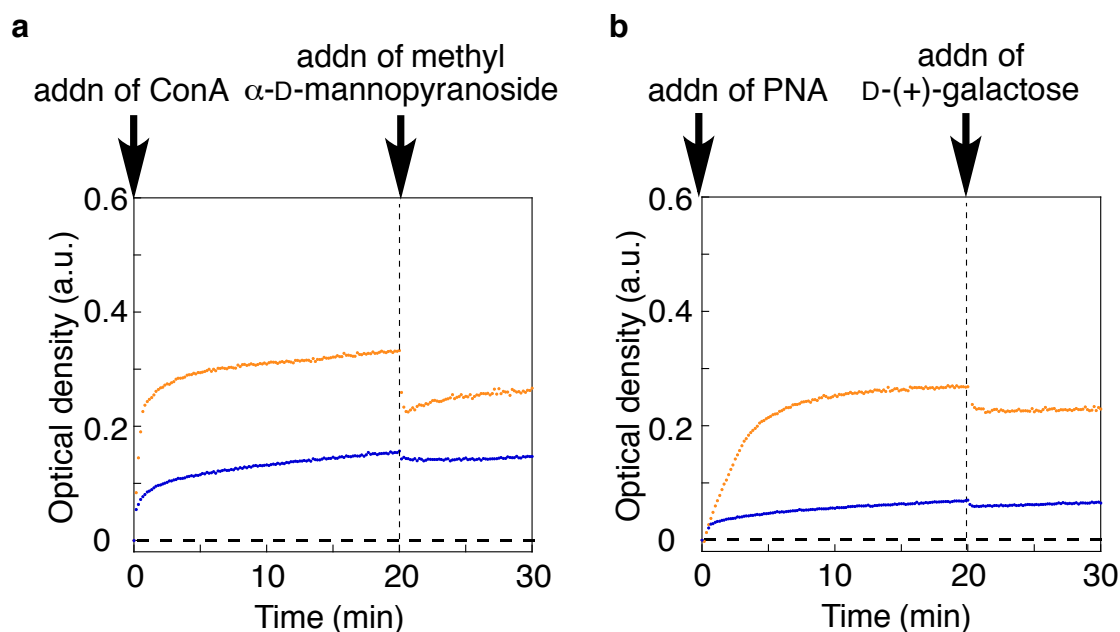


**Figure S2-5.** Time-dependent turbidity change upon mixing proteins with solution of **V1** coated both with FT-Man **1** and FT-Gal **4**. The measurements were carried out using the same condition mentioned above. (a) Turbidity change upon mixing ConA with a solution **V1** coated with **1** and **4** ([**F8K**]:[**1**]:[**4**] = 1:0.5:0.5, red), and ConA with a solution of **V1** (blue). At 20 min, 3000 eq of methyl  $\alpha$ -D-mannopyranoside was added as an inhibitor of binding between **1** and ConA (dashed line). (b) Turbidity change upon mixing PNA to **F8K** vesicle solution incorporating **1** and **4** ([**F8K**]:[**1**]:[**4**] = 1:0.5:0.5, red), and PNA with **V1** (blue). At 20 min, 3000 eq of D-(+)-galactose was added as an inhibitor of specific binding between **4** and PNA (dashed line).

## Chapter 2

### 4. References

- <sup>1</sup> Still, W. C.; Kahn, M.; Mitra, A. *J. Org. Chem.* **1978**, *43*, 2923–2925.
- <sup>2</sup> Webb, G. A. *Annual reports on NMR spectroscopy volume 14*, Academic Press, New York, 1983.
- <sup>3</sup> Pangborn, A. B.; Giardello, M. A.; Grubbs, R. H.; Rosen, R. K.; Timmers, F. J. *Organometallics* **1996**, *15*, 1518–1520.
- <sup>4</sup> Homma, T.; Harano, K.; Isobe, H.; Nakamura, E. *Angew. Chem. Int. Ed.* **2010**, *49*, 1665–1668.
- <sup>5</sup> Homma, T.; Harano, K.; Isobe, H.; Nakamura, E. *J. Am. Chem. Soc.* **2011**, *133*, 6364–6370.
- <sup>6</sup> Ko, K.-S.; Jaipuri, F. A.; Pohl, N. L. *J. Am. Chem. Soc.* **2005**, *127*, 13162–13163.
- <sup>7</sup> Kamiya, N.; Tominaga, M.; Sato, S. Fujita, M. *J. Am. Chem. Soc.* **2007**, *129*, 3816–3817.
- <sup>8</sup> Emerson, Y. A. Nicole, R. D. *Materials Research* **1999**, *2*, 23–32.
- <sup>9</sup> Materials Studio, version 5.0, Accelrys Software Inc., 2009.
- <sup>10</sup> Kamiya, N.; Tominaga, M.; Sato, S. Fujita, M. *J. Am. Chem. Soc.* **2007**, *129*, 3816–3817.

— Chapter 3 —  
**Shape-Selective Surface Modification of a Nanocarbon via  
Host-Guest Interaction of Cyclodextrins**

## *Chapter 3*

### 3.1. Introduction

#### 3.1.1. Properties and Functionalization of Carbon Nanohorns

Carbon nanohorn (CNH) aggregates are 50–150 nm-sized aggregates of cone-shaped carbon nanotubes (CNTs).<sup>1</sup> They are produced by CO<sub>2</sub> laser ablation of carbon at room temperature without any transition metals as a catalyst. Because of the transition metal-free nature and the unique dahlia-shaped morphology that provides large surface area, CNH aggregates are useful for occlusion materials,<sup>2</sup> catalyst supports,<sup>3</sup> and a drug carrier.<sup>4</sup> The spherical tip of CNH is more reactive than the sidewall due to the highly curved and strained  $\pi$  system like fullerenes. Conventionally, there are two methods in the modification of CNH aggregates. One is making hole on the tip by C-C bond cleavage through oxidation, and then catalysts or drug molecules can be incorporated into the interior of the nanohorns.<sup>4b</sup> Another is addition reaction to the outer surface of the tip. For example, tip area can be aminated by treatment with NaNH<sub>2</sub> to yield water-dispersible amino CNHs.<sup>5</sup> In addition, further modification can be carried out through formation of amide bonding.<sup>6</sup> In contrast, noncovalent surface modification of CNH aggregates has been performed in a similar manner to that of CNT, such as adsorption of aromatic molecules by  $\pi$ - $\pi$  interactions and surfactants by hydrophobic interactions.<sup>7</sup> Dispersion of CNH aggregates in water by a surfactant as a dispersant is studied not only for dispersion but also for removal of impurities. Commercially available CNH from NEC Corporation contain 10–20% of hornless micrometer-sized graphitic carbon particles ( $\mu$ mGCPs) that are produced during their production process.<sup>8</sup> Since this impurity has a smaller surface area than CNH aggregates, it decreases the utility of CNH aggregates as a material support. Iijima et al. reported a separation of CNH aggregates and hornless  $\mu$ mGCPs using sodium dodecylbenzenesulfonate (NaDDBS) as a dispersant in D<sub>2</sub>O. However, like conventional noncovalent modification of nanocarbons, dispersion of CNH aggregates by conventional surfactants is inefficient in molecular economy. Large amount of dispersant (e.g. 25 mg of NaDDBS for 1 mg of CNH aggregate) is necessary.

Herein, to overcome the general problems in the surface modification of CNH, I focused on morphology difference in CNH, for instance, conical tip structure of CNH aggregates that is as large as fullerene (size of [60]fullerene: 7.0 Å,<sup>9</sup> Figure 3-1). For the development of a shape-selective surface modification method for CNH aggregates, I chose host-guest interaction as a key to modify a specific site on solid surface precisely.

#### 3.1.2. Host-Guest Complexation of Cyclodextrins with [60]Fullerene

Cyclodextrins (CDs) are cyclic oligomers of  $\alpha$ -D-glucose unit. Since the hydroxy groups are exposed to the outer surface, the outside is hydrophilic but the inner cavity is hydrophobic.<sup>10</sup> Due

to this hydrophobicity of the inner cavity, CDs are usually used as a host molecule for encapsulation of small guest molecules in water via hydrophobic interaction, and CDs dissolve the hydrophobic guest molecules in aqueous media.<sup>10</sup> The encapsulation of guest molecules selectively occurs depending on the size of the inner cavity of CDs (cavity size of  $\alpha$ -CD: 4.7–5.3 Å,  $\beta$ -CD: 6.0–6.5 Å,  $\gamma$ -CD: 7.5–8.4 Å, Figure 3-1).<sup>10, 11</sup>  $\alpha$ -CD,  $\beta$ -CD, and  $\gamma$ -CD are known to encapsulate fullerenes into the inner cavity.<sup>12</sup> In particular,  $\gamma$ -CD forms the most stable water-soluble two to one inclusion complex with fullerenes<sup>12c,12d</sup> and their derivatives<sup>13</sup> due to the suitable cavity size for the size of fullerenes (Figure 3-1). The inclusion complex of  $\gamma$ -CD and [60]fullerene has been prepared by stirring them in aqueous media under reflux condition<sup>12c,12d</sup> or milling at solid state<sup>13</sup>. This inclusion and hydrophilization of fullerene using host-guest complexation with  $\gamma$ -CD have been applied to effective transfer of fullerene from the inclusion complex to a liposome in water to construct a fullerene containing liposome for medical applications using singlet oxygen generation.<sup>13</sup>

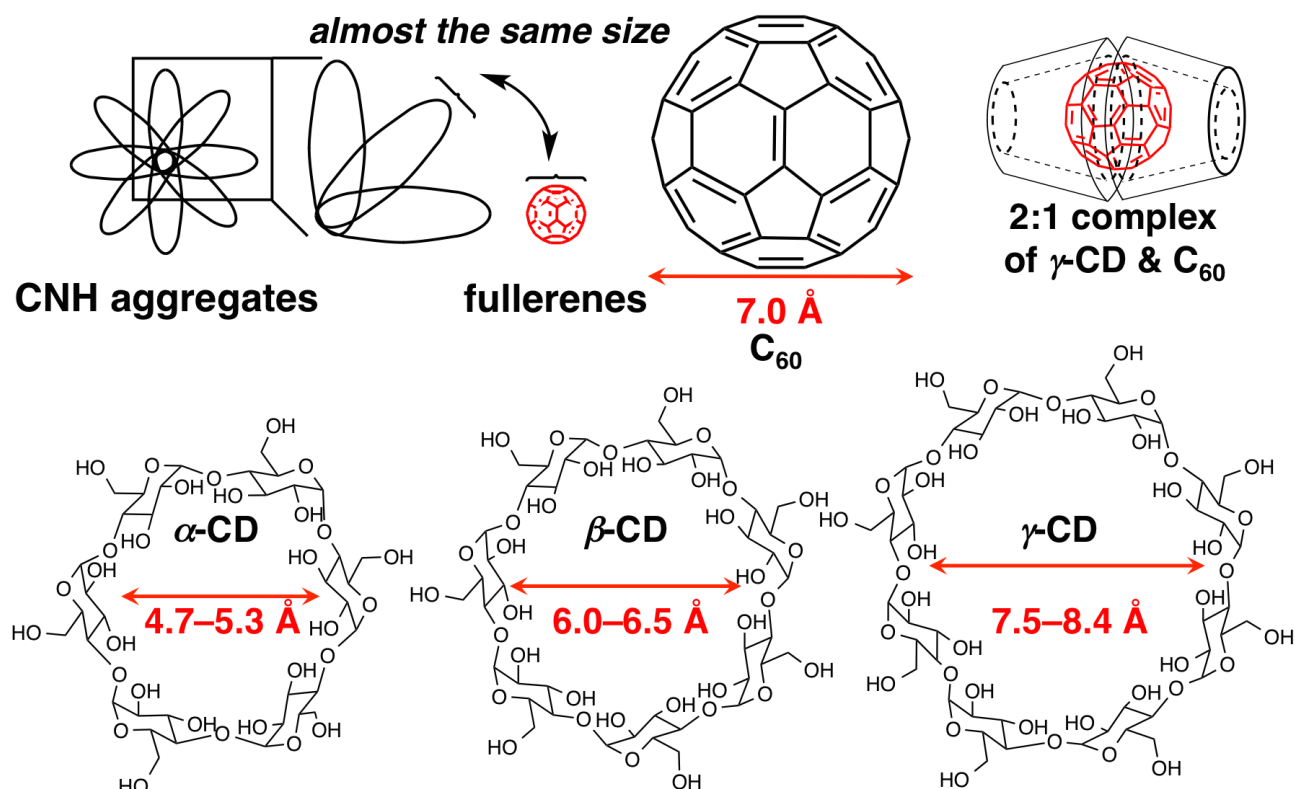


**Figure 3-1.** Molecular structure of [60]fullerene and CDs.

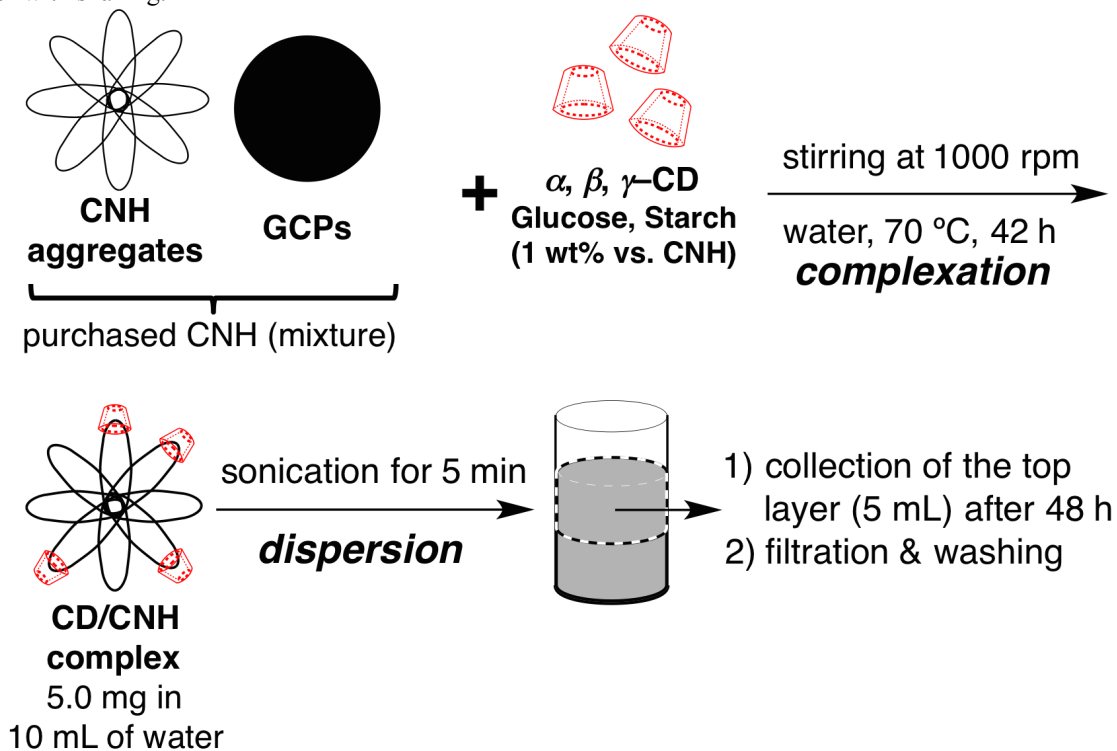
From these insights of encapsulation manner of  $\gamma$ -CD, I surveyed the noncovalent modification of the tip of CNH that is the same size as fullerene with  $\gamma$ -CD via host-guest interaction. I surmised that the shape and size-selective inclusion by  $\gamma$ -CD would be applicable to solid surface recognition for separation of CNH aggregates from a mixture with other nanocarbon particles.

## 3.2. Dispersion of CNH Aggregates in Water with CDs

### 3.2.1. Shape-Selective Recognition of Surface Nanostructure of Nanocarbons via Host-Guest Interaction of CDs

Since CDs are hydrophilic molecule, CNH aggregates were expected to be dispersible in water upon complexation with CDs. I evaluated the complexation on the tip of CNH with CDs by quantification of the dispersibility of CNH aggregates in water. To form a host-guest complex on the tip, I applied conventional complexation method between fullerene and  $\gamma$ -CD.<sup>12d</sup> CNH aggregates (5.0 mg) was mixed with 1 wt% of saccharides ( $\alpha$ -CD,  $\beta$ -CD,  $\gamma$ -CD, D-glucose, or starch from potato) in deoxygenized water (10 mL) with vigorous stirring at 70 °C for 42 h. Since there are about 2000 horns in a 50-150 nm-sized CNH aggregate (formula:  $C_{70,000,000}$ – $C_{170,000,000}$ , ca.  $5.9$ – $14 \times 10^{14}$  horns/1 mg),<sup>5,7</sup> 1 wt% of CDs ( $\alpha$ -CD,  $\beta$ -CD, and  $\gamma$ -CD is 62, 53, and  $46 \times 10^{14}$  molecules/10  $\mu$ g, respectively) is 3–10 equivalent of the number of the horn of CNH aggregates. After long-time stirring, CNH aggregates were precipitated in all the samples. To disperse CNH aggregates, the samples were sonicated in a bath sonicator for 5 min. As expected, CNH aggregates became dispersible in water.

**Scheme 3-1.** Quantification of the dispersibility of CNH aggregates (purchased from NEC, containing 10–20% of GCPs). Power of bath sonicator: 38 kHz, 360 W. The samples were sonicated exactly at the same position in the bath sonicator with shaking.



To check the contents in the dispersed CNH aggregates, thermogravimetric (TG) analysis was carried out because CNH aggregates and  $\mu$ mGCPs show different combustion temperatures due to

the morphology difference.<sup>8,14</sup> Dispersed CNH aggregates were collected by filtration with PTFE membrane filter, washed with water, and finally dried up under vacuum condition with  $P_2O_5$  as a drying reagent. Weight loss of the samples was measured from 30 °C to 1000 °C at the rate of 10 °C/min in dry air atmosphere with a flow rate of 100 mL/min. Combustion signals of CNH aggregates and  $\mu$ mGCPs were detected at 500–740 °C and 740–820 °C, respectively (Figure 3-2b). Combustion signal of  $\gamma$ -CD was detected at 330–550 °C (Figure 3-2a, gray) that was not too much overlapped to combustion signals of CNH aggregates. Purchased CNH showed the both combustion signals and they contained 10 wt% of  $\mu$ mGCPs.

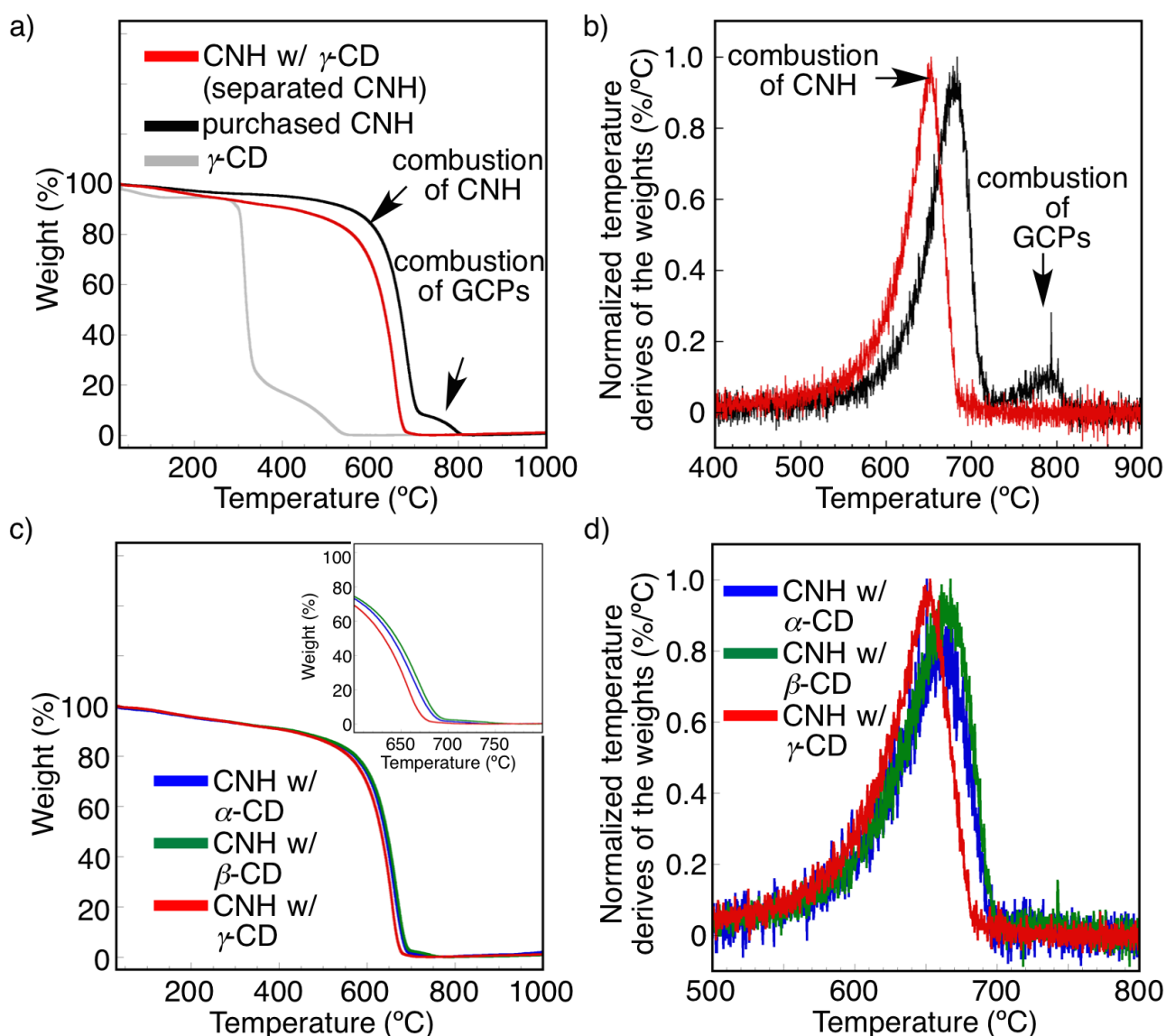


**Figure 3-2.** Thermogravimetric analysis of CNH aggregates. (a) Weight-temperature curve and (b) temperature derivatives of the weights curve of CNH aggregates separated with  $\gamma$ -CD (1 wt%) in water ( $\gamma$ -CD/CNH complex, red), purchased CNH (without separation treatment, black), and  $\gamma$ -CD (gray). Summarized (c) weight-temperature curve and (d) temperature derivatives of the weights curve of CD/CNH complexes (blue:  $\alpha$ -CD/CNH, green:  $\beta$ -CD/CNH, red:  $\gamma$ -CD/CNH). TG analysis was carried out from 30 °C to 1000 °C at a rate of 10 °C/min under dry air flow at 100 mL/min. Samples were taken from top layer of the dispersion liquid 48 h after standing.



### Chapter 3

CNH aggregates were slightly dispersed in water as large agglomerates without any dispersants, but  $\mu\text{mGCPs}$  was remaining (Figure 3-2a, black). In contrast, combustion signal of  $\mu\text{mGCPs}$  was completely disappeared in  $\gamma\text{-CD/CNH}$  complex (Figure 3-2, red). In addition, transmission electron microscopy (TEM) observation revealed that the purchased CNH contain not only  $\mu\text{mGCPs}$  but also sub-100 nm-sized GCPs (nmGCPs, Figure 3-3a). Interestingly nmGCPs that adsorbed on CNH aggregates were also disappeared after dispersion with CDs (Figure 3-3b).

In the separated CNH aggregates with CDs, weight loss was gradually detected from 200 °C and peak top of the combustion signal of CNH aggregates shifted to lower temperature (660 °C) than purchased CNH (690 °C). Considering the surface area and the reactivity of CNH, it is expected that CNH aggregates bearing high surface area, horn-rich CNH aggregates, are more easily combusted than horn-poor CNH aggregates such as bud-shaped and seed-shaped CNH aggregates.<sup>1</sup> Therefore the signal shift indicates that horn-rich CNH aggregates were selectively dispersed in water with CDs. In addition, the same result was also obtained in  $\alpha\text{-CD/CNH}$  complex and  $\beta\text{-CD/CNH}$  complex (See Figure S3-1 in supporting information.), but  $\gamma\text{-CD/CNH}$  complex showed the peak top of the combustion signal at 20 °C lower temperature than other complexes. (Figure 3-2c, d). This difference indicates that  $\gamma\text{-CD}$  more selectively disperses CNH aggregates from a mixture of nanocarbons than other CDs because of the large enough size of inner cavity to encapsulate the tip of CNH. This selectivity is evaluated more and described in the section 3.3.

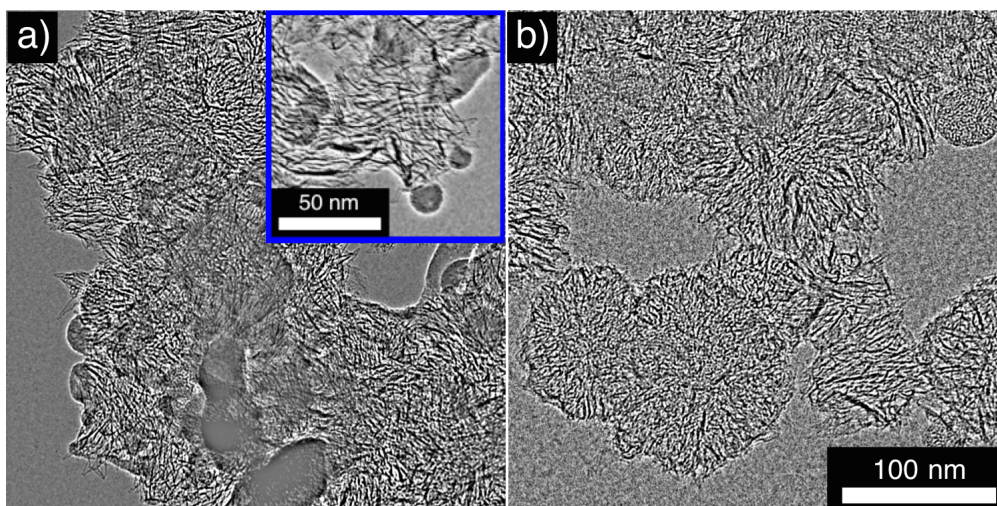


**Figure 3-3.** TEM images of CNH aggregates (a) purchased from NEC and (b) dispersed with  $\gamma\text{-CD}$ . TEM measurement was carried out at an electron acceleration voltage of 120 kV. Low-magnified images are shown in Figure S3-3 in supporting information.

The dispersibility of CNH aggregates were quantified by the amount of dispersed CNH aggregates in the top layer (5.0 mL) of the dispersion liquid 48 h after standing of the dispersion liquid (Scheme 3-1). Amounts of dispersed CNH aggregates recovered from the top layer of

dispersion liquid were summarized in Figure 3-4. CDs dispersed CNH aggregates but D-glucose and starch that have the same unit structure did not. D-glucose is known to disperse CNH aggregates but it needs quite large amount (about 50 times as large amount as CNH aggregates) because D-glucose just physically adsorbs on the wall of CNH.<sup>15</sup> Starch disperses CNT with large amount through physisorption (100 wt% of starch is needed for CNT).<sup>16</sup> However, in this experimental condition, 1 wt% of D-glucose and starch were not enough to disperse CNH aggregates, suggesting that physisorption of the saccharides on the wall of CNH are not so effective for the dispersion. These results also support that CDs disperse CNH aggregates through binding to the tip of CNH.

Host-guest complexation between CD and CNH requires heating to overcome the energy barrier upon complexation.  $\gamma$ -CD dispersed CNH aggregates through stirring at 70 °C and 5 min of sonication, but stirring at 25 °C and 5 min of sonication without the stirring process did not cause dispersion of CNH aggregates (Figure 3-4). It is reported that sonication at room temperature does not induce complexation between the tip and  $\beta$ -CD.<sup>17</sup> In this case, it is expected that  $\beta$ -CD just physically adsorbs on the wall and the groove of CNHs.

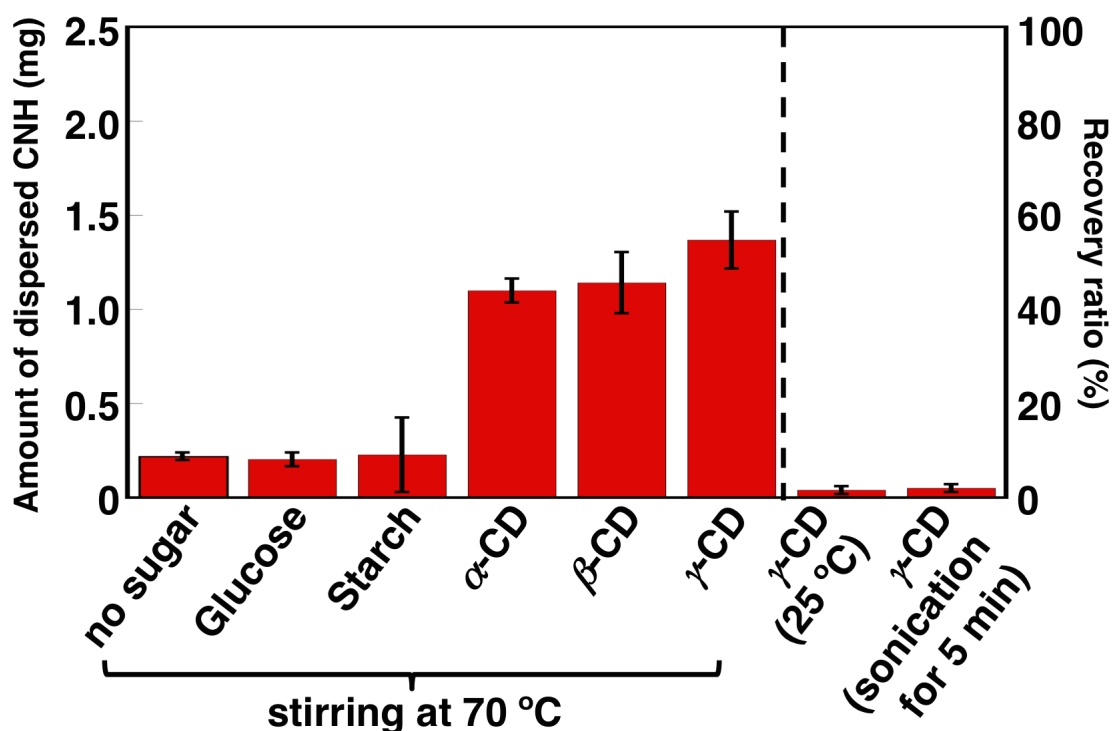


**Figure 3-4.** Amounts of dispersed CNH aggregates recovered from the top layer of dispersion (5 mL). Error bar denotes standard error in three samples.

Graphite and single-walled CNT (CoMoCAT®) were used as other candidates for dispersion using  $\gamma$ -CD as a dispersant. However, these two nanocarbons were not dispersed in water using 1

wt% of  $\gamma$ -CD (Figure 3-5). Since graphite has no cone-shaped structure, and CNT has cone-shaped structure on the tip of CNH but volume of the structure is small due to the micrometer-long architecture,<sup>18</sup>  $\gamma$ -CD did not effectively bind to graphite and CNT and can not disperse them in water.

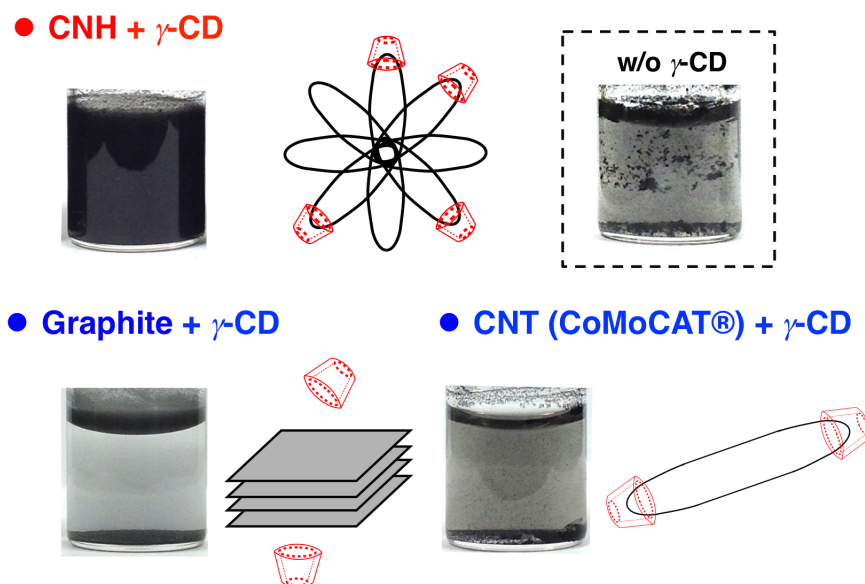


**Figure 3-5.** Dispersion of nanocarbons using  $\gamma$ -CD as a dispersant. The same procedure that is mentioned in Scheme 3-1 was carried out. 1 wt% of  $\gamma$ -CD against nanocarbons was used.

### 3.2.2. Size Effect of CDs for Complexation with CNH

Considering the cavity size of CDs (Figure 3-1), it is expected that  $\gamma$ -CD forms the most stable host-guest complex with the tip of CNH among three CDs ( $\alpha$ ,  $\beta$ , and  $\gamma$ ). To elucidate size effect of CDs for the complexation, I evaluated stability of the dispersion liquid of CD/CNH complexes. In the initial dispersion liquid of CD/CNH complexes, there are unbound CDs in a solution phase that are not adsorbed on CNH. In this condition, attachment and detachment of CDs on the tip is in equilibrium, and CD/CNH complexes were stably dispersed in water for 48 h. When, the unbound CDs were removed by filtration and washing with water, re-dispersion of the CD/CNH complex in pure water causes dissociation of CDs from the tip, resulting in agglomeration of CNH aggregates (Figure 3-6a). Isolated CD/CNH complexes (1 mg) were re-dispersed in water (1 mL) by sonication for 5 min. Dynamic light scattering (DLS) measurement was carried out to trace agglomeration of CD/CNH complexes. 10 min after sonication, all the complexes were dispersed as almost a single particle with unimodal size distribution (average diameter/polydispersity index (PDI): 295 nm/0.391 ( $\alpha$ -CD/CNH), 224 nm/0.241 ( $\beta$ -CD/CNH), 206 nm/0.261 ( $\gamma$ -CD/CNH), See Figure S3-2 in supporting information.). 3 h after sonication,  $\gamma$ -CD/CNH complex was not a single aggregate but still dispersed with unimodal size distribution (average diameter/ PDI: 328 nm/0.515). In contrast,

### Chapter 3

$\alpha$ -CD/CNH complex and  $\beta$ -CD/CNH complex formed micrometer-sized agglomerates (average diameter/ PDI: 441 nm/0.945 ( $\alpha$ -CD/CNH), 557 nm/1.00 ( $\beta$ -CD/CNH))(Figure 3-6b). In addition, 6 h after sonication,  $\alpha$ -CD/CNH complex and  $\beta$ -CD/CNH complex started to precipitate, and they were completely precipitated after 12 h (Figure 3-6c). However, even 12 h after sonication,  $\gamma$ -CD/CNH was dispersed without formation of visible precipitates. As a result of evaluation of dispersibility of CNH aggregates dispersed with CDs, I concluded that  $\gamma$ -CD forms the most stable host-guest complex with a tip and dispersed CNH aggregates stably in water. This result indicates that the host-guest complexation by CDs can be applied for recognition of surface nanostructures and formation of complexes as seen in the complexation with small molecules. Note that from a viewpoint of isolation of CNH aggregates from a mixture of nanocarbons,  $\alpha$ -CD and  $\beta$ -CD are more suitable than  $\gamma$ -CD due to the facility of removal.

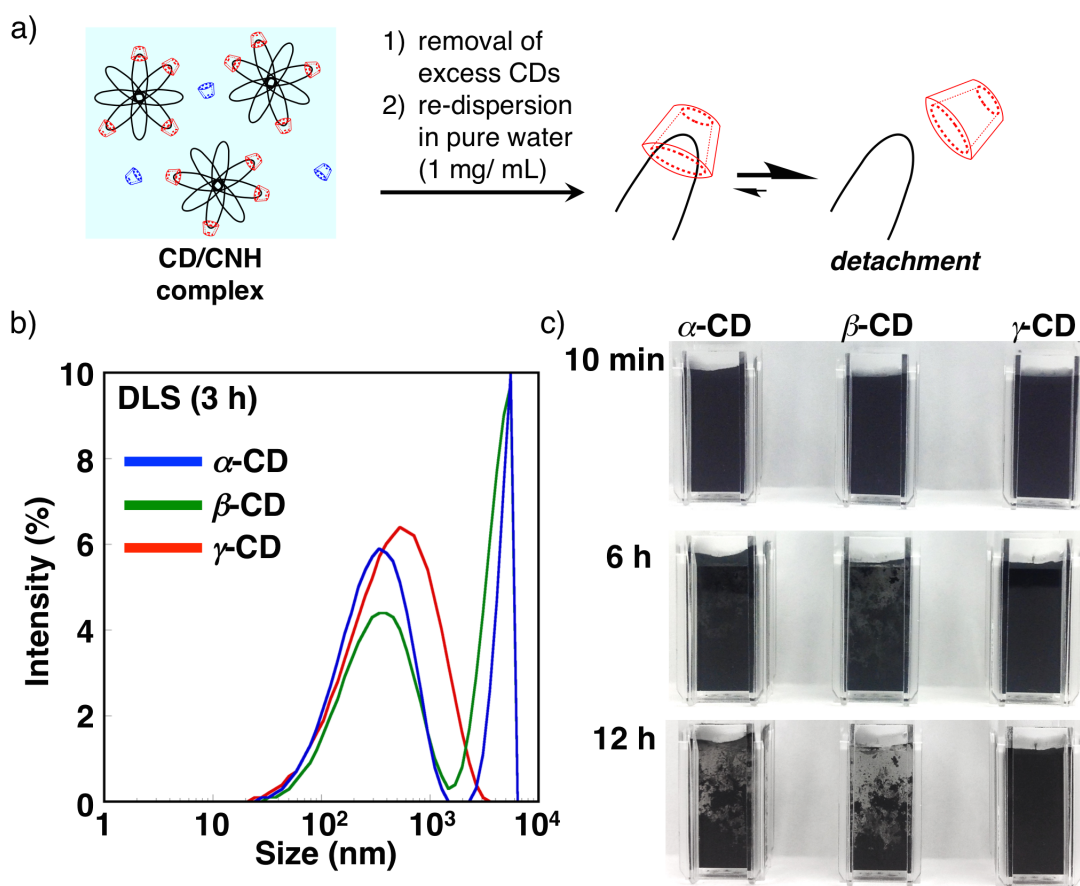


**Figure 3-6.** Evaluation of the size-effect of CDs for encapsulation of the tip of CNH. (a) A procedure for removal of excess CDs from dispersion liquid of CD/CNH complexes (Scheme 3-1) and inducing detachment of CDs from the tip. Power of bath sonicator: 38 kHz, 360 W. The samples were sonicated for 5 min at exactly the same spot in the bath sonicator with shaking. (b) DLS data for re-dispersed CNH complexes with  $\alpha$ -CD (blue),  $\beta$ -CD (green), or  $\gamma$ -CD (red) (1 mg) in water (1 mL) 3 h after sonication at 25 °C. (c) Photos of time-course of dispersion liquid of CNH aggregates with  $\alpha$ -CD (left),  $\beta$ -CD (center), or  $\gamma$ -CD (right).

## Chapter 3

This shape-selective recognition manner of  $\gamma$ -CD for nanocarbons enables separation of different-shaped nanocarbons with high cost-effectiveness. As mentioned in the above paragraph, dahlia-like CNH aggregates were selectively dispersed by  $\gamma$ -CD, and both micrometer-sized and nanometer-sized GCPs were removed from commercially available CNH aggregates. Compared with usual removal method for GCPs from CNH aggregates with surfactant as the dispersant,<sup>8</sup> the cost-effectiveness of CNH aggregate/dispersant in this method is 2500 times higher due to the precise tip-selective modification. In the dispersion liquid of CNH aggregates as shown in Scheme 3-1, only 3.9  $\mu$ M of  $\gamma$ -CD was enough to disperse CNH aggregates due to the nonsurfactant character and the host-guest binding property compared with conventional surfactants that are adsorbed on nanocarbons and disperse them above critical micelle concentration.<sup>19</sup>

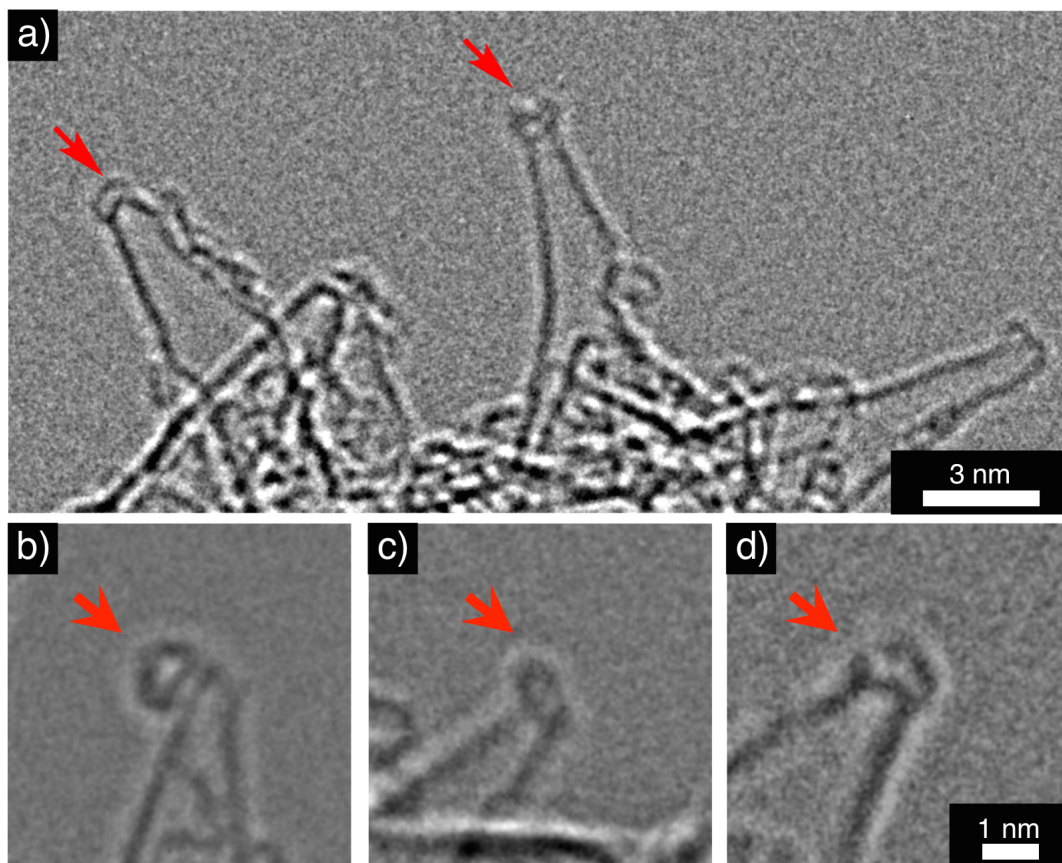
### 3.3. Single-Molecule TEM Imaging of CD/CNH Complex

#### 3.3.1. Molecular-Level Structure of the Host-Guest Complex of CNH and CDs

As mentioned in the previous section, it is revealed that the size of CDs affects the water-dispersibility of CNH aggregates. The cavity of  $\gamma$ -CD is large enough to form a stable host-guest complex with the tip of CNH, while that of  $\alpha$ -CD and  $\beta$ -CD are too small to form it because the average size of the tip is larger than the size of [60]fullerene (7.0 Å). Therefore, I hypothesized that the difference in water-dispersibility among three CDs originates in the difference in the molecular-level structure of the host-guest complexes. Here I demonstrate the molecular-level binding structure of CDs on the nanohorns using TEM measurement.

In TEM sample preparation, CD/CNH complexes (ca. 0.1 mg) were dispersed in water (1 mL) by 10 seconds of sonication, and then the dispersion was placed on a TEM microgrid and excessive amount of water was blotted by filter paper. TEM measurements were performed on TEM with 0.8 Å–3 Å of point resolution at an electron acceleration voltage of 120 kV.

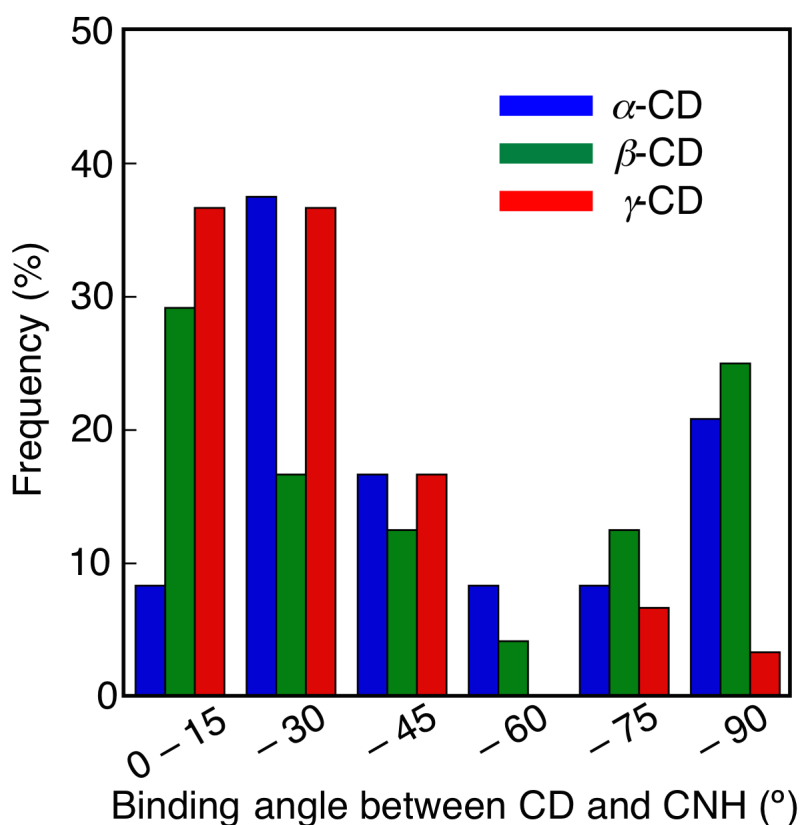
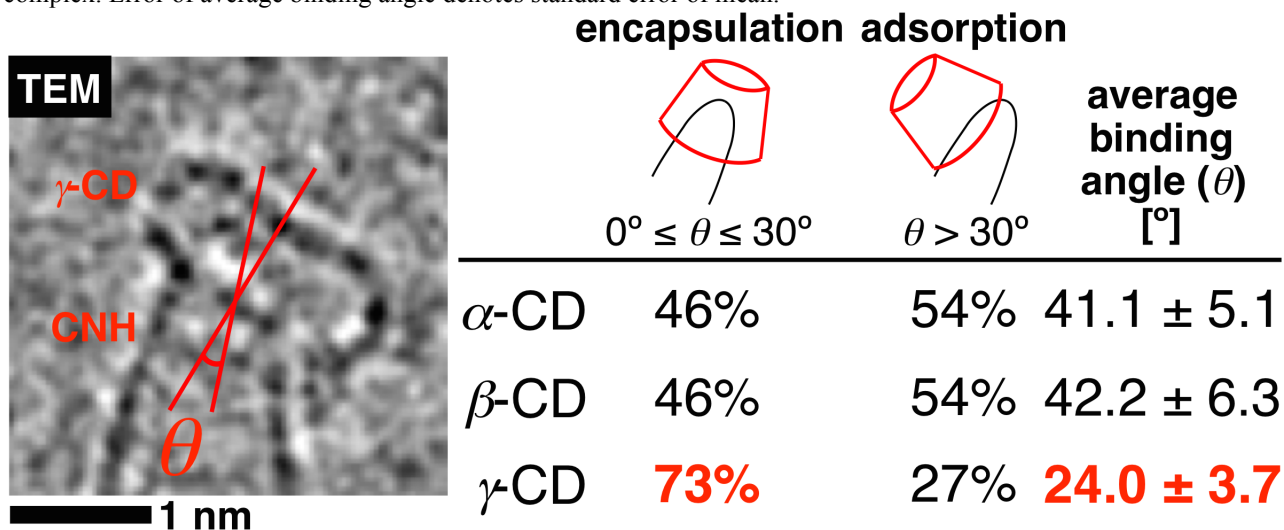
Like covalent-bound organic residues on the tip of CNH,<sup>6</sup> host-guest complexes of CD on the tip of CNH were successfully observed by TEM (Figure 3-7). In the TEM images, I found that 40% of the nanohorns were covered with  $\gamma$ -CD molecules (calculated from 75 CNHs). Binding of  $\alpha$ -CD and that of  $\beta$ -CD on the tip were also observed, but the binding yields were 21% and 29%, respectively.



**Figure 3-7.** Representative TEM images of CD-bound CNHs at an electron acceleration voltage of 120 kV. (a) Low-magnified image of  $\gamma$ -CD-bound CNHs. Scale bar is 3 nm. Magnified image of (b)  $\alpha$ -CD-bound CNHs, (c)  $\beta$ -CD-bound CNHs, (d)  $\gamma$ -CD-bound CNHs. CDs are denoted with red arrows.

The binding structure of CDs on the tip of CNH was evaluated by a binding angle ( $\theta$ ) between two axes of CD and CNH in TEM image (Table 3-1). I categorized the binding structures into two types: encapsulation ( $0^\circ \leq \theta \leq 30^\circ$ ) and adsorption ( $\theta > 30^\circ$ ). Average binding ratio and angles for  $\alpha$ -CD,  $\beta$ -CD, and  $\gamma$ -CD are summarized on the table in Table 3-1 and histograms from the binding angle is shown in Figure 3-8. Both  $\alpha$ -CD and  $\beta$ -CD form the host-guest complexes with 46% of encapsulation and 54% of adsorption, and the average binding angles are  $41.1^\circ$  for  $\alpha$ -CD and  $42.2^\circ$  for  $\beta$ -CD, respectively. In contrast, most of  $\gamma$ -CD molecules bind to CNH by encapsulation (73%), and the average binding angle of  $24.0^\circ$  and the angle distribution are much smaller than those of  $\alpha$ -CD and  $\beta$ -CD. This result clearly indicates that  $\gamma$ -CD binds to CNH through encapsulation of the spherical tip, whereas  $\alpha$ -CD and  $\beta$ -CD bind mainly through physisorption. In other words host molecule binds to specific structure on solid surface through size-selective host-guest interaction. Considering the ratio of binding of CDs on the tip of CNH aggregates, the ratio of binding of CDs by encapsulation are 9.6%, 13%, and 30% for  $\alpha$ -CD,  $\beta$ -CD, and  $\gamma$ -CD, respectively. Therefore,  $\gamma$ -CD/CNH complex was stably dispersed for a long time but  $\alpha$ -CD/CNH complex and  $\beta$ -CD/complex were not.

**Table 3-1.** Evaluation of binding mode of CDs to the tip of CNH by calculation of the binding angle between CD and CNH. Left: TEM image of  $\gamma$ -CD/CNH complex was measured at an electron acceleration voltage of 120 kV. Axis of  $\gamma$ -CD and CNH are denoted with red line. Right: summary of the ratio of binding mode and average binding angles, Number of observed CD/CNH complexes are 24 for  $\alpha$ -CD/CNH complex and  $\beta$ -CD/complex, and 30 for  $\gamma$ -CD/CNH complex. Error of average binding angle denotes standard error of mean.

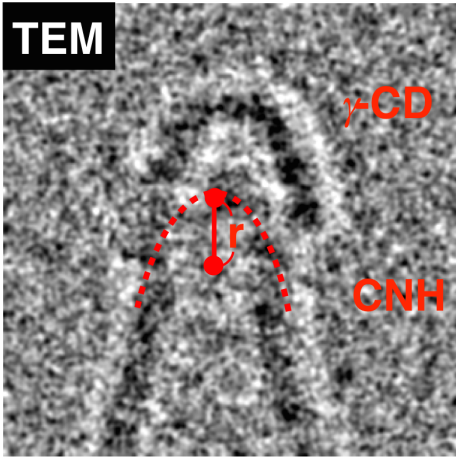


**Figure 3-8.** Histograms from the binding angle between CNH and CD,  $\alpha$ -CD (blue),  $\beta$ -CD (green), and  $\gamma$ -CD (red). The distribution was obtained from more than 24 CNHs in each sample.

### Chapter 3

Next, the host-guest complexation of CDs on the tip of CNH was evaluated from the curvature of the tip. I measured the radius of curvature of the tip of CD-bound CNH with encapsulation manner (binding angle:  $0^\circ \leq \theta \leq 30^\circ$ ). Radius of curvature of the tip ( $r$ , Table 3-2, left image) was calculated by the equation derivatized from Pythagorean theorem using fitting lines described in Figure S3-5 in supporting information. Histograms from radius of curvature of the tip and CD-encapsulated CNH are summarized in Figure 3-9. CNH has large size distribution on the radius of curvature of the tips in the range of 3.5–20 Å (Figure 3-9, black). The tips where the CDs bind, however, showed narrower size distribution suggesting CDs preferentially bind to tips with small curvature. Interestingly,  $\gamma$ -CD-encapsulated CNH shows smaller average radius of curvature of the tip (3.9 Å) than  $\alpha$ -CD-encapsulated CNH (4.4 Å) and  $\beta$ -CD-encapsulated CNHs (4.5 Å) (Table 3-2). Since the radius of inner cavity of  $\gamma$ -CD is 3.8–4.2 Å (Figure 3-1)<sup>11</sup>,  $\gamma$ -CD binds to a suitable-sized tip selectively and forms a host-guest complex. In contrast,  $\alpha$ -CD and  $\beta$ -CD bind to the tip that they cannot encapsulate into their cavity (radius of cavity of  $\alpha$ -CD: 2.4–2.6 Å,  $\beta$ -CD: 3.0–3.3 Å), therefore, they are attached on the curved surface of CNH but do not incorporate the spherical tip into their cavity due to the size mismatch. Since binding stability of CDs on large tips of CNH is expected to be less than that bound on suitable small tips,  $\alpha$ -CD and  $\beta$ -CD are more easily detached from the tips than  $\gamma$ -CD. This difference in binding selectivity difference in CDs is also corresponding to the stability of dispersion of CNH aggregates dispersed with CDs.

**Table 3-2.** Evaluation of size of the tip of CD-encapsulated CNH. Left: TEM image of  $\gamma$ -CD-encapsulated CNH. Surface curvature of CNH is denoted with red broken line. TEM image of  $\gamma$ -CD/CNH complex was measured at an electron acceleration voltage of 120 kV. Right: average radius of curvature ( $r$ ) of the tip of CD-encapsulated CNH, Number of observed encapsulated CNH is 10 for  $\alpha$ -CD and  $\beta$ -CD, and 20 for  $\gamma$ -CD.

TEM	average radius of curvature ( $r$ ) of the tip of CD-encapsulated CNH [Å]	
	CD Type	Value
	$\alpha$ -CD	$4.4 \pm 0.4$
	$\beta$ -CD	$4.5 \pm 0.3$
	$\gamma$ -CD	<b><math>3.9 \pm 0.2</math></b>



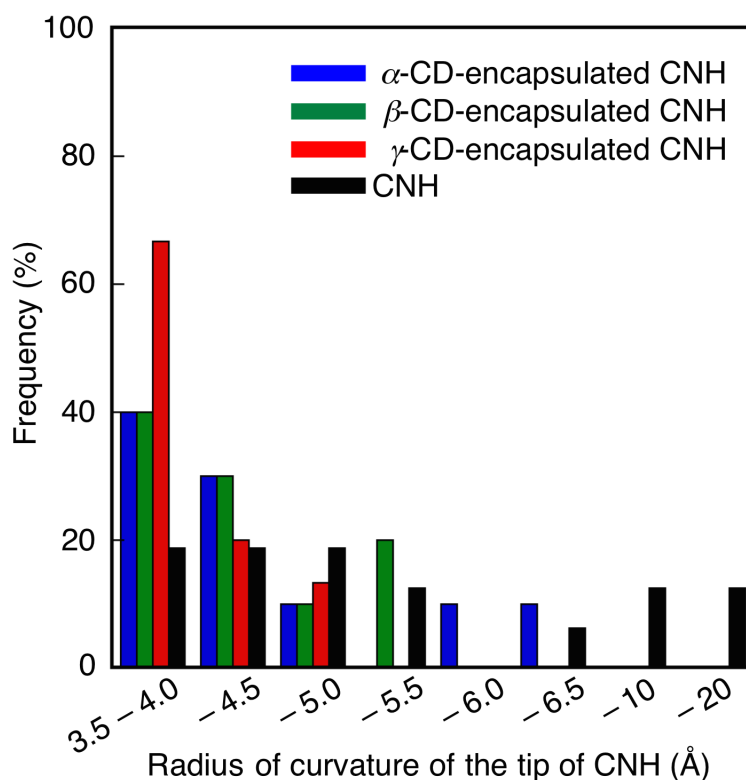


**Figure 3-9.** Histograms from radius of curvature of the tip of CNH encapsulated by  $\alpha$ -CD (blue),  $\beta$ -CD (green), and  $\gamma$ -CD (red). Histogram from radius of curvature of the tip of whole CNH (black). The distribution was obtained from more than 10 CNHs in each sample.

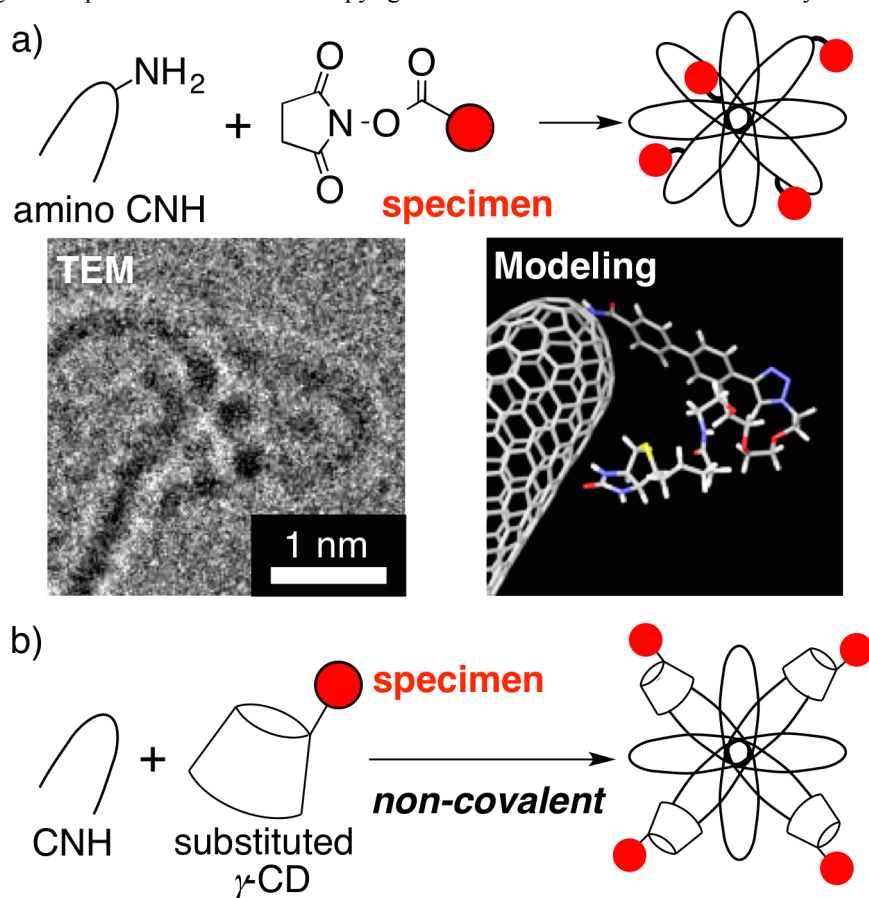
### 3.3.2. Single-Molecule Atomic Real-Time TEM Observation of $\gamma$ -CD

As one of the applications of CNH, Nakamura et al. reported a TEM observation technique for organic molecules using CNH as a specimen support. Specimens bonded to the tip of CNH via covalent amide bonding are observed in atomic resolution (Scheme 3-2a).<sup>5,6</sup> Nakamura et al. applied this modification method of CNH to noncovalently capture target molecules by functional groups bonded to the tip as a fishhook. For example, aromatic molecule was successfully captured on the tip via van der Waals interaction.<sup>20</sup> However, the modification yield on CNH via covalent bonding is less than 10%. In addition, it is quite difficult to confirm that specimen molecules are really immobilized of the tip before TEM observation. Herein, I applied the tip-selective modification of CNH using  $\gamma$ -CD as another non-covalent method for immobilization of specimens (Scheme 3-2b). This strategy can solve the problems in covalent immobilization method, the low modification yield and the difficulty in confirmation of the modification. It is already mentioned in above paragraphs that  $40 \pm 5\%$  of CNH was modified with  $\gamma$ -CD, and CNH aggregates became disperse in water upon the complexation. The bound  $\gamma$ -CD molecule on the CNH was clearly observed by TEM with atomic resolution. In addition, therefore specimens can be easily immobilized on CNH by mixing the specimen-binding  $\gamma$ -CD in water and that can be traced by estimation of the water-dispersibility of CNH aggregates. Another advantage of utilization of CD for TEM imaging that functionalization

### Chapter 3

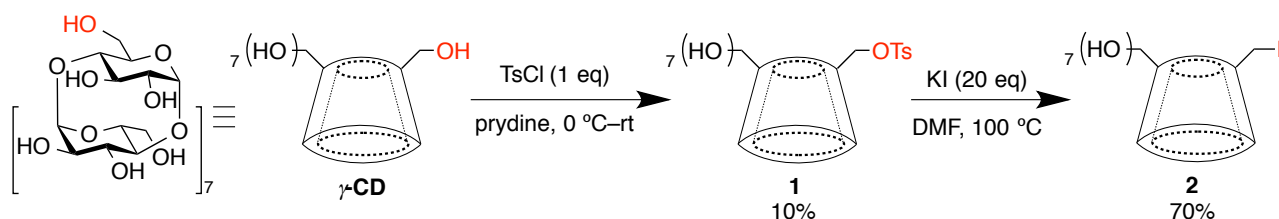
of  $\gamma$ -CD has been widely established.<sup>21</sup> Therefore, many specimens can be easily bound to  $\gamma$ -CD.

**Scheme 3-2.** Immobilization of specimens on CNH by (a) covalent method or (b) non-covalent method. (a) TEM image and modeling image are reprinted from ref. 38c Copyright © 2015 American Chemical Society.



To demonstrate the non-covalent specimen immobilization on CNH for single-molecule atomic real-time (SMART) TEM observations, I synthesized a specimen-binding  $\gamma$ -CD derivative with reference of conventional synthetic approaches for CD derivatives.<sup>21</sup> As a proof of principle study, iodine was selected as a marker for TEM imaging because of the high contrast of the heavy atom. Mono-6-*O*-(*p*-toluenesulfonyl)- $\gamma$ -CD (Ts- $\gamma$ -CD **1**) was synthesized as a versatile intermediate for further substitution reactions,<sup>21b</sup> which was converted into mono(6-doxy-6-iodo)- $\gamma$ -CD (I- $\gamma$ -CD **2**, Scheme 3-3).

Observation of  $\gamma$ -CD and I- $\gamma$ -CD **2** was carried out by a Cs-corrected JEOL JEM-ARM200F at an electron acceleration voltage of 120 kV. TEM samples were prepared by the same complexation method mentioned in Scheme 3-1. To place the samples on TEM microgrid, the obtained complexes were dispersed in toluene to avoid detachment of  $\gamma$ -CDs from the tip of CNH, because complexation of  $\gamma$ -CD is in equilibrium in water as mentioned in the previous section.

Scheme 3-3. Synthesis of specimen-binding  $\gamma$ -CD derivative.

$\gamma$ -CD molecules were observed as trapezoid or rectangular-shaped structures composed of high contrast dots without decomposition during the observation for several minutes (Figure 3-10). Judging from the contrast profile of a TEM image, top (Figure 3-10, middle, blue) and side (Figure 3-10, middle, green) of the object showed strong contrast, but the contrast of the bottom (Figure 3-10, middle, red) is relatively weaker than the others. Contrast of TEM image becomes strong by increase in the probability of electron scattering, and the probability increases when electrons pass through high atomic density position. Since more than two glucose units of  $\gamma$ -CD are overlapped on the side and the atomic density is very high, contrast of the side is very strong. In addition,  $\gamma$ -CD has eight  $\text{CH}_2\text{OH}$  groups on the upper-rim, and the opposite and the neighbor groups are overlapped from the aspect on the TEM image in Figure 3-10. Therefore, the top of the observed structure that shows strong contrast is corresponding to upper-rim of  $\gamma$ -CD. In contrast, since opposite hydroxy groups on the lower-rim of  $\gamma$ -CD are overlapped but the neighbors are not, the bottom of the observed structure that shows relatively weak contrast is corresponding to the lower-rim of  $\gamma$ -CD. The binding direction is further evaluated using I- $\gamma$ -CD **2** described in the below paragraph.

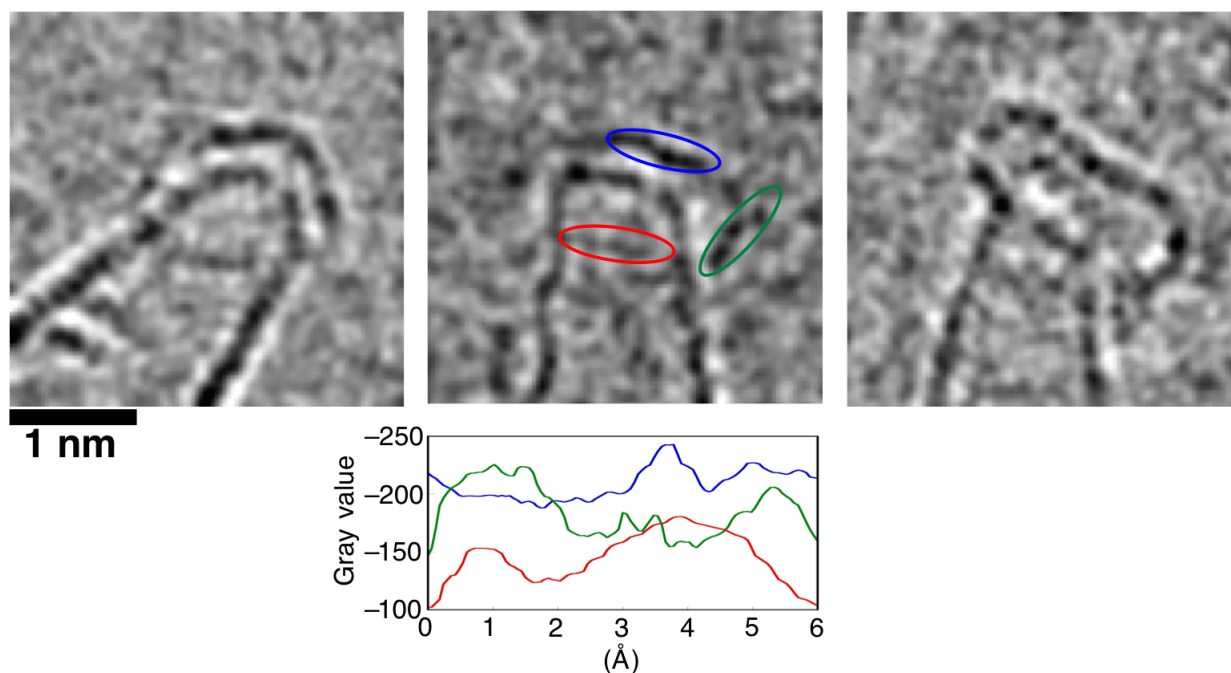
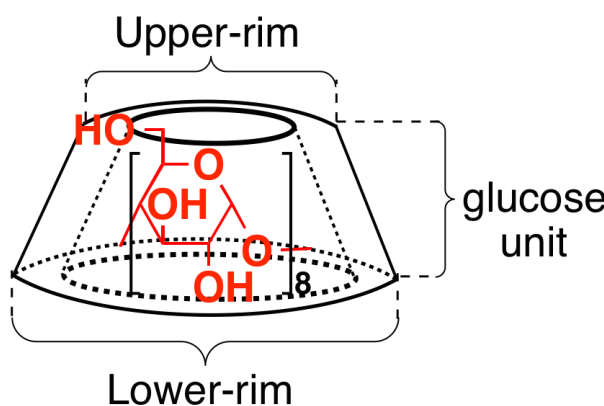


**Figure 3-10.** Representative TEM images of  $\gamma$ -CD/CNH complexes were measured at an electron acceleration voltage of 120 kV. Bottom: contrast profile of middle TEM image (blue: top, green: side, and red: bottom of  $\gamma$ -CD structure).

Conformation of  $\gamma$ -CD was changed upon formation of the host-guest complex with the tip of CNH. Length of each side of  $\gamma$ -CD, upper-rim, lower-rim, and glucose unit in TEM images are summarized in Table 3-3. The length is shown as an average value of three TEM images shown in Figure 3-10. The length of glucose unit ( $7.7 \pm 0.3 \text{ \AA}$ ) was almost the same length as that of free- $\gamma$ -CD in a crystal ( $7.8 \text{ \AA}$ )<sup>11</sup> due to the structure robustness. In contrast, the length of upper-rim and the lower-rim of  $\gamma$ -CD differ from those of crystal structure. The upper-rim was shorter, and the lower-rim was longer than in the crystal, respectively. This size differences was derived from conformational change of  $\gamma$ -CD upon formation of the host-guest complex with the tip. The lower-rim of  $\gamma$ -CD was spread to maximize van der Waals contact with the CNH tip, whereas the upper-rim was enabled to minimize the distortion upon complexation (Figure 3-11).

**Table 3-3.** Length of each side of  $\gamma$ -CD, upper-rim, lower-rim, and glucose unit in  $\gamma$ -CD/CNH complex.



	Length [ $\text{\AA}$ ]	
	TEM	Crystal
Upper-rim	$14.9 \pm 2.7$	16.1
Lower-rim	$18.0 \pm 0.7$	16.9
glucose unit	$7.7 \pm 0.3$	7.8

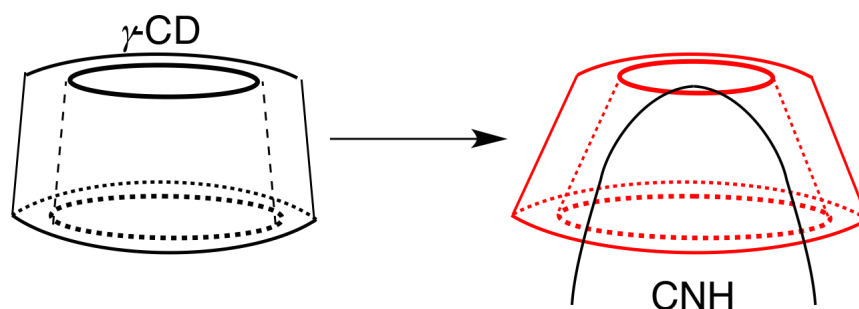


**Figure 3-11.** Illustration of conformational change of  $\gamma$ -CD upon formation of the host-guest complex with CNH.

TEM molecular modeling and simulation were carried out to confirm what we see is of  $\gamma$ -CD. The molecular model of  $\gamma$ -CD was optimized by molecular mechanics calculations using Compass force field implemented in Materials Studio (Figure 3-12, right).<sup>22</sup> Considering the structure robustness of glucose unit of  $\gamma$ -CD, conformation was adjusted by rotation of the glycosidic linkage between the glucose units, and C6 methylene group of the glucose units. TEM simulation images

were generated from the modeling images for each structure by using a procedure implemented in a standard simulation software (Figure 3-12, middle).<sup>23</sup> High contrast dots on both upper-rim and lower-rim of  $\gamma$ -CD were reproduced by the overlap of oxygen atoms on the rims, or overlap of oxygen atom of the glucose unit and carbon atoms of CNH (Figure S3-6e). However, the simulation image was not completely matched to the corresponding TEM image because conformation of  $\gamma$ -CD changed during the beam exposure time of 0.4 seconds.

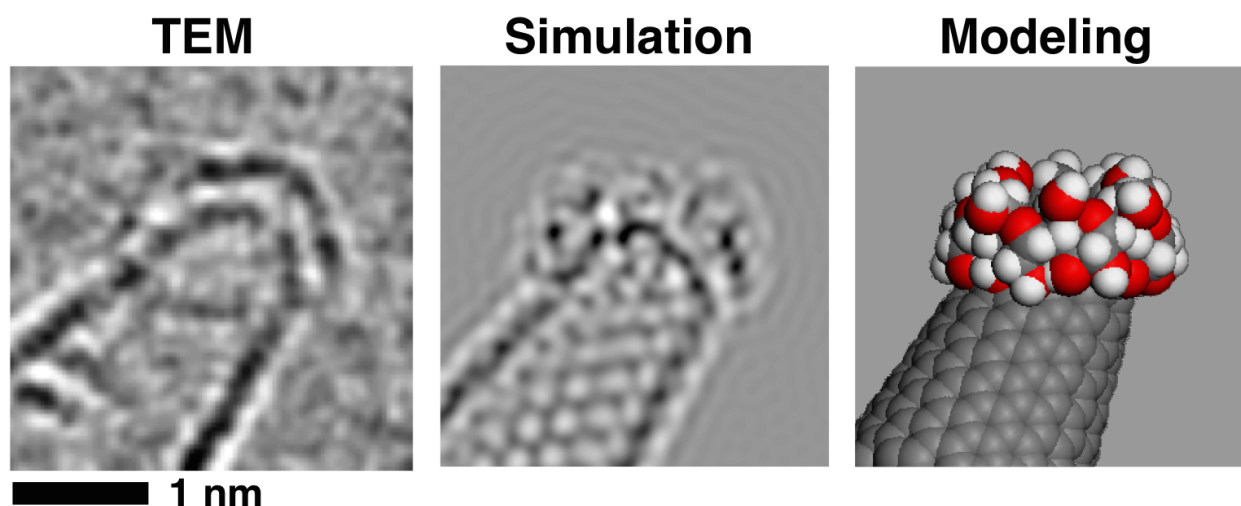


**Figure 3-12.** TEM image of  $\gamma$ -CD bound on the tip of CNH (left), the simulation image (middle), and the modeling image (right, gray: carbon, white: hydrogen, red: oxygen). TEM measurement was measured at an electron acceleration voltage of 120 kV.

Next, I- $\gamma$ -CD **2** was visualized and characterized by SMART-TEM. In TEM images, high contrast dots are observed both outside and inside of the CD structure (Figure 3-13a, left, Figure S3-4 in supporting information). Simulation and modeling of the TEM image were carried out by the same method as mentioned in the previous paragraph, and the TEM image was well reproduced by the simulated image (Figure 3-13a, middle and right). The high contrast probably the iodine atom gave information about the direction in the capping of  $\gamma$ -CD on the tip of CNH. Since iodine is substituted at C6 carbon of the glucose unit that is on the upper-rim of  $\gamma$ -CD, the image inevitably indicates that  $\gamma$ -CD encapsulates the tip from the lower-rim. In the movie of observed I- $\gamma$ -CD **2**, the iodine atom disappeared in some frames (Figure 3-13b, Figure S3-12 in supporting information). Because of the rotation of C6 methylene group substituted with iodine, iodine atom was overlapped with  $\gamma$ -CD or CNH scaffold (Figure S3-8, Figure S3-9 in supporting information).

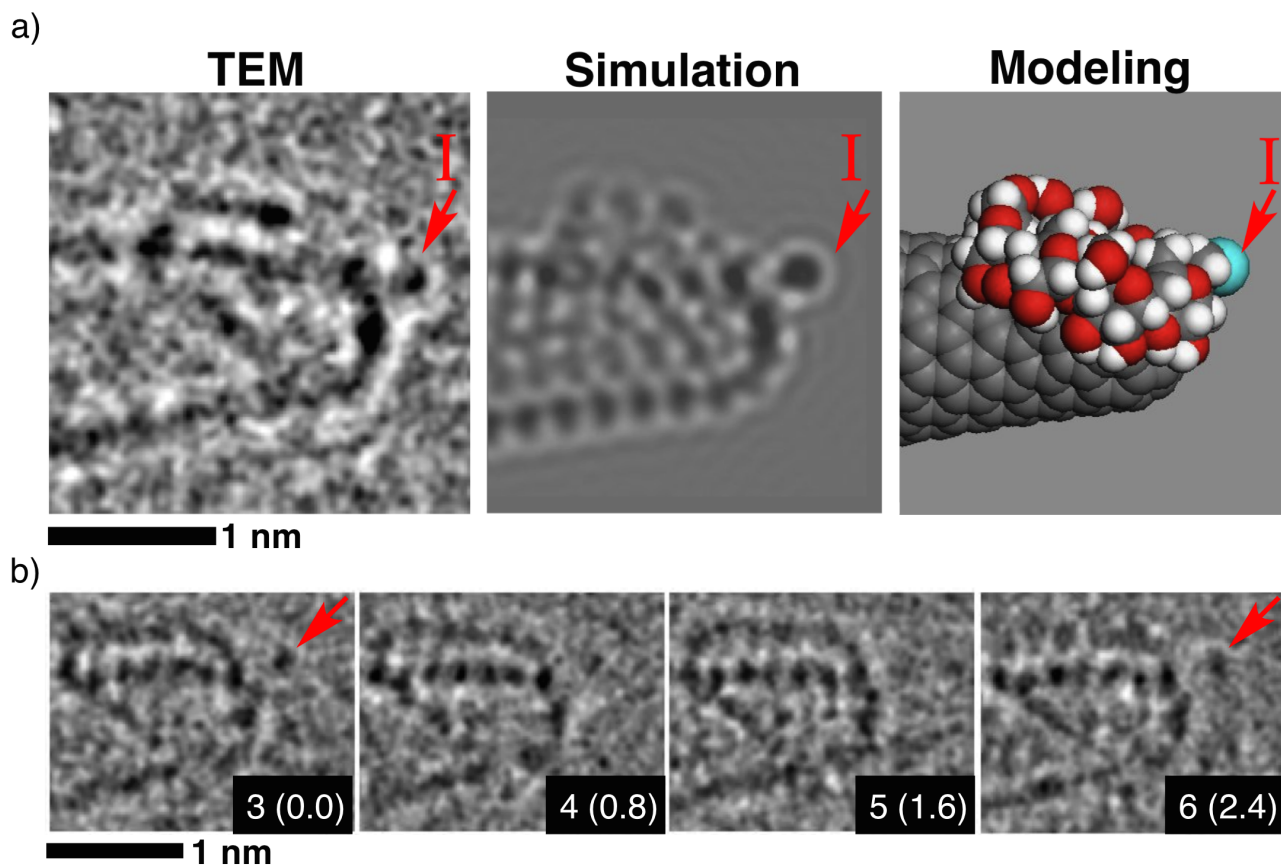


**Figure 3-13.** TEM image of I- $\gamma$ -CD **2** bound on the tip of CNH (a, left), the simulation image (a, middle), and the modeling image (a, right, gray: carbon, white: hydrogen, red: oxygen, pale blue: iodine). (b) Representative TEM images of **2**. The numbers refer to the frame number in the movie as shown in Figure S3-11 in supporting information. Time is shown inside the parenthesis in seconds. Iodine is denoted with a red arrow. TEM measurement was measured at an electron acceleration voltage of 120 kV.

To quantify the molecular motion of  $\gamma$ -CD and I- $\gamma$ -CD **2**, I carried out cross-correlation analysis of the sequential TEM images. Gorgoll et al. reported a quantification method of molecular motion observed by TEM using cross-correlation ( $\gamma$ ) between consecutive two TEM images (Figure 3-14, left bottom).<sup>6b</sup> Briefly, cross-correlation factor of 1 means perfect match between the two images that indicates no motion in the structures. In contrast, cross-correlation factor of 0 means no match between them that indicates motion of structures. Cross-correlation of the area of CNH region ( $0.77 \pm 0.09$ , black area in Figure 3-14) was collected to quantify the background motion of the images. Compared with cross-correlation value of CNH, that of upper-rim of  $\gamma$ -CD was smaller ( $0.66 \pm 0.08$ , red area in Figure 3-14). This result suggests that conformation of  $\gamma$ -CD was changed during the TEM observation, in other words,  $\gamma$ -CD is more mobile than CNH.

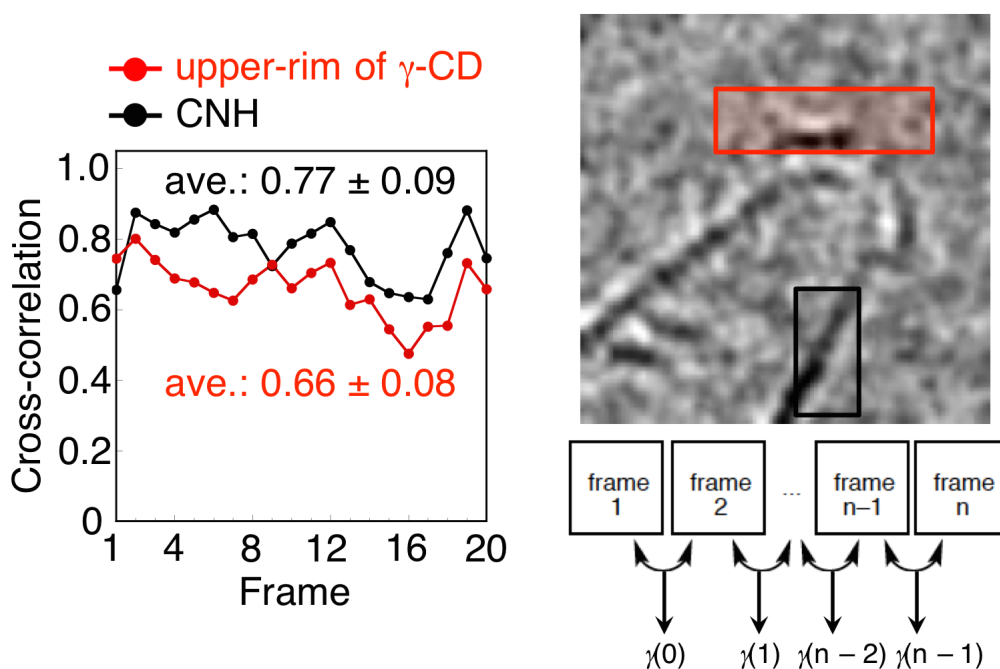


**Figure 3-14.** Cross-correlation analysis of  $\gamma$ -CD/CNH complex. Cross correlation ( $\gamma$ ) calculated from consecutive frames of the movie of image in Figure 3-12.

TEM image of I- $\gamma$ -CD **2** was separated into three different rectangular areas (area 1 (black): CNH, area 2 (green): I- $\gamma$ -CD/CNH complex, area 3 (red): I- $\gamma$ -CD, Figure 3-15b). Cross-correlation of these three areas were calculated from the corresponding consecutive images (Figure 3-15a, Figure S3-12 in supporting information). Compare with cross-correlation of area 1, area 2 showed almost the same cross-correlations through out the movie. Therefore,  $\gamma$ -CD moiety did not move so much. In contrast, cross-correlation of area 3 was significantly smaller than that of area 1. Especially, cross-correlation decreased between frames 6–7, 13–14, and 27–28 indicated by star in Figure 3-15. At these neighboring pairs of frames, appearance and disappearance of iodine atom were clearly observed (Figure S3-12). As a result,  $\gamma$ -CD scaffold was fixed by host-guest interaction on the tip of CNH, but C6 methylene group of the glucose unit of  $\gamma$ -CD frequently moved.

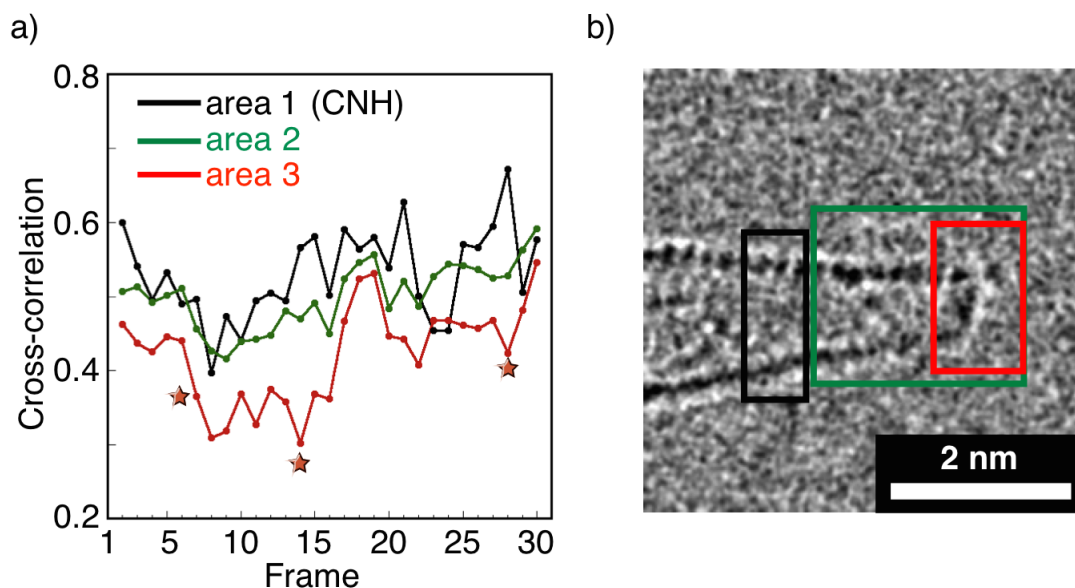


**Figure 3-15.** Cross-correlation analysis of I- $\gamma$ -CD/CNH complex. (a) Cross correlation calculated from consecutive frames of the movie of image a in Figure S3-4 in supporting information. (b) Representative image and calculation area (black: area 1, green: area 2, red: area 3). All the calculated TEM images were shown in Figure S3-10, Figure S3-11, and Figure S3-12 in supporting information. Stars indicate significant decrease of cross-correlation corresponding to appearance or disappearance of iodine atom emphasized by red rectangles in Figure S3-12.

### 3.4. Conclusion

In conclusion, shape-selective surface modification of a nanocarbon was achieved by host-guest interaction of CDs. Especially  $\gamma$ -CD recognized the cone-shaped tip aggregates with high size selectivity and formed a stable host-guest complex. Upon complexation, hydrophobic CNH aggregates became water-dispersible, and horn-less GCPs were removed in the following separation process. As a dispersion and separation method of CNH aggregates, this surface modification method is quite effective compared with conventional methods using surfactants as a dispersant. In addition, CDs are biocompatible and should be easily removed by acid treatment or enzymes. This is an advantage of CDs as dispersant for bioapplication of CNHs. The host-guest complex of  $\gamma$ -CD and the tip of CNH was clearly observed by TEM measurement with atomic resolution. This high-resolution TEM imaging gave evidence for the boundary between the molecular-level structure and the water-dispersibility of CD/CNH complex. Since substituted iodine of  $\gamma$ -CD was observed, various kinds of specimens will be bound to CNH and observed by TEM using  $\gamma$ -CD as a fishhook.



## 3.5. References

- <sup>1</sup> Iijima, S.; Yudasaka, M.; Yamada, R.; Bandow, S.; Suenaga, K.; Kokai, F.; Takahashi, K. *Chem. Phys. Lett.* **1999**, *309*, 165–170.
- <sup>2</sup> Bekyarova, E.; Murata, K.; Yudasaka, M.; Kasuya, D.; Iijima, S.; Tanaka, H.; Kahoh, H.; Kaneko, K. *J. Phys. Chem. B* **2003**, *107*, 4681–4684.
- <sup>3</sup> Kosaka, M.; Kuroshima, S.; Kobayashi, K.; Sekino, S.; Ichihashi, T.; Nakamura, S.; Yoshitake, T.; Kubo, Y. *J. Phys. Chem. C* **2009**, *113*, 8660–8667.
- <sup>4</sup> (a) Murakami, T.; Ajima, K.; Miyawaki, J.; Yudasaka, M.; Iijima, S.; Shiba, K. *Mol. Pharm.* **2004**, *1*, 399–405. (b) Ajima, K.; Yudasaka, M.; Murakami, T.; Maigne, A.; Shiba, K.; Iijima, S. *Mol. Pharm.* **2005**, *2*, 475–480.
- <sup>5</sup> Isobe, H.; Tanaka, T.; Maeda, R.; Noiri, E.; Solin, N.; Yudasaka, M.; Iijima, S.; Nakamura, E. *Angew. Chem. Int. Ed.* **2006**, *45*, 6676–6680.
- <sup>6</sup> (a) Nakamura, E.; Koshino, M.; Tanaka, T.; Niimi, Y.; Harano, K.; Nakamura, Y.; Isobe, H. *J. Am. Chem. Soc.* **2008**, *130*, 7808–7809. (b) Gorgoll, R. M.; Yücelen, E.; Kumamoto, A.; Shibata, N.; Harano, K.; Nakamura, E. *J. Am. Chem. Soc.* **2015**, *137*, 3474–3477.
- <sup>7</sup> Zhu, S. Xu, G. *Nanoscale* **2010**, *2*, 2538–2549.
- <sup>8</sup> Zhang, M.; Yudasaka, M.; Miyawaki, J.; Fan, J.; Iijima, S. *J. Phys. Chem. B* **2005**, *109*, 22201–22204.
- <sup>9</sup> Kroto, H. W.; Heath, J. R.; O'Brien, S. C.; Curl, R. F.; Smalley, R. E. *Nature* **1985**, *318*, 162–163.
- <sup>10</sup> (a) Dodziuk, H. *Cyclodextrins and Their Complexes: Chemistry, Analytical Methods, Applications*, Wiley-VCH, Weinheim, 2006. (b) Crini, G. *Chem. Rev.* **2014**, *114*, 10940–10975.
- <sup>11</sup> Martin Del Valle, E. M. *Process Biochemistry* **2004**, *39*, 1033–1046.
- <sup>12</sup> (a) Zhang, Y. Y.; Liu, W.; Gao, X.; Zhao, Y.; Zheng, M.; Lia, F.; Ye, D. *Tetrahedron Lett.* **2006**, *47*, 8571–8574. (b) Murthy, C. N.; Geckeler, K. E. *Chem. Commun.* **2001**, *13*, 1194–1195. (c) Yoshida, Z.; Takekuma, H.; Takekuma, S.; Matsubara, Y. *Angew. Chem., Int. Ed.* **1994**, *33*, 1597–1599. (d) Anderson, T.; Nilsson, K.; Sundahl, M.; Westman, G.; Wennerström, O. *J. Chem. Soc., Chem. Commun.* **1992**, 604–606.
- <sup>13</sup> Ikeda, A.; Iizuka, T.; Maekubo, N.; Aono, R.; Kikuchi, J.; Akiyama, M.; Konishi, T.; Ogawa, T.; Ishida-Kitagawa, N.; Tatebe, H.; Shiozaki, K. *ACS Med. Chem. Lett.* **2013**, *4*, 752–756.
- <sup>14</sup> Fan, J.; Yudasaka, M.; Kasuya, D.; Azami, T.; Yuge, R.; Imai, H.; Kubo, Y.; Iijima, S. *J. Phys. Chem. B* **2005**, *109*, 10756–10759.
- <sup>15</sup> Miyawaki, J.; Matsumura, S.; Yuge, R.; Murakami, T.; Sato, S.; Tomida, A.; Tsuruo, T.; Ichihashi, T.; Fujinami, T.; Irie, H.; Tsuchida, K.; Iijima, S.; Shiba, K.; Yudasaka, M. *ACS Nano* **2009**, *3*, 1399–1406.
- <sup>16</sup> Star, A.; Steuerman, D. W.; Heath, J. R.; Stoddart, J. F. *Angew. Chem. Int. Ed.* **2002**, *41*, 2508–2512.
- <sup>17</sup> Dai, H.; Yang, C.; Ma, X.; Lin, Y.; Chen, G. *Chem. Commun.* **2011**, *47*, 11915–11917.
- <sup>18</sup> Kitiyanan, B.; Alvarez, W. E.; Harwell, J. H.; Resasco, D. E. *Chem. Phys. Lett.* **2000**, *317*, 497–503.
- <sup>19</sup> Moore, V. C.; Strano, M. S.; Haroz, E. H.; Hauge, R. H.; Smalley, R. E. *Nano Lett.* **2003**, *3*, 1379–1382.
- <sup>20</sup> Harano, K.; Homma, T.; Niimi, Y.; Koshino, M.; Suenaga, K.; Leibler, L.; Nakamura, E. *Nat.*

### Chapter 3

*Mater.* **2012**, *11*, 877–881.

<sup>21</sup> (a) Khan, A. R.; Forgo, P.; Stine, K. J.; D'Souza, V. T. *Chem. Rev.* **1998**, *98*, 1977–1996. (b) Tang, W.; Ng, S.-C. *Nat. Protoc.* **2008**, *3*, 691–697. (c) Popr, M.; Hybelbauerová, S.; Jindřich, J. *Beilstein J. Org. Chem.* **2014**, *10*, 1390–1396.

<sup>22</sup> Materials Studio, version 5.0, Accelrys Software Inc., 2009.

<sup>23</sup> Kirkland, E. J. in *Advanced Computing in Electron Microscopy*, Plenum, London, 1998.

**— Chapter 3 —  
Experimental Section  
&  
Supporting Information**

## *Chapter 3*

### Table of Contents

#### 1. General

#### 2. Materials

#### 3. Measurements

#### 4. References

#### 1. General

All reactions dealing with air- or moisture-sensitive compounds were in a dry reaction vessel under nitrogen or argon atmosphere. The water content of the solvent was confirmed with a Karl-Fisher Moisture Titrator (MKC-210, Kyoto Electronics Company) to be less than 100 ppm. Analytical thin-layer chromatography was performed on a glass plate coated with 0.25 mm 230–400 mesh silica gel containing a fluorescent indicator (Merck). Analysis and isolation with high performance liquid chromatography (HPLC) was performed on SHIMADZU HPLC system equipped with an octadecyl-silica gel column (Phenomenex® Kinetex 5 mm C18 100 Å, LC Column 150 x 4.6 mm for analysis, Kinetex 5 mm C18 100 Å, AXIA Packed LC Column 150 x 21.2 mm for isolation; column temperature at rt). Flash silica gel chromatography was performed on silica gel 60N (Kanto, spherical and neutral, 140–325 mesh) as described by Still.<sup>1</sup> Reverse phase column chromatography was performed on octadecyl-silica gel Wakogel® C18 Series (Wako, spherical and neutral, 38–63 or 63–212 mesh). Ion-exchange column chromatography was performed on DOWEX® 50WX8–100 cation-exchange resin (Sigma Aldrich) and DOWEX™ 1x4 20–25 mesh anion-exchange resin (Wako). Infrared (IR) were recorded on an ASI Applied System React IR1000 equipped with an attenuated total reflection (ATR) instrument or JASCO/ FT IR-420 and are reported as wavenumbers ( $\nu$ ) in  $\text{cm}^{-1}$ . NMR spectra were measured on JEOL ECX-400 and ECA-500 spectrometers and reported in parts per million from tetramethylsilane (TMS). <sup>1</sup>H NMR spectra in D<sub>2</sub>O and DMSO were referenced internally to acetone as standard, <sup>13</sup>C NMR spectra to the solvent resonance. Thermogravimetric (TG) measurement was carried out on a Rigaku Thermo Plus machine from 30 °C to 1000 °C at the rate of 10 °C/min in dry air atmosphere with a flow rate of 100 mL/min using an alumina pan. Dynamic light scattering (DLS) study was carried out on a Malvern Zetasizer Nano ZS machine. Transmission electron microscopy (TEM) was performed on a JEOL JEM-2100F (acceleration voltage: 120 kV). High resolution TEM was performed on a JEOL ARM-200F (acceleration voltage: 120 kV).

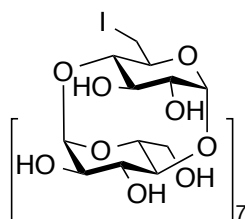
## Chapter 3

### 2. Materials

Unless otherwise noted, materials were purchased from Tokyo Kasei Co., Aldrich Inc., and other commercial suppliers and used after appropriate purification before use. Anhydrous ethereal solvents (stabilizer-free) were purchased from WAKO Pure Chemical and purified by a solvent purification system (GlassContour)<sup>2</sup> equipped with columns of activated alumina and supported copper catalyst (Q-5) prior to use. All other solvents were purified by distillation and stored over molecular sieves 4 Å. Distilled water was further purified with Millipore Milli-Q.

### Synthesis

#### Mono(6-deoxy-6-iodo)- $\gamma$ -cyclodextrin (I- $\gamma$ -CD 2)



Mono(6-*O-p*-tolenesulfonyl)- $\gamma$ -cyclodextrin<sup>3</sup> and KI were dried under vacuum pressure for 18 h. To a solution of mono(6-*O-p*-tolenesulfonyl)- $\gamma$ -cyclodextrin (40 mg, 27  $\mu$ mol) in dry DMF (2 mL), KI (90 mg, 0.54 mmol) was added and the reaction mixture was stirred at 100 °C for 48 h. Progress of the reaction was traced by TLC using <sup>n</sup>PrOH/EtOAc/H<sub>2</sub>O = 7/7/5 as eluent. The reaction mixture was cooled to rt, and then it was pored into acetone (100 mL) to precipitate the product. The precipitates were collected by filtration with PTFE membrane filter, washed with acetone (20 mL x 3 times), and dried under vacuum pressure. Further purification was conducted by inverse phase column chromatography on ODS silica gel (Wakogel®50C18) using H<sub>2</sub>O/MeOH as eluent. The desired product was obtained as a white solid (26 mg, 19  $\mu$ mol, 70%): mp 212-214 °C (dec); IR (powder) 3307, 2924, 2359, 1646, 1418, 1337, 1154, 1080, 1023, 938, 850, 758, 704, 641 cm<sup>-1</sup>; <sup>1</sup>H NMR (400 MHz, D<sub>2</sub>O)  $\delta$  3.30–3.34 (m, 2H), 3.39–3.51 (m, 16H), 3.70–3.78 (m, 30H), 4.93 (d, 7H, *J* = 3.6 Hz), 5.04 (d, 1H, *J* = 3.7 Hz); <sup>13</sup>C NMR (100 MHz, D<sub>2</sub>O, i.s. acetone:  $\delta$  (CH<sub>3</sub>) = 30.89)  $\delta$  7.58, 60.81, 60.95, 61.17, 70.80, 72.36, 72.59, 72.92, 73.42, 73.54, 81.03, 81.13, 81.34, 85.03, 102.10, 102.29 ; HRMS (ESI<sup>+</sup>): Calculated for [C<sub>48</sub>H<sub>79</sub>O<sub>39</sub>INa]<sup>+</sup>: 1429.3135, found: 1429.3193.

### **3. Measurements**

#### **Evaluation of dispersity of CNH via complexation with saccharides**

CNH (5 mg) was stirred in a solution of saccharides (glucose,  $\alpha$ ,  $\beta$ ,  $\gamma$ -CD, starch, 1 wt% for CNH) in water (10 mL) at 70 °C (heated in a sand bath) for 42 h. The mixtures were cooled down to rt, and then they were sonicated (38 kHz, 360 W) for 5 min at exactly the same spot in the bath sonicator with hold-shaking. The dispersed liquid was left to stand for 48 h for the ill-dispersed CNH to precipitate. The top layer (5 mL) was collected and excess saccharides were washed out with water (10 mL). The collected CNH was dried under vacuum condition with P<sub>2</sub>O<sub>5</sub> as a drying reagent overnight.

#### **TG analysis**

Before TG analysis, samples were dried up under vacuum condition with P<sub>2</sub>O<sub>5</sub> as a drying reagent. Weight loss of the samples was measured by Rigaku Thermo Plus machine from 30 °C to 1000 °C at the rate of 10 °C/min in dry air atmosphere with a flow rate of 100 mL/min using an alumina pan. Temperature derivatives of the weights curve were plotted from the weight loss curve.

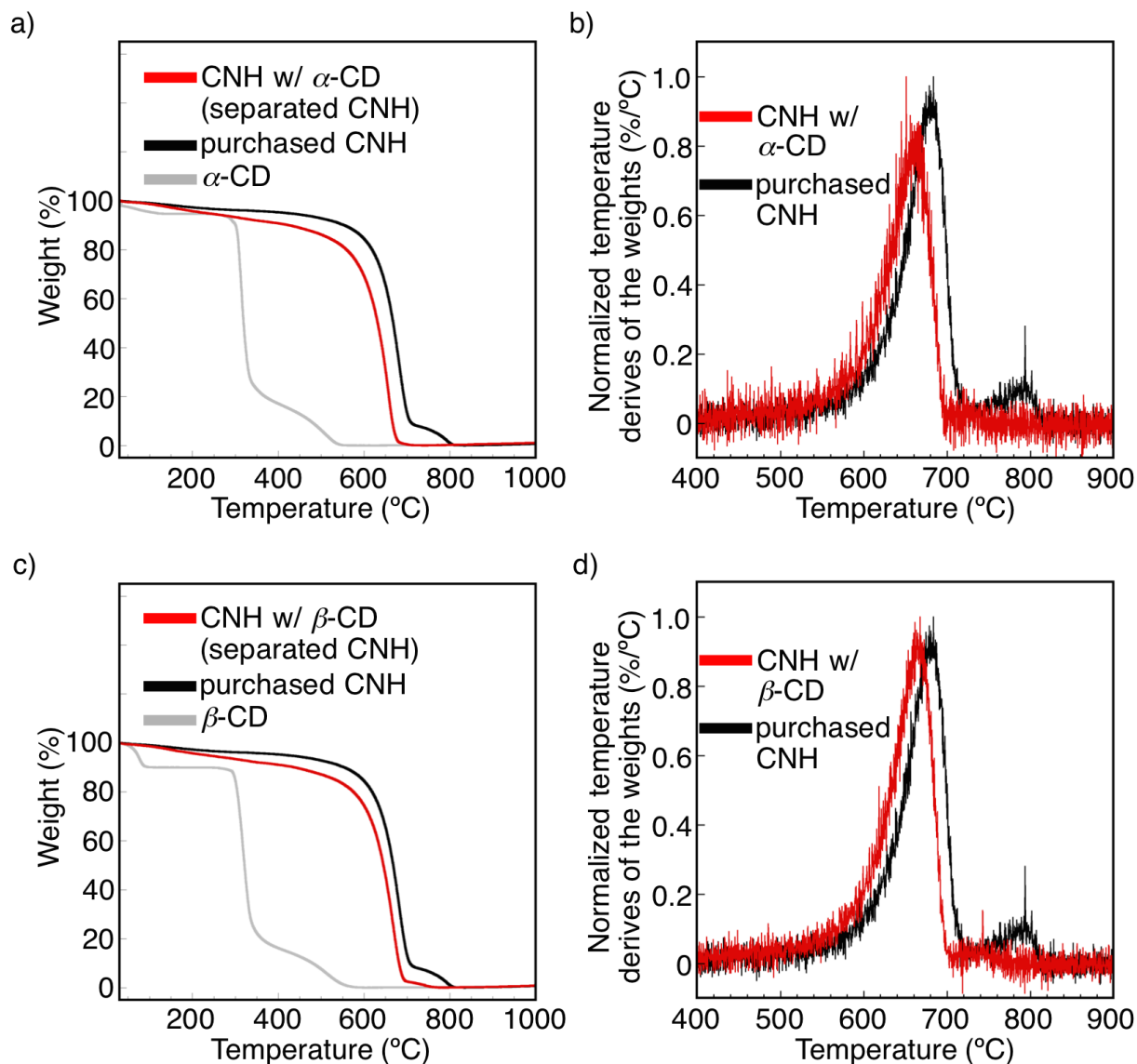
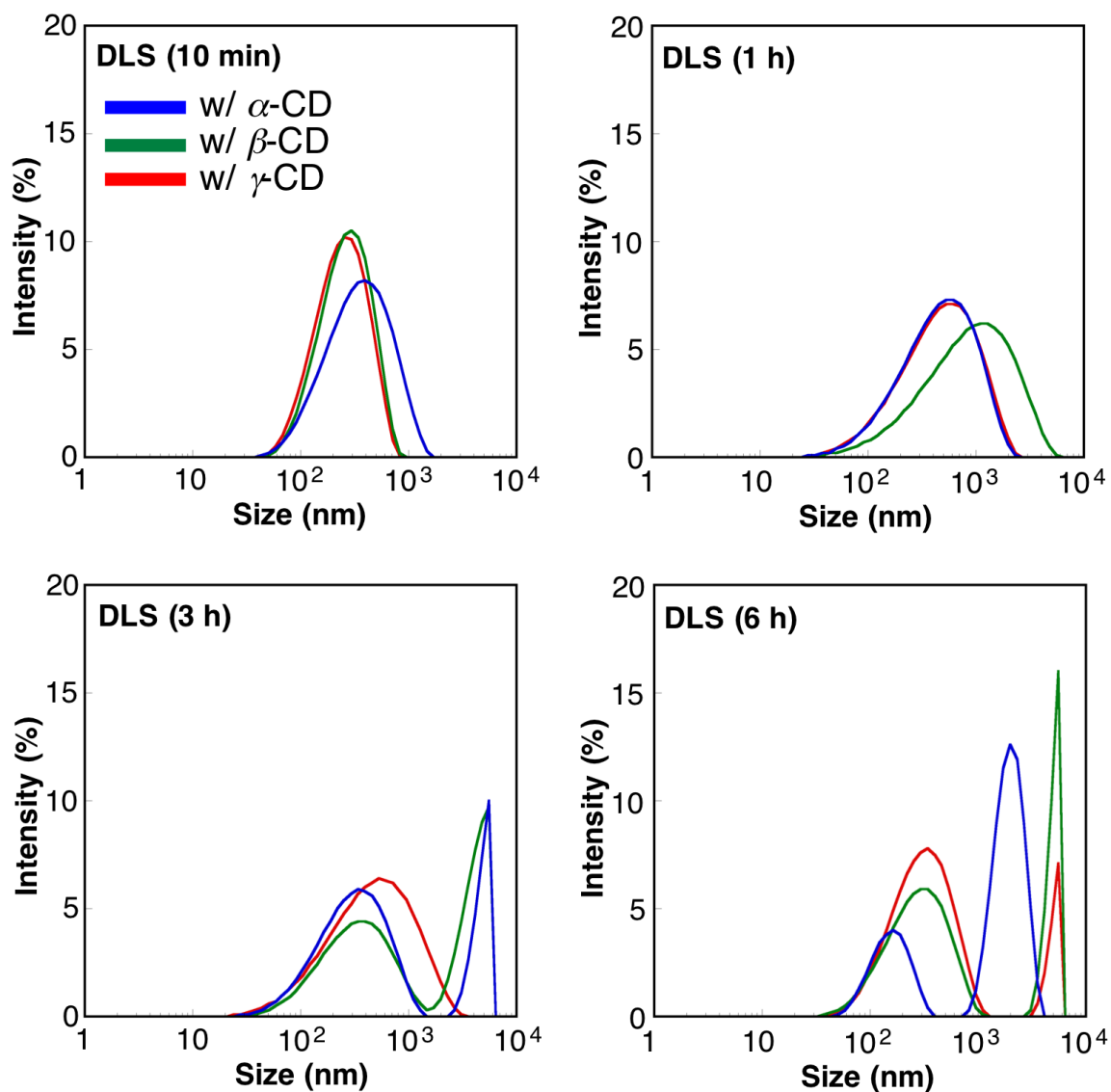


**Figure S3-1.** Thermogravimetric measurement of CNH aggregates. (a), (c) Weight-temperature curve of CNH aggregates separated with CDs (1 wt%) in water (red,  $\alpha$ -CD/CNH complex in a and b,  $\beta$ -CD/CNH complex in c and d), and purchased CNH (without separation treatment), respectively. CNH aggregates heated at 70 °C in water (black) and CDs (gray). (b), (d) Temperature derivatives of the weights curve of  $\alpha$ -CD/CNH complex,  $\beta$ -CD/CNH complex, and overlap of the curve of CD/CNH complexes. TG analysis was carried out from 30 °C to 1000 °C at a rate of 10 °C/min under dry air flow at 100 mL/min. Samples were taken from top layer of the dispersion liquid 48 h after standing.

### DLS measurement

DLS measurement was performed by using Malvern Zetasizer Nano ZS equipped with an He-Ne laser operating 4 mW power and 633 nm wavelength, and a computer-controlled correlator, at a 173° accumulation angle. Measurements were carried out in polystyrene cuvette. The data were processed using Dispersion Technology Software version 7.11 to give Z-average particle size and polydispersity index (PDI) value by cumulant analysis, and particle size distribution by CONTIN analysis<sup>4</sup>.





dispersant (time)	average diameter (nm)	Pdl
$\alpha$ -CD (10 min)	295	0.391
(1 h)	334	0.425
(3 h)	441	0.945
(6 h)	491	0.841
$\beta$ -CD (10 min)	224	0.241
(1 h)	578	0.474
(3 h)	557	1.00
(6 h)	762	0.818
$\gamma$ -CD (10 min)	206	0.261
(1 h)	333	0.452
(3 h)	328	0.575
(6 h)	381	0.724

**Figure S3-2.** DLS data for re-dispersed CNH complexes with  $\alpha$ -CD (blue),  $\beta$ -CD (green), or  $\gamma$ -CD (red) (1 mg) in water (1 mL) at 25 °C.

## Chapter 3

### TEM measurement

TEM measurement was performed by JEOL JEM-2100F at an electron acceleration voltage of 120 kV. The black powder of CD/CNH complexes and  $\gamma$ -CD derivatives-immobilized CNH aggregates (ca. 0.1 mg) were dispersed in water or toluene (1 mL) using bath sonicator for 10 seconds. 10  $\mu$ L of the dispersion liquid of samples was placed on a TEM microgrid and excessive amount of solvent was blotted by filter paper. The TEM microgrid was dried under vacuum condition for 2–3 hours before observation by TEM.

### Atomic-resolution TEM measurement

Atomic-resolution TEM measurements were carried on a Cs-corrected JEOL JEM-ARM200F equipped with a thermal field-emission gun, CEOS CECTOR aberration-corrector, GATAN Ultrascan CCD camera, and a double-tilt sample holder (acceleration voltage of 120 kV, 3.7 pA/cm<sup>2</sup>, T = 293 K, 1.0 x 10<sup>-5</sup> Pa, spherical aberration C3 = -15  $\pm$  6  $\mu$ m, C5 = 12  $\pm$  7 mm). Sequential images were obtained at 1024 x 1024 pixels resolution in 2.0 x 10<sup>6</sup> magnification with the exposure time of 0.4 seconds followed by data readout of 0.79 seconds.

### Correction of TEM images

TEM images taken by JEOL JEM-2100F were observed at underfocus. TEM images taken by JEOL JEM-ARM200F were observed at overfocus, but the contrast was inverted by image software, Image J. Noises and blur in the images were filtered by bandpass filter to improve the signal to noise ratio, and then the contrast and the brightness were adjusted.

### SMART-TEM image simulation: Determination of the molecular structure of $\gamma$ -CD and I- $\gamma$ -CD 2

Computational molecular models of the  $\gamma$ -CD/CNH complex and I- $\gamma$ -CD 2/CNH complex were constructed with a variety of conformations of the molecules, and viewed from a variety of directions. Modeling of the molecular structure was optimized by molecular mechanics calculations using Compass force field implemented in Materials Studio.<sup>5</sup> TEM simulation images were generated from the modeling images for each structure by using a procedure implemented in a standard simulation software.<sup>6</sup> Each of the simulated TEM image was carefully compared with each image in the movie of the  $\gamma$ -CD/CNH complex to determine the location and the orientation of  $\gamma$ -CD molecules.

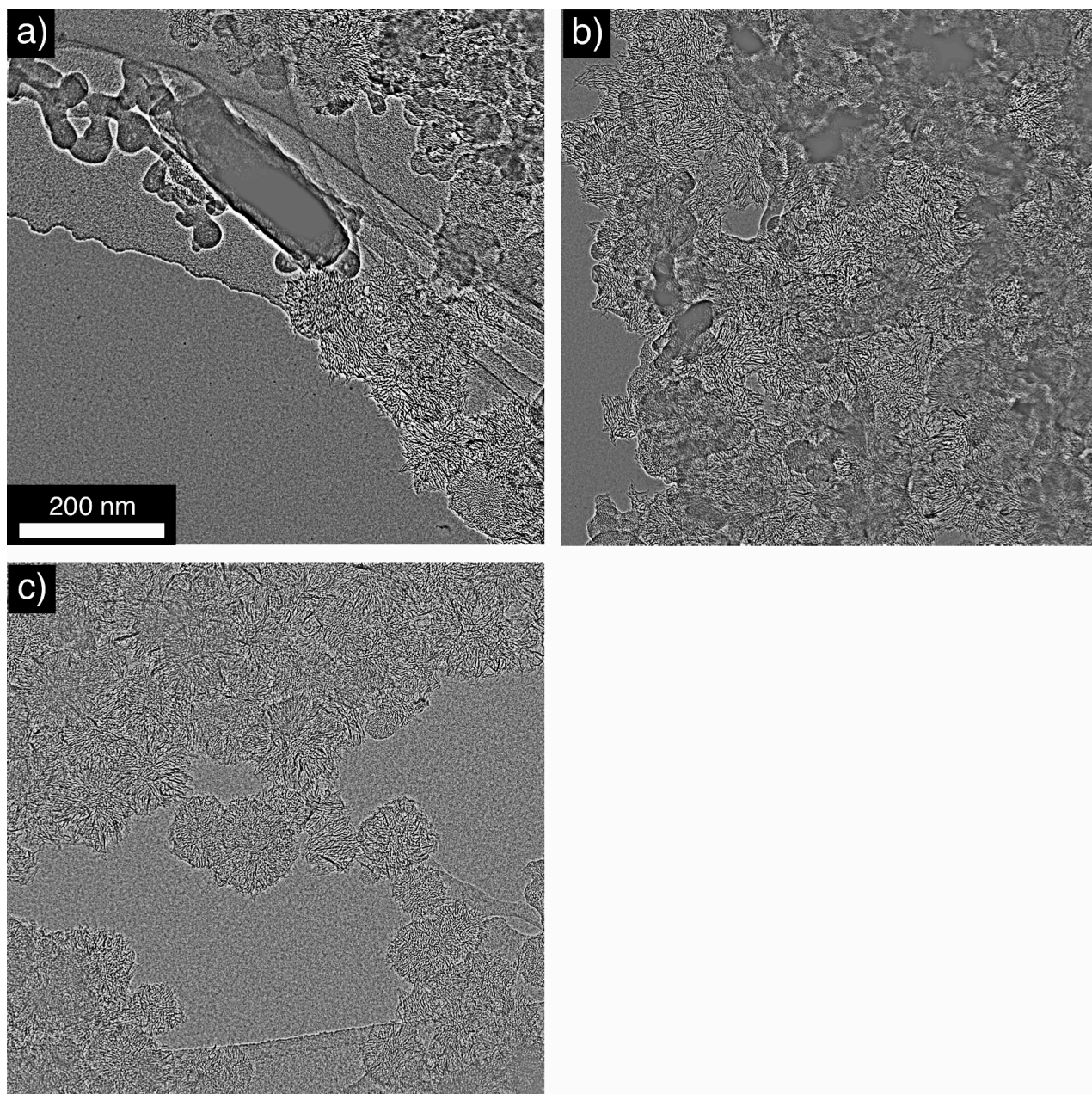


**Figure S3-3.** TEM images of CNH aggregates. (a), (b) CNH particles purchased from NEC, (c)  $\gamma$ -CD/CNH complex. Images were taken on JEOL JEM-2100F at an electron acceleration voltage of 120 kV.  $\mu$ mGCPs are found in image a. Large amount of nmGCPs adsorb on CNH aggregates are observed in image b, but no such particles exist in image c.

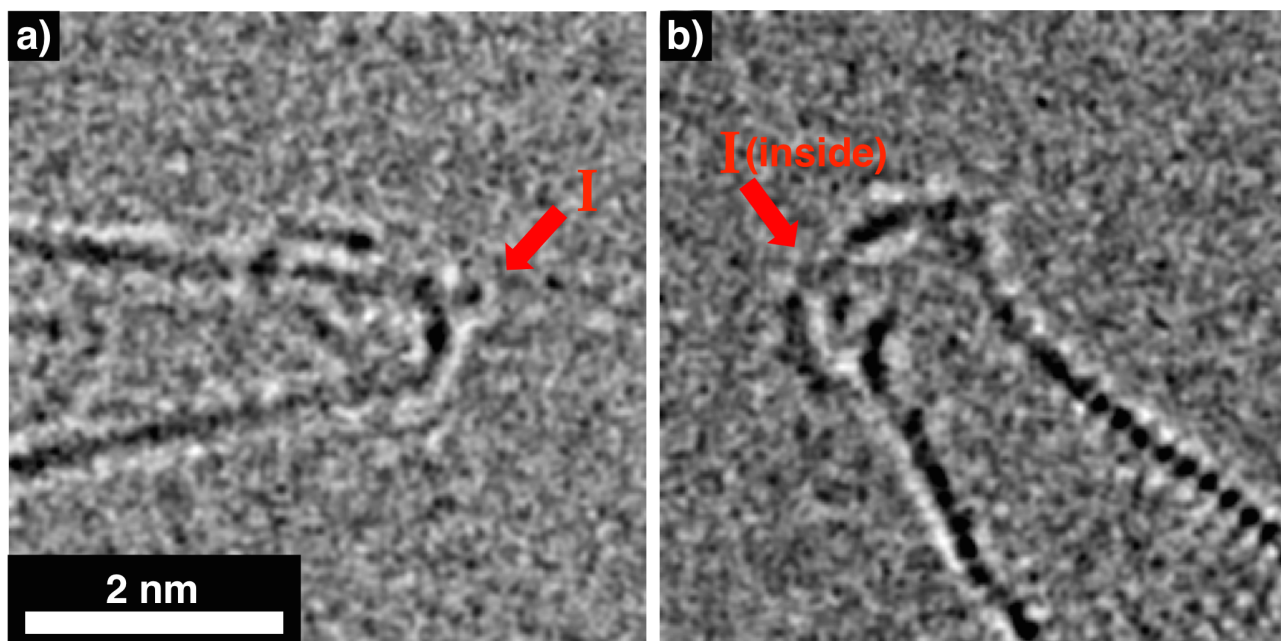


**Figure S3-4.** TEM images of I- $\gamma$ -CD 2/CNH complex. Conducted by JEM-ARM200F at an electron acceleration voltage of 120 kV, under low electron dose (3.7 pA/cm<sup>2</sup>).

#### Curvature analysis of CD-bound tip

Relationship between morphology of the tip of CNH and complexation of CDs were evaluated by measuring a radius of curvature of the tip of CD-bound CNH. The radius of curvature of the tip ( $r$ ) was calculated by the following equation derivatized from Pythagorean theorem using fitting lines described in Figure S3-5b.

$$r = \frac{\{(PB + PC)/2\}^2 - PA^2}{2PA}$$

Tangent points and intersections are put on the center of the contrast of atoms. Two lines tangent to the curvature of the tip (PB and PC) are averaged. Point A is an intersection of a bisector of  $\angle BPC$  and CNH. Radius of curvature of the tip ( $r$ ) was calculated from fifteen CD-bound CNHs in TEM images. Error of the value is calculated as standard error.

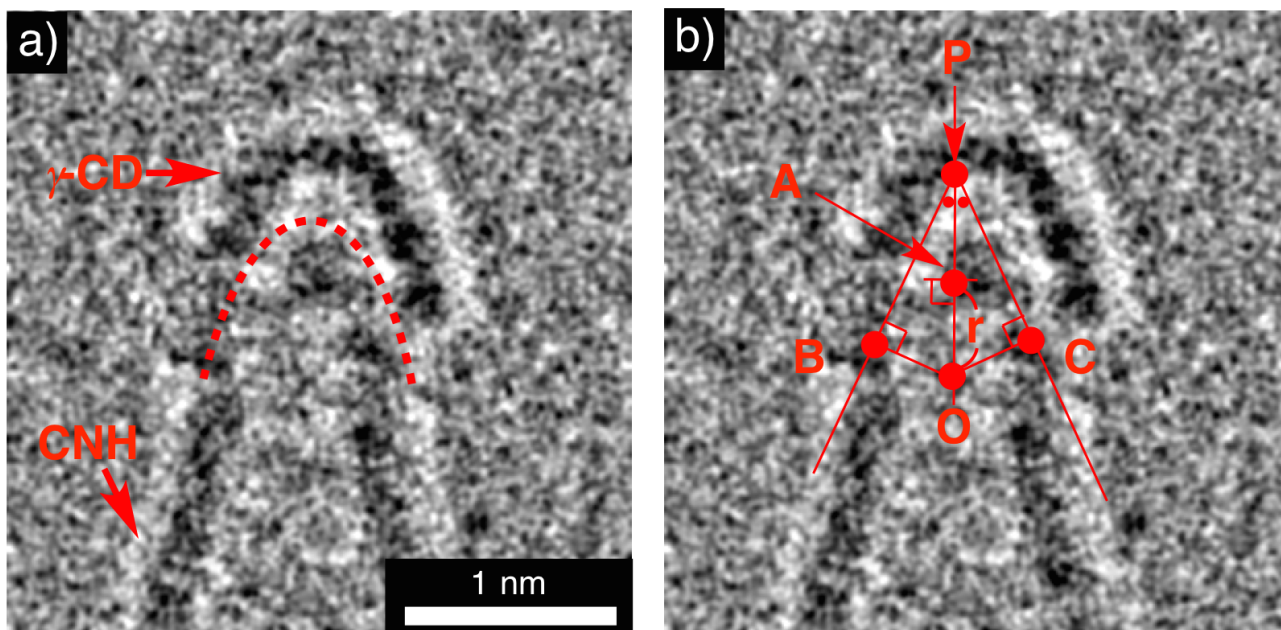


**Figure S3-5.** TEM images of  $\gamma$ -CD-bound CNH (a). Surface curvature of CNH is indicated with red dash line and  $\gamma$ -CD is denoted by red arrow in image a. (b) The same image as in image b, fitting lines for CNH and intersections are indicated with red line and dot. TEM measurement was carried on JEOL JEM-ARM200F at an electron acceleration voltage of 120 kV.

### Modeling method of a host-guest complex of $\gamma$ -CD and I- $\gamma$ -CD 2 on the tip of CNH

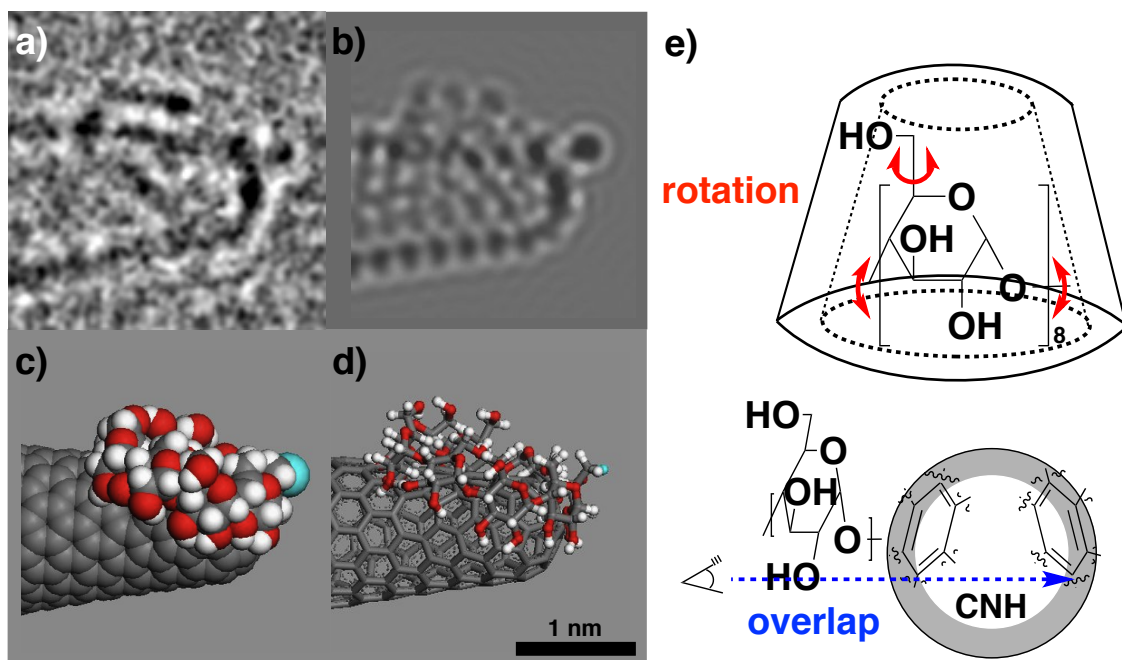


**Figure S3-6.** Simulation and modeling of I- $\gamma$ -CD/CNH complex. (a) TEM image, (b) Simulation image of (a) (120 kV, defocus: 110 Å), (c, d) Corresponding modeling images of (b), gray: carbon, white: hydrogen, red: oxygen, pale blue: iodine, (e) Illustration of structure optimization in the simulation and modeling of I- $\gamma$ -CD 2.

Chapter 3

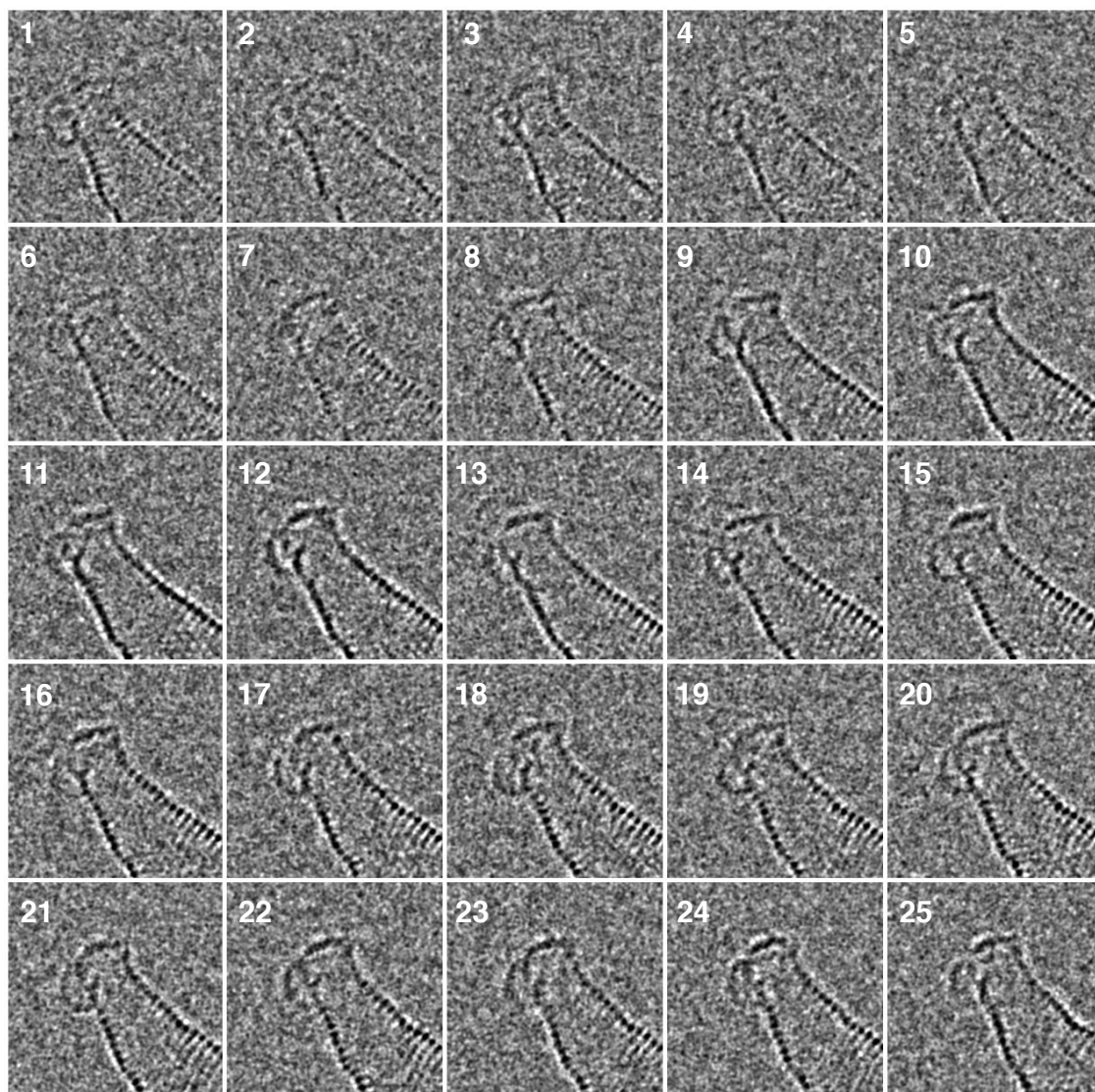


**Figure S3-7.** A series of TEM images of I- $\gamma$ -CD 2/CNH complex (image b in Figure S3-4). Image size: 5.0 x 5.0 nm.

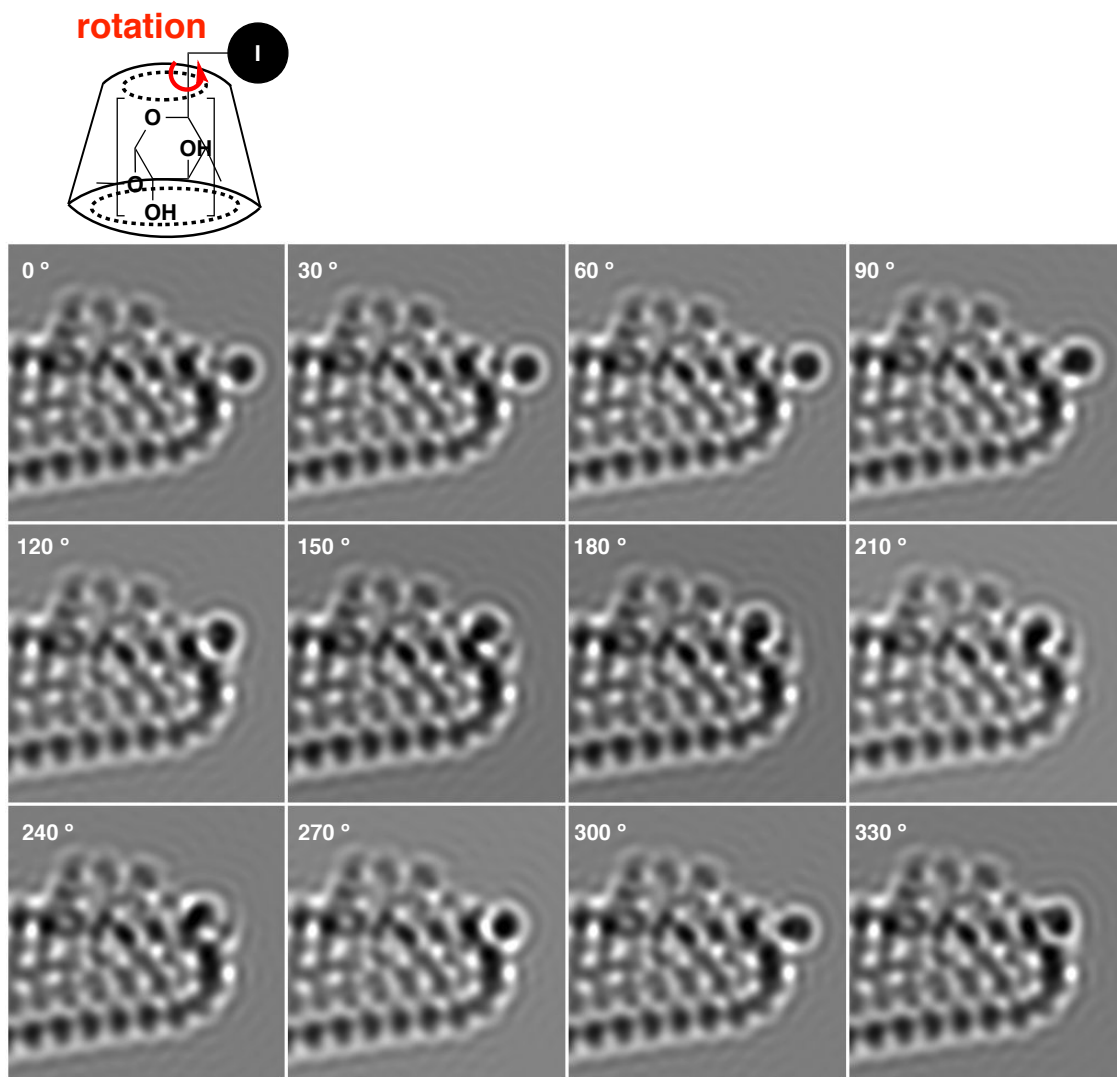


**Figure S3-8.** Simulation images of I- $\gamma$ -CD 2 in Figure 3-13 with rotation of the C5–C6 single bond.

### Chapter 3

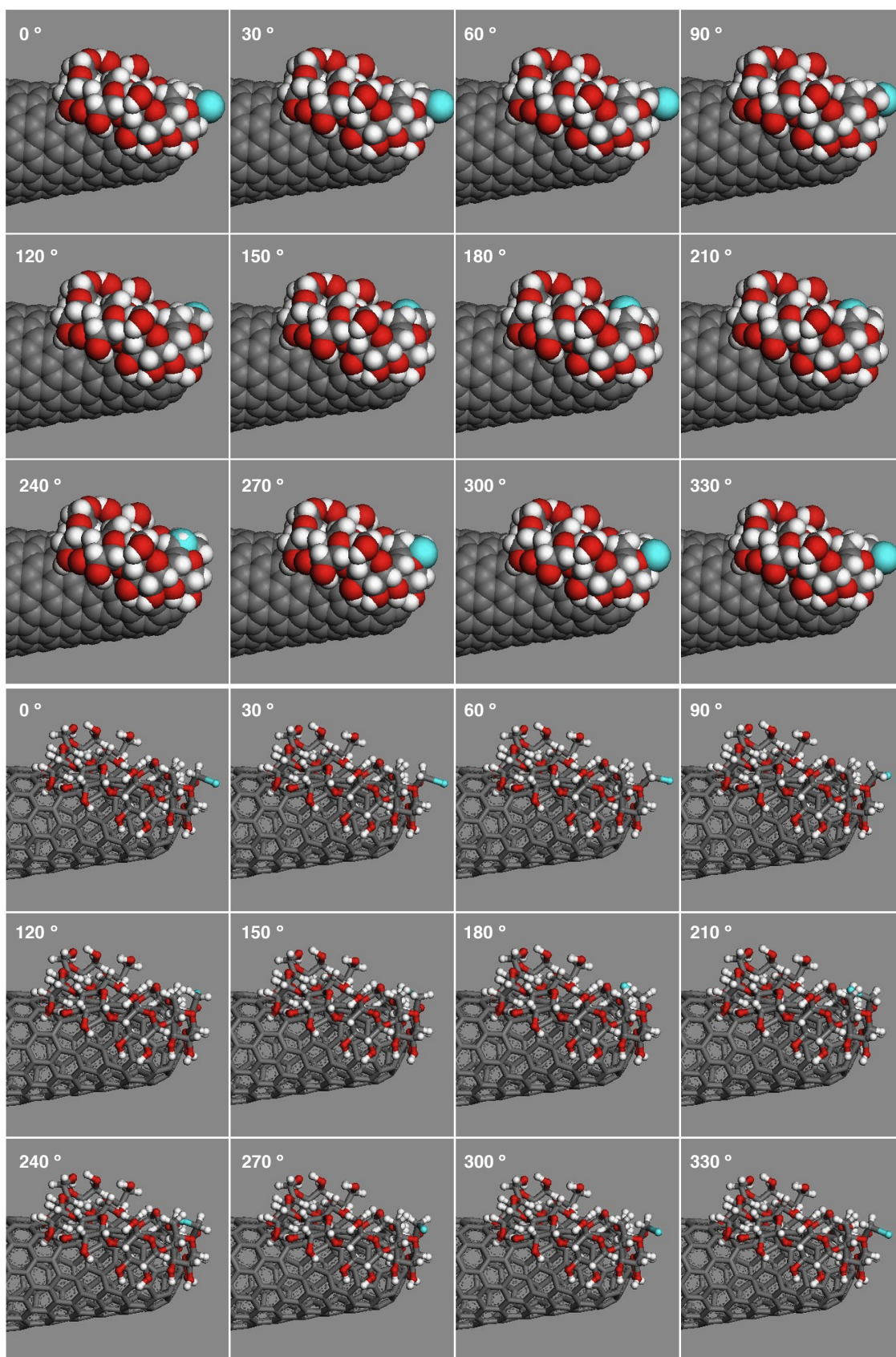


**Figure S3-9.** Modeling images of I- $\gamma$ -CD **2** in Figure 3-13 with rotation of the C5-C6 single bond. Gray: carbon, white: hydrogen, red: oxygen, pale blue: iodine.



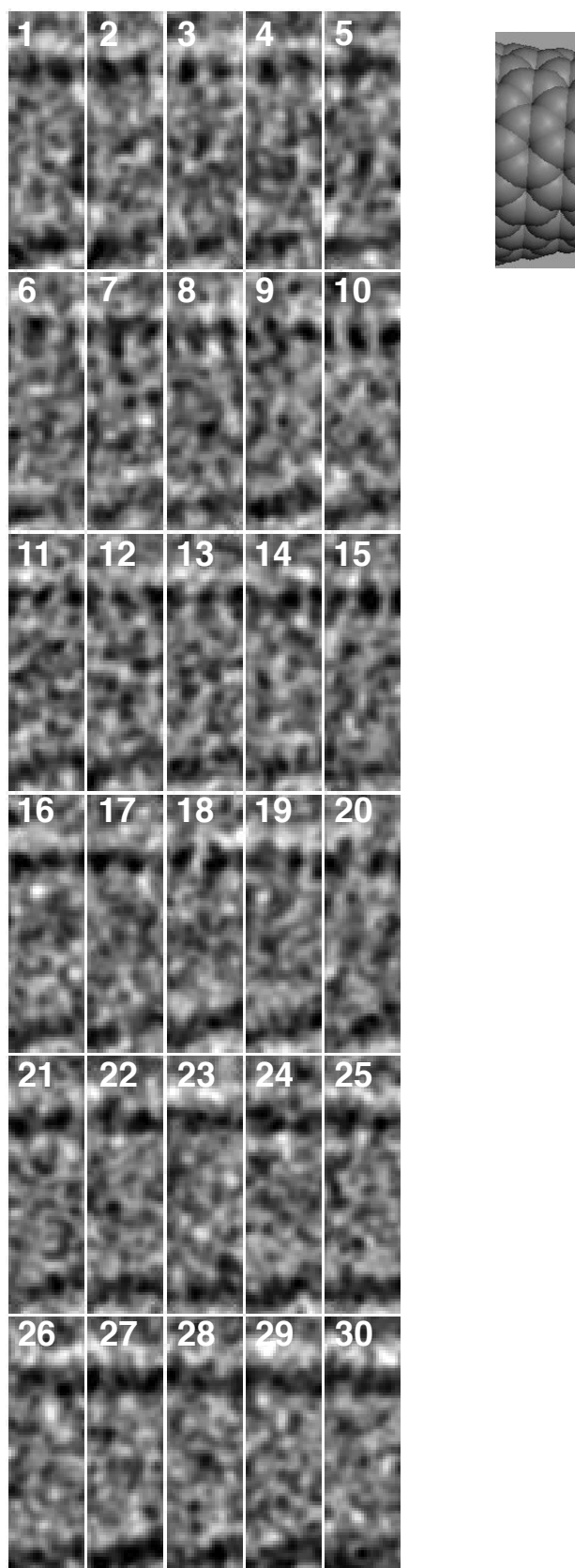


**Figure S3-10.** A series of TEM images of CNH region, area 1 in Figure 3-15b. Image size: 0.5 x 1.7 nm.

Chapter 3

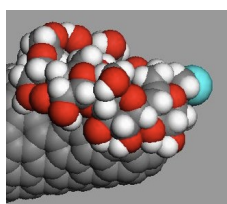
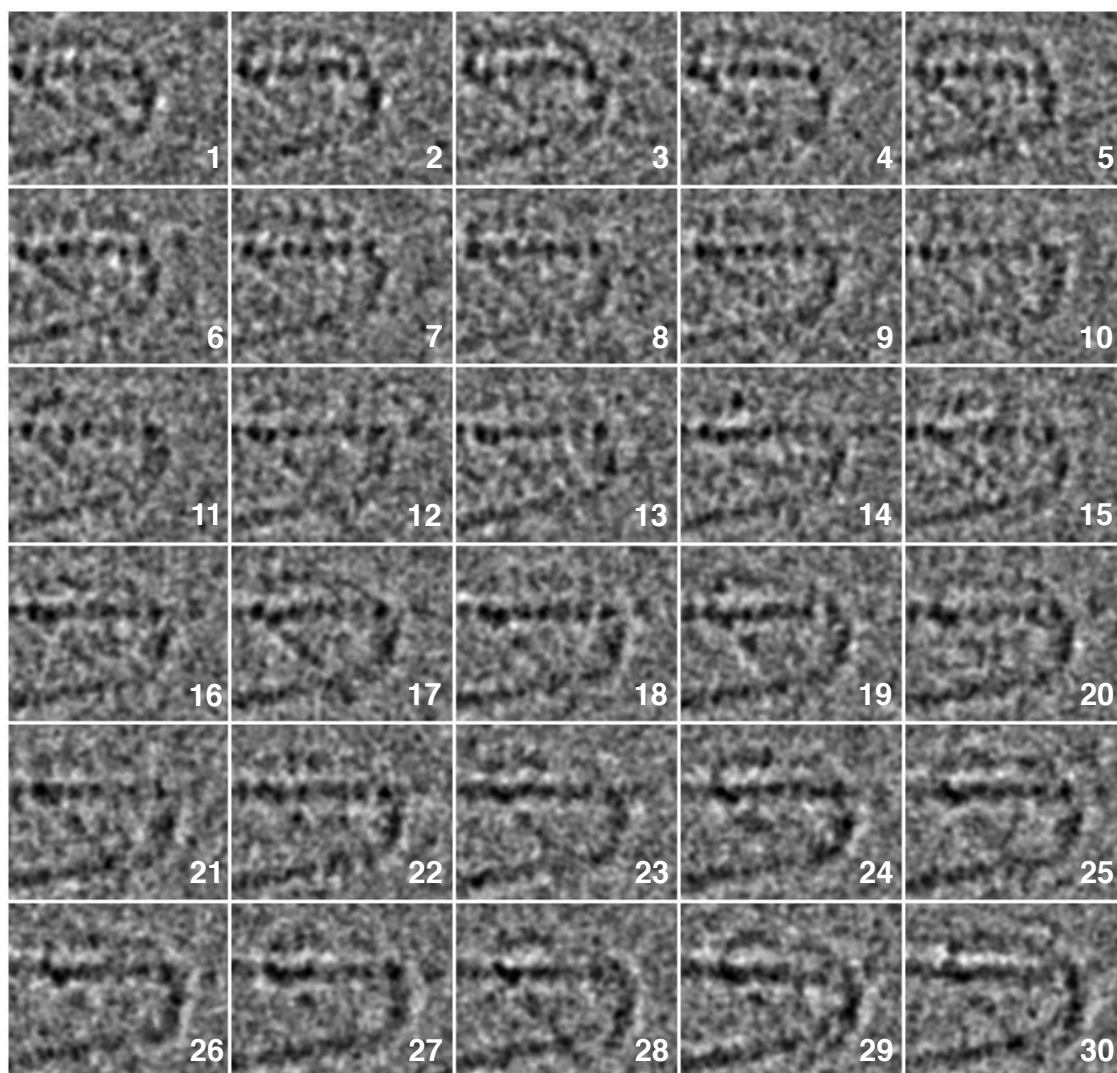


**Figure S3-11.** A series of TEM images of CNH region, area 2 in Figure 3-15b. Image size: 2.4 x 1.9 nm.

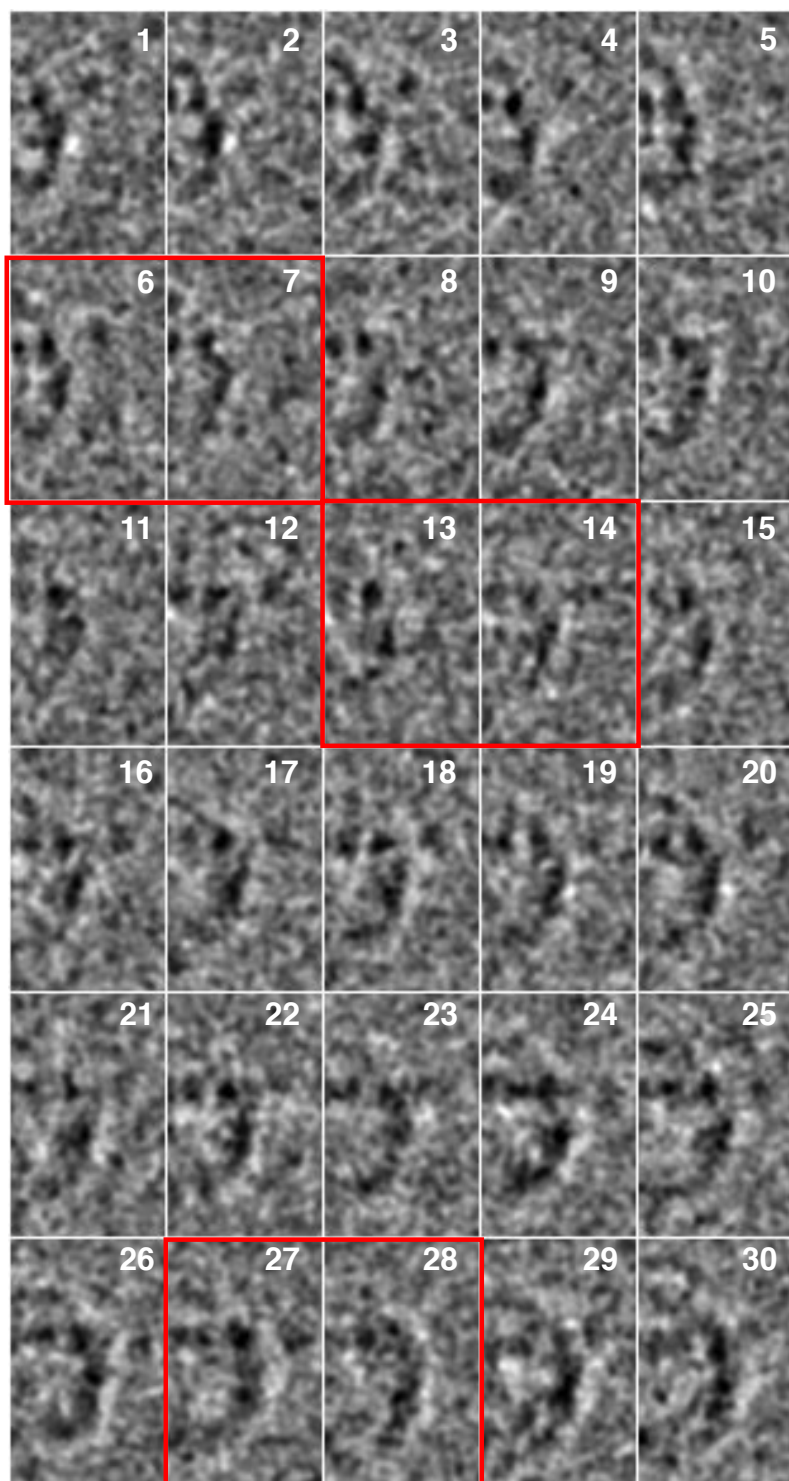
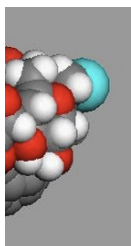


**Figure S3-12.** A series of TEM images of CNH region, area 3 in Figure 3-15b. Image size: 1.3 x 1.9 nm. Red rectangles denote consecutive two TEM images of cross-correlation factor indicated with stars in Figure 3-15a.

#### 4. References

- <sup>1</sup> Still, W. C.; Kahn, M.; Mitra, A. *J. Org. Chem.* **1978**, *43*, 2923–2925.
- <sup>2</sup> Pangborn, A. B.; Giardello, M. A.; Grubbs, R. H.; Rosen, R. K.; Timmers, F. J. *Organometallics*, **1996**, *15*, 1518–1520.
- <sup>3</sup> Tang, W.; Ng, S.-C. *Nat. Protoc.* **2008**, *3*, 691–697.
- <sup>4</sup> Provencher, S. W.; Stepánek, P. *Particle & Particle Systems Characterization*, **1996**, *13*, 291–294.
- <sup>5</sup> Materials Studio, version 5.0, Accelrys Software Inc., 2009.
- <sup>6</sup> Kirkland, E. J. in *Advanced Computing in Electron Microscopy*, Plenum, London, 1998.

**— Chapter 4 —  
Summary & Outlook**

## *Chapter 4*

## Chapter 4

In the present thesis, I developed two kinds of precisely controlled supramolecular surface modification methods in molecular-level to overcome long-standing problems on noncovalent modification of self-assembled objects and nanocarbons resulting from nonspecific binding of functional molecules on their surface. One is post-surface modification of a self-assembled capsule via fluororous interaction that does not affect to the structural integrity of the capsule. Another is shape-dependent surface modification of a nanocarbon via host-guest interaction that enable us to functionalize it with high efficacy to the control of the physicochemical properties.

In chapter 2, protein-ligand display on the surface of sub-micrometer-sized fluororous fullerene vesicle via fluororous interaction was achieved without decreasing the mechanical stability of the membrane of the vesicle even after binding with proteins. Vesicle made of fluororous fullerene amphiphile are composed of a bilayer of amphiphilic fullerene where the fullerene core is located in the interior, perfluoroalkyl substituents are exposed to an aqueous environment, and the anionic part is located in the middle. Because of the unique fluororous/polar/fullerene (nonpolar) ternary architecture that enables hierarchical construction of vesicles by orthogonal interactions, fluororous-tagged saccharides as ligands for proteins were successfully immobilized on the fluororous surface of the vesicle via fluororous interaction just mixing the sample solutions (Figure 4-1).

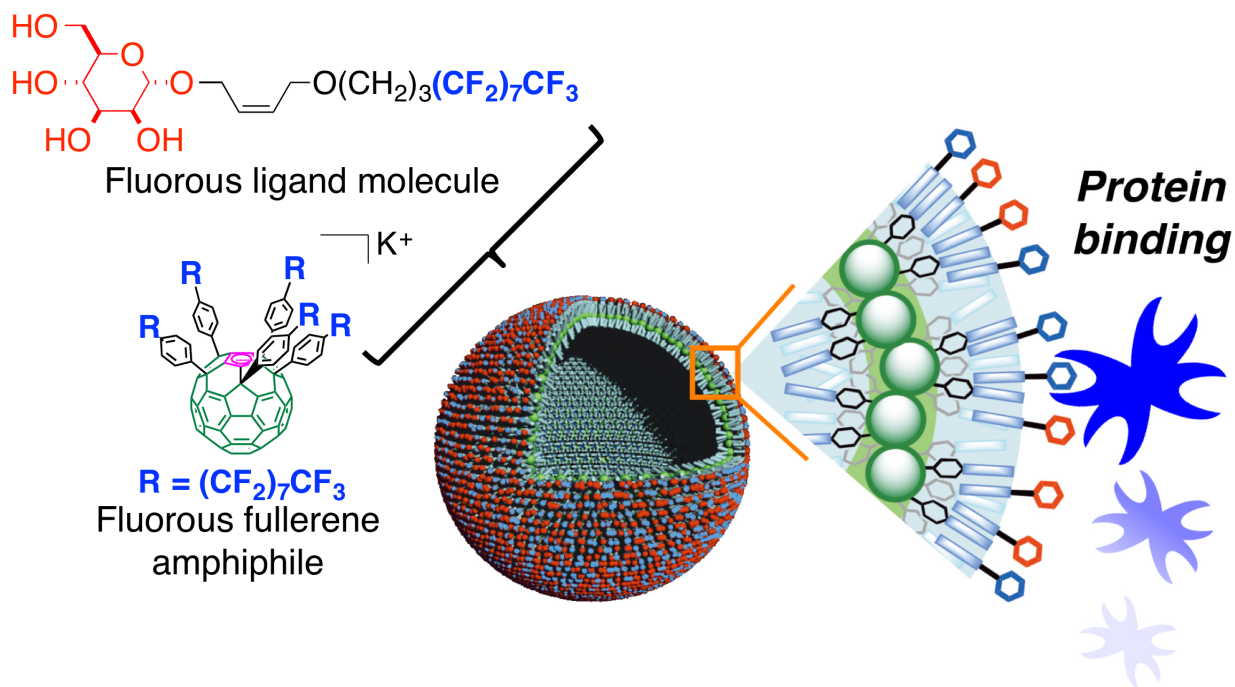


**Figure 4-1.** Ligand display on a self-assembled nanocapsule via fluororous interaction.

Because of the robust fullerene membrane and immiscibility of heavy fluororous molecules with non-fluororous molecules, only the fluororous tag moiety was incorporated into the fluororous surface

without penetration to the fullerene membrane, and the hydrophilic saccharide moiety and the aliphatic tether moiety were successfully displayed on the surface of the vesicles that enables them to be bound to the target proteins strongly.

Fluorous interaction was crucial for the ligand display and the following protein binding on the surface of the vesicle via ligand-protein interaction. This precision immobilization and the display of ligand molecules preserved the mechanical stability of the fullerene membrane that retains the vesicular structure even after binding with proteins on the surface of the vesicle confirmed by high resolution scanning-electron microscopy (SEM) measurements that can reveals the surface morphology of self-assembled objects (Figure 4-2). The protein ligand-decorated fluorine-rich and fullerene-based functional vesicles are expected to be applicable in medicinal applications.

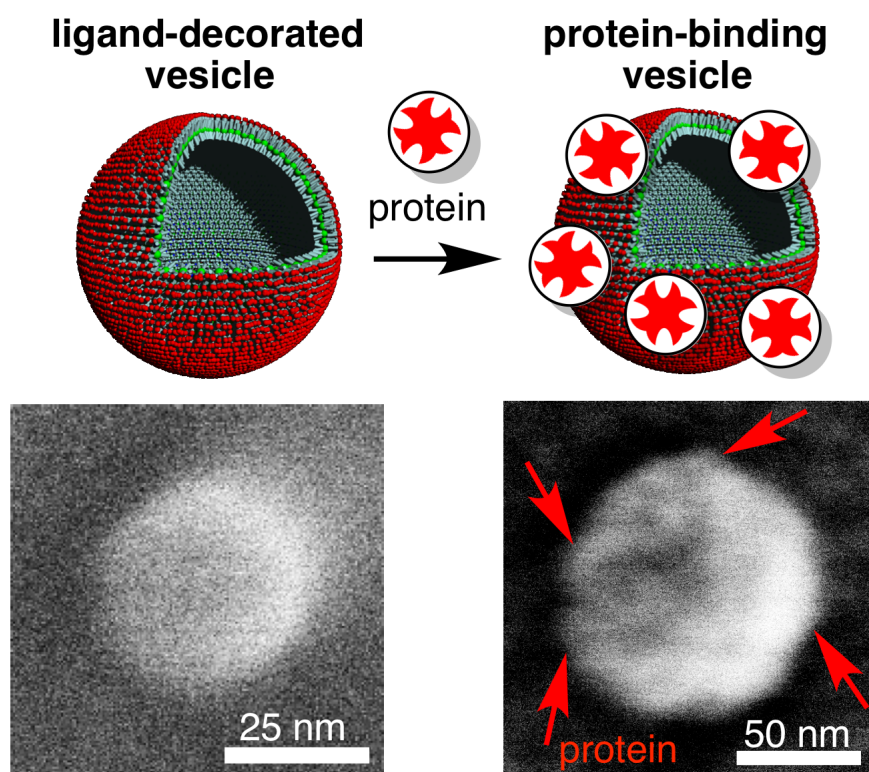


**Figure 4-2.** High resolution SEM measurement of ligand-decorated vesicle (left) and protein-binding vesicle (right). SEM measurement was performed on a smooth IZO/glass substrate at low landing voltage 200 V.

In chapter 3, shape-selective surface modification of specific cone-shapes of carbon nanohorn (CNH) via host-guest interaction of cyclodextrin (CD) was achieved. CNH aggregates are 50–150 nm-sized aggregates of cone-shaped carbon nanotubes. The size of cone-shaped tip of CNH is almost the same size as fullerene. CDs are usually used as a host molecule for encapsulation of small guest molecules in water through host-guest interaction. In particular,  $\gamma$ -CD is known to encapsulate fullerenes into its inner cavity and forms a stable water-soluble complex. Herein, I achieved non-covalent modification of the tip for separation of CNH aggregates from a mixture



with other nanocarbon particles by the shape and size-selective inclusion of  $\gamma$ -CD.  $\gamma$ -CD selectively bound to a small spherical tip of CNH and selectively dispersed horn-rich CNH aggregates in water. Usually excess amount of surfactant is needed to disperse and separate CNH aggregates, but the separation method of CDs only needed 1 wt% of CDs because of the strong and proper binding to the tip of CNH that is effective for wettability of the aggregates. In addition, interestingly, the CD/CNH complexes were visualized by transmission electron microscopy (TEM) with atomic resolution, and this imaging revealed that the relationship between molecular-level binding structure of CDs on the surface of CNH and the dispersibility of CD/CNH complex in water (Figure 4-3). Since binding stability of CDs on large tips of CNH is expected to be less than that bound on suitable small tips,  $\alpha$ -CD and  $\beta$ -CD were more easily detached from the tips than  $\gamma$ -CD. This difference in binding selectivity difference in CDs is also corresponding to the stability of dispersion of CNH aggregates dispersed with CDs. In addition, I demonstrated a proof of principle study of introducing a specimen to CNH via non-covalent interaction using substituted  $\gamma$ -CD as a fishhook for single molecule atomic real time TEM technique.

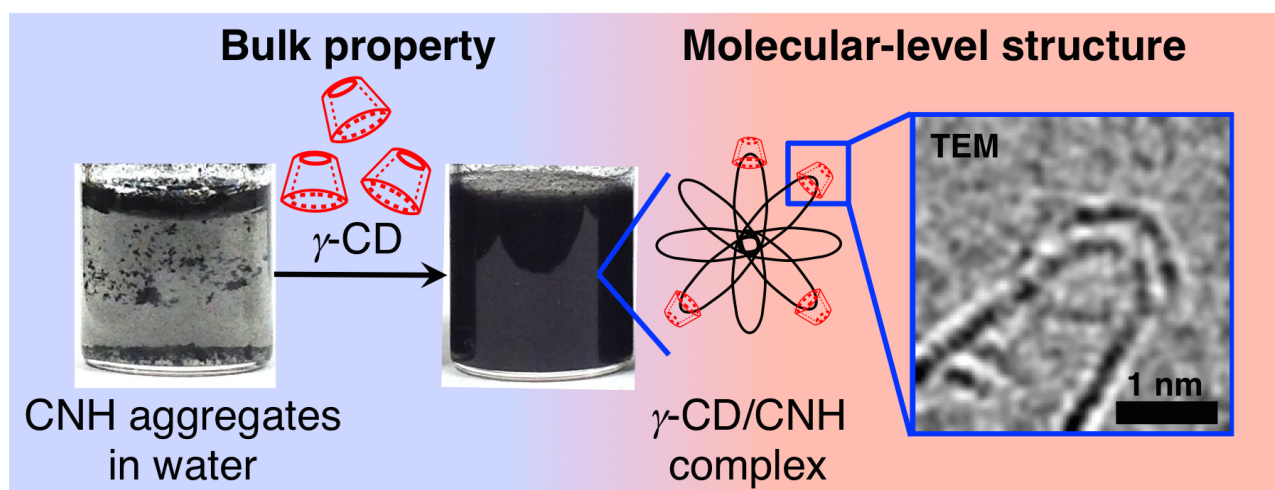


**Figure 4-3.** Host-guest complexation of  $\gamma$ -CD on the tip of CNH and the tip-selective modification induced dispersion of CNH aggregates in water.

This thesis gives knowledge and insight in molecular-level precision functionalization on the surface of a nanometer-sized self-assembled object and a nanocarbon, which enables us to control the bulk properties such as binding affinity to other materials and wettability with high efficacy. Proper molecular design enabled using fluororous interaction and host-guest interaction that have excellent selectivity in non-covalent surface modification of the nanometer-sized materials. In addition, high-resolution electron microscopic imaging revealed that not only surface morphology but also boundary between the molecular-level structure and the bulk properties of the materials.